Static and Fatigue Biaxial Flexural Behavior of Strain-Hardening UHPFRC Thin Slab Elements

Xiujiang SHEN

École
polytechnique
fédérale
de Lausanne

2020

"路漫漫其修远兮

　　　　吾将上下而求索"

-屈原

"Long, long had been my road and far, far was the journey

I would go up and down to seek my heart's desire"

- Yuan Qu

Foreword

Ultra-High Performance Fiber Reinforced Cementitious composite materials (UHPFRC) have high potential to strengthen effectively reinforced concrete structures and to develop into an own building method for new constructions, while reducing significantly the environmental impact compared to traditional reinforced concrete construction.

Cast as a relatively thin layer on existing reinforced concrete members to form a monolithic composite element, UHPFRC acts as an external reinforcement, increasing the ultimate and fatigue resistances. UHPFRC elements, complemented by steel reinforcement bars or prestressing, are relatively thin and allow for the construction of cost-effective lightweight structures. An additional benefit is that UHPFRC has extremely low permeability that provides outstanding durability.

In Switzerland, the UHPFRC technology is implemented on a larger scale for more than 10 years to enhance existing concrete structures and to build new structures, leading to more than 150 field applications by now. The UHPFRC technology transfer in Switzerland is based on the targeted research activity by the MCS group at EPFL. The present doctoral thesis by Xiujiang Shen is part of this 20 year-long research effort.

In his doctoral thesis, Xiujiang Shen investigated the failure process in thin slab elements of UHPFRC under quasi-static and fatigue loading. Such elements are increasingly been used worldwide for innovative new structures as well as for rehabilitation and strengthening of reinforced concrete members to increase their ultimate and fatigue resistances as well as the durability. Novel experimental methods have been developed to observe and characterize the tensile and fatigue behaviour of UHPFRC under uniaxial and equi-biaxial tensile stress state. The biaxial fatigue testing and the determination of fiber orientation effects by means of non-destructive testing are original and new. Consequently, novel knowledge regarding material characteristics of UHPFRC and their implementation in structural engineering are gained.

Xiujiang Shen provides the proof of his capabilities to conduct a scientific study and to solve complex scientific questions. In the name of the whole MCS Team, I thank him for his constant and thorough investment to the thesis topic as well as for his professional skills and personal qualities.

Lausanne, April 2020   Professor Eugen Brühwiler

Acknowledgement

I still owe a lot to my family, especially my parents Yilong and Baozhu, who support my any decisions whatever and whenever.

Finally, I would like to thank my wife, Yixuan, for all the discovery and sharing of happy moments, for her understanding during long-time-separation, especially during her prepregnant time. And thank her for giving birth of our lovely son.

Lausanne, April 2020

Xiujiang Shen

Summary

Cast-in-place thin layers of Ultra-High Performance Fiber Reinforced Cementitious Composites (UHPFRC) on the specific zones of existing reinforced concrete (RC) bridge decks has been demonstrated to be a technically efficient and economic rehabilitation and strengthening method. In these applications, the UHPFRC layer with typical thickness of 30 to 50mm, serving as tensile reinforcement, increases the bending and shear resistance of UHPFRC-RC composite members through its in-plane tensile resistance and deformability. Bridge deck slabs are the most fatigue loaded structural elements in bridges, and the actual stress state caused by wheel loading is nearly equi-biaxial and far from uniaxial. Bridge decks are expected to be subjected to a high number of fatigue stress cycles, which may exceed several hundred million. Accordingly, this thesis is devoted to study experimentally and analytically the static and fatigue flexural response of UHPFRC slab-like element subjected to biaxial stresses.

For a given UHPFRC mix, there are no intrinsic tensile properties. The representative behavior, especially the strain-hardening response, is dependent on the fiber distribution characterized by the fiber volume fraction V_f, fiber orientation μ_0 and fiber efficiency μ_1 within the UHPFRC element. The present thesis introduces firstly the uniformity factor μ_2 for considering the local fiber distribution within an UHPFRC element. Accompanied with the fiber orientation factor μ_0 and efficiency factor μ_1, the influence of μ_2 on the strain-hardening response of UHPFRC under uniaxial tension is investigated quantitatively by means of experimental campaign and mechanical analysis. The direct tensile test (DTT) was carried out on dumbbell specimens, extracted from a UHPFRC slab element, to characterize the tensile behavior of UHPFRC. Before tensile testing, actual fiber distribution of each specimen was measured by the non-destructive test (NDT) method using a magnetic probe. During DTT, the initiation and propagation of matrix discontinuities and the fictitious crack were monitored visually by the digital image correlation (DIC) system. Based on the present results and available literature, it is concluded that μ_2 is relevant to characterize the tensile strain-hardening response, especially the hardening strain ε_{Utu} and matrix discontinuities energy g_{Uf} of the tested UHPFRC. Additionally, ε_{Utu} and g_{Uf} are found to vary linearly with $\mu_0\mu_1\mu_2$ for a given UHPFRC mix. The average μ_2 value is proposed to be applied for scaling the representative tensile response in the design of UHPFRC structural elements. Finally, the most likely μ_2 values are determined for UHPFRC layers with different thickness.

In a next step, the biaxial flexural response of strain-hardening UHPFRC circular slab elements using ring-on-ring test method is investigated. The DIC system is applied to capture the 3D full-field strain and deflection of the tensile surface through the whole loading process. Based on the testing results, a quasi-elastic limit is introduced to characterize the flexural response of UHPFRC under biaxial stress condition. The random and uniform distribution of matrix discontinuities in the quasi-elastic domain, as well as multiple fictitious cracks in the hardening domain of structural specimen response, is highlighted. In addition, an in-depth comparison between ring-on-ring test

and 4-Point-Bending-Test (4PBT) results, with special emphasis on flexural strength and matrix discontinuity development, is conducted. The results show considerably higher ultimate flexural strength and energy absorption capacity under ring-on-ring test, and almost the same flexural strength at the quasi-elastic limit for both tests. An original analytical inverse analysis method for determining the biaxial tensile properties of strain-hardening UHPFRC from ring-on-ring test is developed based on yield line and slab bending theories. The inverse analysis results are validated against the experimental evidence, particularly based on DIC analysis. It shows a 18% lower elastic limit stress, and almost equivalent tensile strength of UHPFRC subjected to biaxial stresses, compared with the corresponding values from uniaxial stress. And a relatively small biaxial hardening strain is highlighted.

Finally, four series of biaxial flexural fatigue tests under constant amplitude fatigue cycles up to Very High Cycle Fatigue (20 million cycles) are conducted using circular slab-like elements. The fatigue stress level S (ratio of the maximum fatigue force to the ultimate quasi-static resistance of the slab specimen) is ranging from 0.50 to 0.68, targeting at the fatigue endurance limit and fatigue behavior of strain-hardening UHPFRC material under biaxial stress condition. The fatigue damage evolution is analyzed in terms of central deflection as well as development of fictitious crack propagation and opening. Based on the fatigue test results, a fatigue endurance limit at 20 million cycles is found at the stress level S=0.54 for UHPFRC circular slab elements under biaxial flexural fatigue. At this force level, the specimen is in the final part of its quasi-elastic domain of quasi-static flexural response, where a network of matrix discontinuities is largely developed in the UHPFRC material. And four phases of fatigue damage evolution characterize the fatigue behavior of UHPFRC specimens showing fatigue failure, while only the first two phases are identified for run-out specimens. Moreover, linear fatigue damage accumulation occurs in UHPFRC slab specimens showing fatigue fracture, irrespective of the fatigue loading level. The constant fatigue damage rate dD_n/dN_n is determined to be 0.26, which is 27% slower than the corresponding value obtained from direct tensile fatigue tests

Keywords: Strain-hardening UHPFRC, Fiber distribution, Uniformity factor, Matrix discontinuity, Direct tensile test (DTT), Ring-on-ring test, Biaxial stress condition, Digital image correlation (DIC), non-destructive test (NDT), Inverse analysis, Very high cycle fatigue (VHCF), Quasi-elastic limit, Thin slab element

Table of Contents

Symbols

Glossary

DIC	Digital Image Correlation
DTT	Direct Tensile Test
FEA	Finite Element Analysis
FRC	Fiber Reinforced Concrete
LCA	Life Cycle Analysis, Life Cycle Assessment
LVDT	Linear Variable Differential Transformer
NDT	Non-Destructive Test
RC	Reinforced Concrete
R-UHPFRC	Reinforced Ultra-High Performance Fiber Reinforced Cementitious Composites
RPC	Reactive Powder Concrete
UHPC	Ultra-High Performance Concrete
UHPFRC	Ultra-High Performance Fiber Reinforced Cementitious Composites
VHCF	Very High Cycle Fatigue
4PBT	Four-Point Bending Test

Latin uppercase letters

A_U	Area of the cross-section of UHPFRC
A_f	Area of the cross-section of a fiber
D	Elastic flexural stiffness of the slab
E_m	Modulus of elasticity of the UHPFRC matrix
E_f	Modulus of elasticity of the fibers
E_U	Modulus of elasticity of UHPFRC
E_{Uu}	Unloading modulus of UHPFRC when the tensile strength is reached
F	Measured force during testing
F_e	Measured force at the elastic limit during testing
$F_{fat,max}$	Imposed maximum fatigue load
$F_{fat,min}$	Imposed minimum fatigue load
F_{qe}	Measured force at the quasi-elastic limit during testing
F_p	Maximum measured force during testing
G_{Uf}	Dissipated energy per unit fracture surface during softening domain of UHPFRC
L_{MEA}	Measurement length for direct tensile test
N	Number of fatigue loading cycles
N_f	Absolute number of fibers crossing plane
R	Radius of support ring for ring-on-ring test

S	Fatigue loading level
S_r	Spacing of matrix discontinuities
V	Volume fraction
V_f	Volume fraction of fibers in UHPFRC mix
V_m	Volume fraction of matrix in UHPFRC mix
W_{ext}	External work
W_{int}	Internal work

Latin lowercase letters

b	width of UHPFRC test specimens
d_f	diameter of fiber
f_c	concrete compressive strength
f_{mt}	tensile strength of the matrix
f_{Ute}	elastic tensile strength of UHPFRC
f_{Utu}	tensile strength of UHPFRC
g_{Uf}	dissipated energy to generate matrix discontinuities per unit volume during hardening domain of UHPFRC
h	thickness of UHPFRC test specimens
l	total span of UHPFRC test specimens in test setup
l_f	fiber length
l	resistant moment per unit length
ℓ_{tr}	equivalent fiber anchorage length required to transmit tensile force
n_f	number of fibers crossing a unit area
q	shear force per unit length
r	radius of force transmitting ring for ring-on-ring test
v	the Poisson's ratio
w	opening of matrix discontinuity or fictitious crack
w_e	opening of matrix discontinuity at elastic limit
w_{qe}	opening of matrix discontinuity at quasi-elastic limit
w_p	opening of fictitious crack at maximum force

Greek lowercase letters

ε_{Ute}	strain in UHPFRC at elastic tensile strength
ε_{Utu}	strain in UHPFRC at tensile strength
$\varepsilon_{fat,max}$	imposed maximum strain at the initial quasi-static loading
δ	measured deflection during testing
δ_e	measured deflection at F_e during testing
δ_{qe}	measured deflection at F_{qe} during testing

δ_p	measured deflection at F_p during testing
θ	angle between the fiber and the main tensile stress direction
μ_0	fiber orientation factor
μ_1	fiber efficiency factor
μ_2	uniformity factor of fiber distribution
σ_{Ut}	tensile stress in UHPFRC
τ_f	maximum pullout stress of a straight fiber embedded in UHPFRC
$\sigma_{fat,max}$	imposed maximum fatigue stress
$\sigma_{fat,min}$	imposed minimum fatigue stress
a	ratio between the yielding zone and specimen height
φ	rotation angle of single segment
χ	curvature of slab

Introduction

1. Context

The concept of sustainability is nowadays respected in modern civil engineering projects relating to construction and rehabilitation of infrastructures (e.g. bridges and buildings), where minor environmental impact and low economic costs are required [1–6].

Globally, one-third of the final energy consumption is related with bridges and buildings, which contributes to almost one-quarter of greenhouse gas (GHG) emission worldwide [3]. This consumption becomes increasingly large attributed to two main facts. One comes from the population and traffic volume growth, suggesting the increase demand of new infrastructures. On the other hand, some existing structures are either reaching the end of their service life or become structurally deficient due to premature deterioration [7]. This is particularly so in the case of bridges. For example, 35% of bridges in Europe are older than 100 years [6]; 39% of bridges in US are more than 50 years old, of which 9.1% exhibit significant damage with considerable risk of failure [7]. These infrastructures thus need to be rehabilitated and improved to comply with current requirements in terms of ultimate, serviceability and fatigue limit states. In this regard, developing advanced materials and innovative construction technologies for construction and rehabilitation is of paramount importance.

Tensile strain hardening Ultra High-Performance Fiber Reinforced Cementitious Composites (UHPFRC) possess very appealing features to improve the effectiveness, durability and sustainability of new and existing structures, shown to be an advanced material towards the fulfilment of the concept of sustainable development. UHPFRC has extremely low permeability, relatively high strength (compressive strength ≥ 180 MPa, tensile strength ≥ 10 MPa) and good ductility in tension [8,9]. In addition, it is well acknowledged that UHPFRC shows fatigue endurance limit up to multimillion cycles under uniaxial tensile, flexural and compressive fatigue [10]. Currently, UHPFRC is available at an industrial scale and successfully applied in practice.

Regarding new structures, slenderness and lightweight generally represent UHPFRC structural elements for bridge and building applications (Figure 1). Worldwide, UHPFRC applications on innovative new structures develop rapidly under the impulse of pioneering countries such as Switzerland [8], China [11] and Malaysia [2]. As benefited from the high strength and ductility in tension, UHPFRC thin structural elements provide good resistance against bending, shear and fatigue resistance even without ordinary reinforcement [9,10,12]. Moreover, they often are prefabricated and transported easily, hence allowing a very fast construction on-site. Maintenance is largely reduced during the service life, given the high durability of UHPFRC materials. Consequently, significant material and energy savings are achieved when lightweight UHPFRC elements are applied.

UHPFRC is used to rehabilitate and strengthen structural members of reinforced concrete bridges with respect to resistance and durability. This method is based on the research works at MCS/EPFL since 1999 [8,13] (Figure 3) and has made its proof in engineering practice in Switzerland (Figure 2). The original concept is placing a relatively thin UHPFRC layer (with typical thickness of 40 to 60mm) on the top surface of specific zones of existing reinforced concrete (RC)

elements subjected to severe mechanical and environmental actions [8,13]. This technique is spreading widely in Switzerland (over 100 applications) under the impulse of MCS, and more recently in Slovenia, France, Japan and Germany under the supervision of MCS. This type of intervention, considered as "once for all" solution, can be accomplished in a rather short time frame, thus minimizing traffic interruptions, as well as reducing the environmental impact to lower than 50% compared with traditional methods as shown by Life Cycle Assessment (LCA) [4].
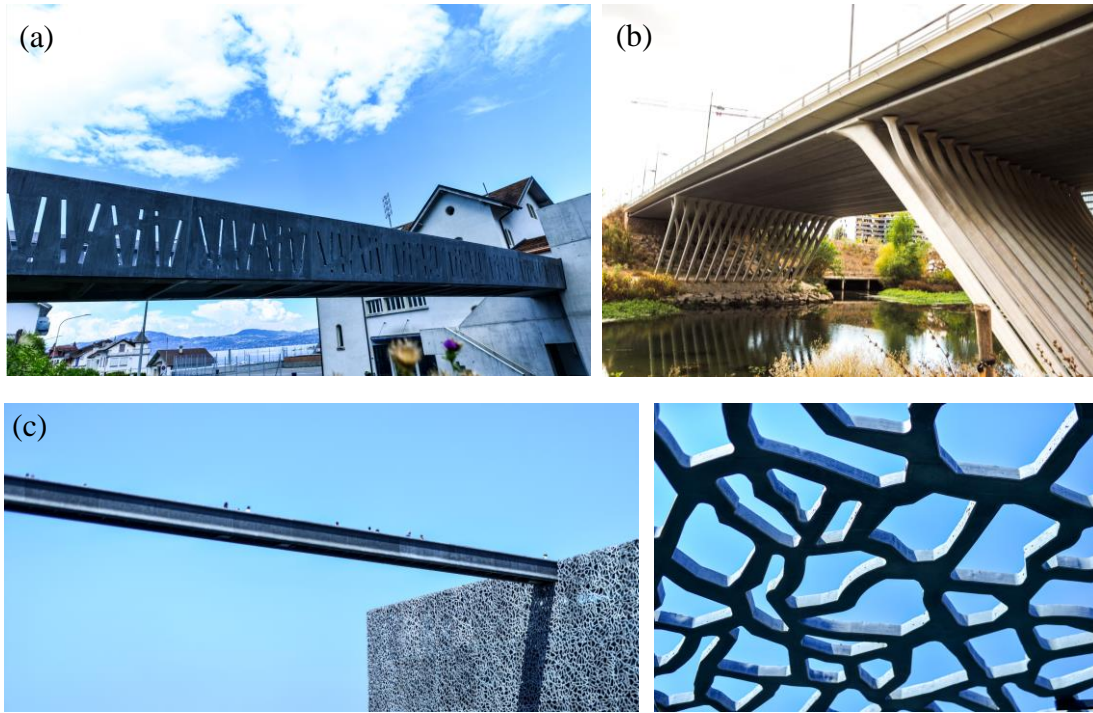
Figure 1 New structure using UHPFRC:
(a) Le Bouveret footbridge in Switzerland; (b) Republic road bridge in Montpellier, France;
(c) footbridge and façade elements in UHPFRC of the MUCEM building in Marseille, France

(b)

Figure 2 Rehabilitation using UHPFRC:
(a) Chillon viaduct after strengthening; (b) UHPFRC casting finisher

Habel, K. 2004
Structural Behavior of Elements Combining UHPFRC and RC
➢ Fundamental and general studies of UHPFRC properties
➢ Bending behavior and resistance of RU-RC members

Material Property

Structural Behavior

Fatigue Behavior

Kamen, A. 2007
Early-age and time-dependant behavior of a strain-hardening UHPFRC
➢ Early-age properties and thermo-mechanical behavior of UHPFRC

Switek, A. E. 2011
Time-Dependent Response of UHPFRC under Low to High Tensile Stresses
➢ Tensile creep behavior of UHPFRC

Kazemi-Kamyab, H. 2013
Autogenous Shrinkage and Hydration Kinetics of SH-UHPFRC
➢ Autogenous shrinkage of UHPFRC under moderate to low curing temperatures

Hafiz, M.A. 2019
Tensile response of Eco- Strain Hardening Ultra High Performance Fibre Reinforced Concretes under low temperatures and low loading rates
➢ Influence of low loading rates on tensile behavior of Eco-UHPFRC

Hajiesmaeili, A. 2019
Next Generation UHPFRC for a sustainable built environment
➢ New generation of UHPFRC with synthetic fibers and massive clinker replacement by limestone filler

Wuest, J. 2007
Structural Behavior of UHPFRC in Tension in Composite Elements
➢ Tensile response of UHPFRC
➢ Fiber orientation in UHPFRC

Oesterlee, C. 2010
Structural Response of R-UHPFRC and RC Composite Members
➢ Tensile response of UHPFRC and R-UHPFRC
➢ Bending behavior and resistance of RU-RC members

Noshiravani, T. 2012
Structural Response of R-UHPFRC - RC Composite Members Subjected to Combined Bending and Shear
➢ Bending behavior and shear resistance of RU-RC members

Bastien-Masse, M. 2015
Structural Behavior of R-UHPFRC - RC Composite Slabs
➢ Effect of fiber orientation on the tensile response of UHPFRC
➢ Punching and shear resistance of RU-RC slabs

Herwig, A. 2008
Reinforced Concrete Bridges under Increased Railway Traffic Loads: Fatigue Behavior and Safety Measures
➢ Fatigue behavior of RU-RC members

Makita, T. 2014
Fatigue Behavior of UHPFRC and RU- RC Composite Members
➢ Fatigue behavior of UHPFRC and R-UHPFRC in tension
➢ Fatigue behavior of RU-RC members

Loraux, C. 2018
Long term monitoring of existing wind turbines towers and fatigue resistance of UHPFRC under compressive stresses
➢ Compressive fatigue behavior of UHPFRC at a very high number of cycles

Shen, X. 2020
Static and Fatigue Flexural Behavior of UHPFRC Thin Slab Elements
➢ Influence of local fiber distribution on the tensile properties of UHPFRC
➢ Biaxial flexural/tensile behavior of UHPFRC thin slab element
➢ Biaxial flexural fatigue behavior of UHPFRC thin slab element

Figure 3 Previous researches and present work at MCS/EPFL [9,14–20]

2. Motivation and problem statement

A notable feature of UHPFRC subjected to uniaxial tension is the significant deformation capacity including hardening strain up to 5‰, where only matrix discontinuities in the bulk matrix are observed before reaching the tensile strength. Afterward, the pronounced softening behavior is characterized by the formation of one fictitious crack with major fracture energy dissipation. Figure 4 shows the schematic representation of uniaxial tensile response of strain-hardening UHPFRC.
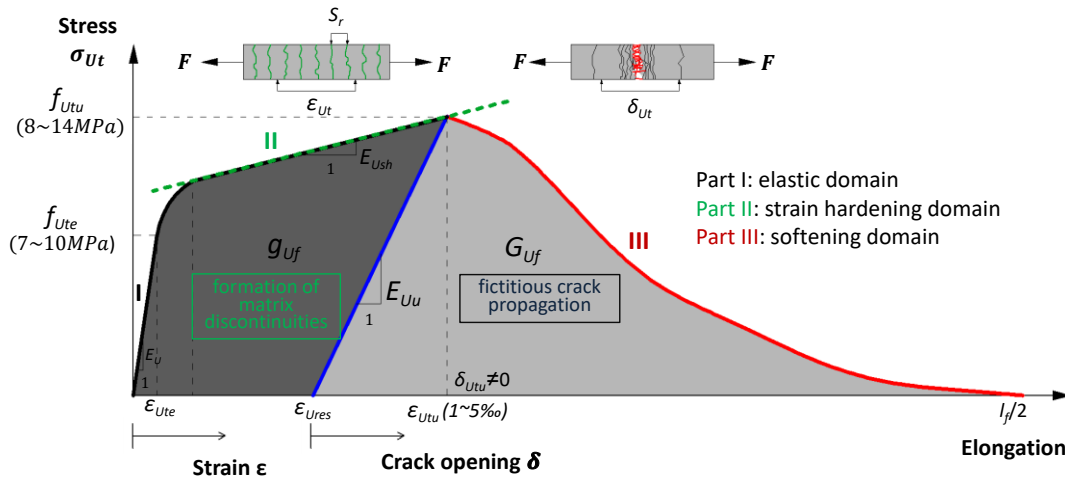
Figure 4 Schematic representation of the tensile response of strain-hardening UHPFRC (not in scale)

For a given UHPFRC mix, there are no intrinsic tensile properties, especially strain hardening response. The representative behavior is strongly dominated by the fiber distribution characterized by fiber volume fraction V_f, fiber orientation μ_0 and efficiency μ_1 within the UHPFRC specimen. Dispersion of tensile properties in UHPFRC thin elements is due to the wide range of μ_0 and μ_1 as determined by analysis of the fracture surface. This has been highlighted and investigated by several researchers [9,21–27]. Current studies mostly focused on the fiber orientation and efficiency factors μ_0 and μ_1 at the fracture surface and their influence on the tensile strength f_{Utu} under the assumption of uniform fiber distribution within UHPFRC volume. Only few studies considered the intrinsic heterogeneity of local fiber distribution, although it plays a key role in the strain hardening response of UHPFRC in tension. Thus, to identify the representative tensile properties in UHPFRC thin elements, the influence of local fiber distribution combined with fiber orientation and efficiency should be investigated quantitatively.

UHPFRC is generally used in slab-like structural applications with relatively thin thickness typically of 50mm. Such structural UHPFRC systems are subjected to biaxial stresses [28], exhibiting important stress redistribution capacity with high fracture energy dissipation. Moreover, in the case of bridge applications of UHPFRC as tensile reinforcement layer for existing RC bridge deck slabs and deck slabs of new UHPFRC bridges, a high number of repetitive loading due to passing vehicles occurs, typically exceeding several hundred million during the service life [29]. In this

context, comprehensive understanding of the biaxial static and fatigue behavior of slab-like UHPFRC elements representing actual structural conditions is necessary. However, to the best of the author's knowledge, only few studies have been carried out on the biaxial flexural behavior of UHPFRC slabs, and the biaxial fatigue behavior of UHFRC has not yet been investigated.

3. Objectives

With regards to the structural application of strain-hardening UHPFRC for bridge decks, the main objectives of this thesis is to understand and model the static and fatigue biaxial flexural behavior of UHPFRC slab elements representing actual structural conditions at both material and structural levels. This work is a continuation of 20 years of research on the topic at MCS/EPFL (Figure 3).

The following objectives are involved:

(1) To define quantitatively the local fiber distribution in strain-hardening UHPFRC thin slab element, and identify its influence combined with fiber orientation and efficiency on the tensile properties of UHPFRC with special emphasis on the strain-hardening behavior;

(2) To investigate the biaxial flexural behavior of strain-hardening UHPFRC thin slab elements using the ring-on-ring test method;

(3) To develop an analytical inverse analysis method based on ring-on-ring test results to determine the biaxial tensile properties of strain-hardening UHPFRC;

(4) To conduct an in-depth comparison between uniaxial and biaxial tensile properties of strain-hardening UHPFRC;

(5) To understand the biaxial flexural fatigue behavior of UHPFRC thin slab element at very high cycle fatigue (VHCF), typically exceeding 5 million fatigue cycles.

4. Methodology

As illustrated in Figure 5, four experimental campaigns are carried out, in which the strain-hardening UHPFRC thin slab-like element represents typical UHPFRC application on bridge decks as reinforcement layer or new structural element. The small UHPFRC plates extracted from thin slab elements are used for characterization of uniaxial tensile and flexural responses of UHPFRC by means of direct tensile tests (DTT) and four-point-bending tests (4PBT), respectively. Ring-on-ring tests are conducted to investigate the static and fatigue flexural behavior of UHPFRC slab elements subjected to biaxial stresses. Besides, the Digital Image Correlation (DIC) technique

is applied to capture the full-field damage propagation on the surface of specimens over the entire loading process.

Non-destructive test (NDT) method using a magnetic probe is applied to identify the local fiber distribution for each dumbbell specimens before conducting DTT. In order to prevent specimen eccentricities producing bending effects, the specimens are fixed in the testing machine by means of a special metallic device instead of conventional clamping.

Regarding the ring-on-ring test method, the circular slab element is simply supported on a ring support and loaded through a force transmitting ring. Thus, uniform tensile stress is introduced on the bottom surface of the slab within the force transmitting ring area, where biaxial stress condition is assumed. Totally, four quasi-static biaxial flexural tests are carried out; and fourteen biaxial flexural fatigue tests under constant amplitude fatigue cycles up to 20 million cycles are conducted with varying maximum fatigue stress level S (ratio of maximum fatigue stress to ultimate static resistance) ranging from 0.50 to 0.70.

An analytical inverse analysis method to determine the biaxial tensile properties of strain-hardening UHPFRC from the ring-on-ring test results is proposed based on the elastic slab bending and yield line theories. Ring-on-ring test and 4PBT results are compared with special emphasis on strength, ductility and characteristics of matrix discontinuity and fictitious crack development, according to experimental evidences and inverse analysis results.

The fatigue endurance limit of UHPFRC slab element under biaxial flexural fatigue is determined from the S-N diagram. Two types of fatigue test results (fatigue failure and run-out) are characterized individually based on DIC analysis in terms of central deflection, matrix discontinuity and fictitious cracks development. The scant modulus obtained from the force – deflection curve of each loading cycle is introduced as damage variable describing fatigue damage evolution.
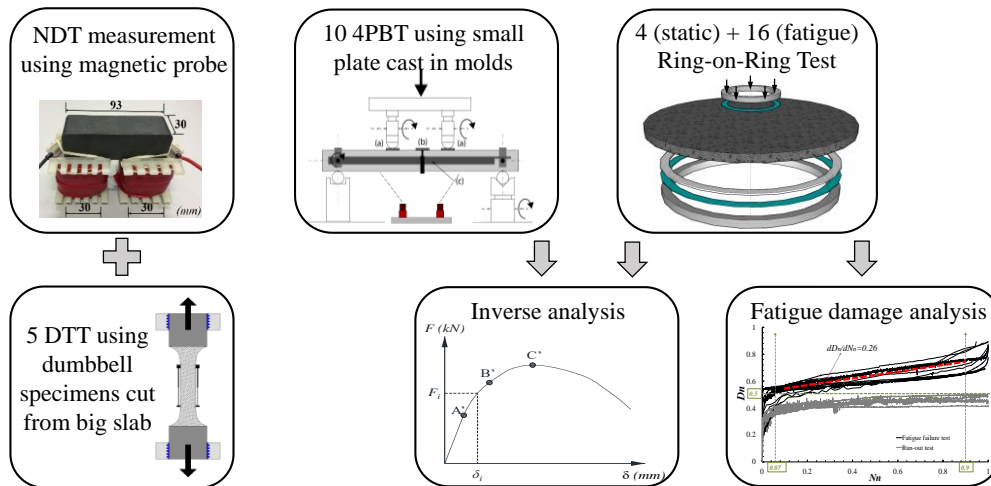
Figure 5 Experimental campaigns and analysis methods applied in present work

5. Outline

The thesis manuscript is presented as four distinct papers those have been published or submitted to internationally peer-reviewed scientific journals, accompanied with the introduction and conclusions chapters.

The four papers are:

I.   Influence of Local Fiber Distribution on Tensile Behavior of Strain Hardening UHPFRC using NDT and DIC *(Cement and Concrete Research 132 (2020): 106042.)*
      ⊥ This paper treats objective (1).

II.   Flexural Response of Strain-Hardening UHPFRC Circular Slab Elements Subjected to Biaxial Stresses *Construction and Building Materials, Volume 255, 20 September 2020, 119344)*
      ⊥ This paper treats objectives (2) and (4) experimentally.

III. An Analytical Inverse Analysis Method to Determine the Biaxial Tensile Properties of Strain-Hardening UHPFRC from Ring-on-Ring Test *(Submitted to Materials and Structures)*
      ⊥ This paper treats objectives (3) and (4) analytically.

IV.   Biaxial Fatigue Flexural Behavior of Strain-Hardening UHPFRC Thin Slab Elements *(Submitted to International Journal of Fatigue)*
      ⊥ This paper treats objective (5).

6. References

[1]   Sustainable Development & Energy | ASCE, (n.d.). https://www.asce.org/advocacy/energy/.

[2]   Voo Yen Lei, Foster Stephen J., Voo Chen Cheong, Ultrahigh-Performance Concrete Segmental Bridge Technology: Toward Sustainable Bridge Construction, Journal of Bridge Engineering. 20 (2015) B5014001.

[3]   B. Dean, J. Dulac, K. Petrichenko, P. Graham, Towards zero-emission efficient and resilient buildings.: Global Status Report, (2016).

[4]   K.F. Bizjak, A. Šajna, K. Slanc, F. Knez, Environmental life cycle assessment of railway bridge materials using UHPFRC, Materials and Geoenvironment. 63 (2016) 183–198.

[5]   G. Habert, E. Denarié, A. Šajna, P. Rossi, Lowering the global warming impact of bridge rehabilitations by using Ultra High Performance Fibre Reinforced Concretes, Cement and Concrete Composites. 38 (2013) 1–11.

[6]   J. Bien, L. Elfgren, J. Olofsson, Sustainable bridges : assessment for future traffic demands and longer lives, Dolnoslaskie Wydawnictwo Edukacyjne, 2007.

[7]   ASCE's 2017 American Infrastructure Report Card | GPA: D+. https://www.infrastructurereportcard.org.

[8]   E. Brühwiler, "Structural UHPFRC" to enhance bridges, in: Keynote Lecture, 2nd International Conference on UHPC Materials and Structures (UHPC 2018 - China), Fuzhou, China, 2018: pp. 140–158.

[9]   C. Oesterlee, Structural response of reinforced UHPFRC and RC composite members (doctoral thesis, 4848), École polytechnique fédérale de Lausanne (EPFL), 2010.

[10] T. Makita, E. Brühwiler, Tensile fatigue behaviour of ultra-high performance fibre reinforced concrete (UHPFRC), Mater Struct. 47 (2014) 475–491.

[11] X. Shao, L. Deng, J. Cao, Innovative steel-UHPC composite bridge girders for long-span bridges, Front. Struct. Civ. Eng. 13 (2019) 981–989.

[12] M. Bastien-Masse, E. Brühwiler, Experimental investigation on punching resistance of R-UHPFRC–RC composite slabs, Materials and Structures. 49 (2016) 1573–1590.

[13] E. Denarié, E. Brühwiler, Cast-on site UHPFRC for improvement of existing structures–achievements over the last 10 years in practice and research, in: 7th Workshop on High Performance Fiber Reinforced Cement Composites, 1-3, June 2015, Stuttgart, Germany, 2015.

[14] K. Habel, Structural behaviour of elements combining ultra-high performance fibre reinforced concretes (UHPFRC) and reinforced concrete, École polytechnique fédérale de Lausanne (EPFL), 2004.

[15] W. John, Comportement structural des bétons de fibres ultra performants en traction dans des éléments composés, Doctoral thesis No.3987, EPFL, 2007.

[16] T. Makita, Fatigue behaviour of UHPFRC and R-UHPFRC-RC composite members (doctoral thesis 6068), Doctoral thesis, École polytechnique fédérale de Lausanne (EPFL), 2014.

[17] M.A. Hafiz, Tensile response of Strain-Hardening Ultra High Performance Fiber Reinforced Concretes under low loading rates and low temperatures, Doctoral thesis No.7336, École polytechnique fédérale de Lausanne (EPFL), 2019.

[18] A. Hajiesmaeili, Next generation synthetic fibers UHPFRC for sustainable structural applications, EPFL, 2019.

[19] C.T. Loraux, Long-term monitoring of existing wind turbine towers and fatigue performance of UHPFRC under compressive stresses (doctoral thesis, 8404), École polytechnique fédérale de Lausanne (EPFL), 2018.

[20] M. Bastien Masse, Structural behavior of R-UHPFRC-RC composite slabs, EPFL, 2015.

[21] M. Bastien-Masse, E. Denarié, E. Brühwiler, Effect of fiber orientation on the in-plane tensile response of UHPFRC reinforcement layers, Cement and Concrete Composites. 67 (2016) 111–125.

[22] L.F.M. Duque, B. Graybeal, Fiber orientation distribution and tensile mechanical response in UHPFRC, Mater Struct. 50 (2017) 1–17.

[23] B. Zhou, Y. Uchida, Influence of flowability, casting time and formwork geometry on fiber orientation and mechanical properties of UHPFRC, Cement and Concrete Research. 95 (2017) 164–177.

[24] B. Zhou, Y. Uchida, Relationship between fiber orientation/distribution and post-cracking behaviour in ultra-high-performance fiber-reinforced concrete (UHPFRC), Cement and Concrete Composites. 83 (2017) 66–75.

[25] A. Abrishambaf, M. Pimentel, S. Nunes, Influence of fibre orientation on the tensile behaviour of ultra-high performance fibre reinforced cementitious composites, Cement and Concrete Research. 97 (2017) 28–40.

[26] S. Nunes, M. Pimentel, F. Ribeiro, P. Milheiro-Oliveira, A. Carvalho, Estimation of the tensile strength of UHPFRC layers based on non-destructive assessment of the fibre content and orientation, Cement and Concrete Composites. 83 (2017) 222–238.

[27] S. Nunes, M. Pimentel, A. Carvalho, Non-destructive assessment of fibre content and orientation in UHPFRC layers based on a magnetic method, Cement and Concrete Composites. 72 (2016) 66–79.

[28] J. Kim, D.J. Kim, S.H. Park, G. Zi, Investigating the flexural resistance of fiber reinforced cementitious composites under biaxial condition, Composite Structures. 122 (2015) 198–208.

[29] M. Rocha, E. Brühwiler, Prediction of fatigue life of reinforced concrete bridges using Fracture Mechanics, in: Proceedings Bridge Maintenance, Safety, Management, Resilience and Sustainability, CRC Press/Balkema, 2012: pp. 3755–3761.

Paper I

Influence of Local Fiber Distribution on Tensile Behavior of Strain Hardening UHPFRC using NDT and DIC

ABSTRACT

This paper introduces the uniformity factor μ_2 for considering the local fiber distribution within elements made with Ultra-High Performance Fiber Reinforced Cementitious Composites (UHPFRC). The influence of μ_2 on the strain-hardening response of UHPFRC under uniaxial tension is investigated quantitatively by means of experimental campaign and mechanical analysis. The uniaxial direct tensile test (DTT) was carried out on dumbbell specimens, extracted from a slab, to characterize the tensile behavior of UHPFRC using digital image correlation (DIC) system. Before DTT, actual fiber distribution of each specimen was measured by non-destructive test (NDT) method. Based on the present results and available literature, it is concluded that μ_2 plays a significant role in tensile strain-hardening response, especially hardening strain ε_{Utu} and matrix discontinuities energy g_{Uf}, of UHPFRC. The average μ_2 value for a given UHPFRC structural element is proposed to be applied for scaling the representative tensile response to intended applications.

1. Introduction

The tensile behavior of Ultra-High Performance Fiber Reinforced Cementitious Composites (UHPFRC) reveals strain-hardening response with non-visible multiple fine micro-cracks, hereafter called matrix discontinuities, with energy dissipation g_{Uf}, subsequently called hardening energy, in the bulk matrix before reaching the tensile strength f_{Utu}. Afterward, cracking concentrates in the fracture process zone while the specimen parts outside this zone are unloading; i.e, the softening behavior is characterized by the formation of a single discrete crack, hereafter called fictitious crack following the classical definition by Hillerborg [1], with significant fracture energy dissipation G_{Uf} [2,3]. A real crack is reached when the crack opening reaches about half of the fiber length ($l_f/2$). Figure 1 shows the schematic representation of tensile response of strain-hardening UHPFRC.
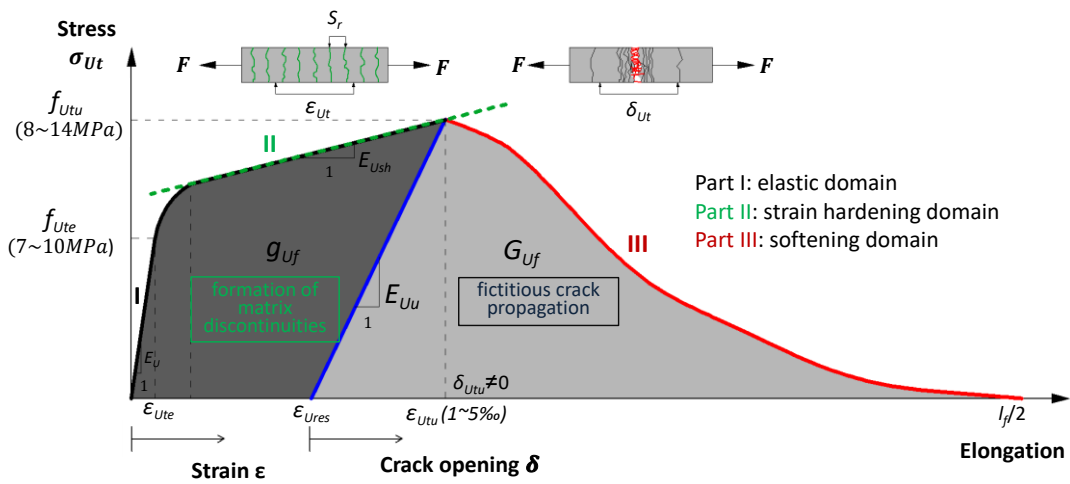
Figure 1 Schematic representation of tensile response of strain-hardening UHPFRC (not in scale)

Cast-in-place UHPFRC layer with typical thickness of 25~50mm is applied to specific zones of existing reinforced concrete (RC) elements subjected to severe mechanical and environmental actions. This strengthening method has been proven to be effective to enhance structural members in terms of resistance and durability [2,4] (Figure 2). In such applications, the UHPFRC layer, serving as tensile reinforcement, resists bending and shear forces in the UHPFRC-RC composite elements through its in-plane tensile resistance and deformability [2,5,6]. As a general rule, the serviceability of the composite structure is defined by a criterion for the deflection and impermeability of the UHPFRC layer. In the case of elements with requirement of water-tightness of severely exposed structural elements like bridge deck slabs, the allowable deformation in strain-hardening UHPFRC is limited to 1.3‰, as proposed by Charron et al. [7]. For design purposes, this threshold is set to be 1.0‰ at serviceability limit state (SLS) in UHPFRC standard SIA 2052 [8]. At ultimate limit state (ULS), the flexural resistance of composite elements is dominated by the yielding of steel rebars in UHPFRC layer [6,9], in which most parts of the UHPFRC cross section is in the strain-hardening domain. The strain-hardening response of UHPFRC is thus of

utmost importance in both SLS and ULS of composite elements, and therefore it needs to be characterized representatively and accurately.
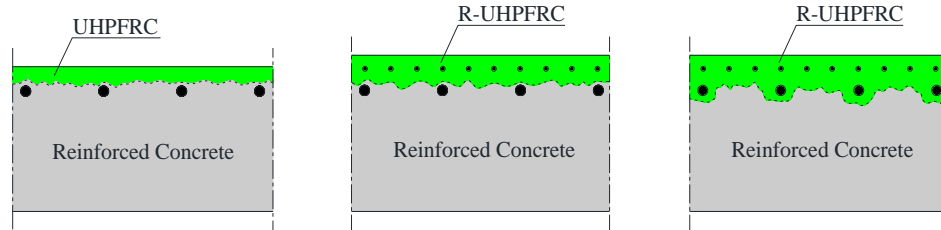
Figure 2 Application of UHPFRC as thin tensile reinforcement layer [2]

For a given UHPFRC mix, there are no intrinsic tensile properties. The representative behavior is strongly dominated by the fiber distribution characterized by fiber volume fraction V_f, fiber orientation μ_0 and efficiency μ_1 within the UHPFRC element. The fiber distribution depends on the casting method, flow direction of fresh mixture, finishing process, geometry and dimension of formworks [9–16].

As summarized in Table 1, the large dispersion of tensile properties in UHPFRC elements due to the wide range of fiber orientation and efficiency factors μ_0 and μ_1 as determined by analysis of the fracture surface, have been highlighted and investigated by several researchers [9–13,17–19]. In most studies, the tested specimens have small thickness (≤ 50 mm), and are extracted from large UHPFRC panels fabricated using various casting methods. These casting methods were found to be representative for numerous UHPFRC applications, e.g., tensile reinforcement layer for existing RC structure or thin precast elements [2,4,20]. Fiber orientation and efficiency factors certainly avoid overestimating the available strength and deformation in real structural applications since favorable fiber orientation in narrow laboratory specimens are normally regarded as an upper bound [15]. Currently, reduction factors for tensile strength f_{Utu} considering this well-known fiber orientation aspect are introduced in UHPFRC design standards like SIA 2052 [8] and NF P18-710 [21].

However, current studies mostly focused on the fiber orientation and efficiency factors μ_0 and μ_1 at the fracture surface and their influence on the tensile strength f_{Utu} of UHPFRC under the assumption of uniform fiber distribution. Only few studies considered local fiber distribution within UHPFRC. The intrinsic heterogeneity of local fiber distribution, as well as its influence on the tensile response, is already verified and highlighted for fiber reinforced cementitious composites in [22–24]. Pimentel et al. [25] also detect similar heterogeneity of fiber distribution within UHPFRC layer based on NDT method, and find that it is necessary to consider the local fiber distribution in order to reproduce accurately the structural response of UHPFRC layer under flexure. Hadl et al. [26,27] show that the large scattering in flexural behavior of UHPFRC members mainly results from the variation of local fiber volume fraction in the UHPFRC element. To the best of the authors' knowledge, the local fiber distribution has not yet been characterized quantitatively, and no extensive research is available in the literature about its influence on the strain-hardening response of UHPFRC in tension. These aspects are of paramount importance

for better understanding the tensile fracture mechanism, as well as permeability [7], of UHPFRC subjected to tensile stress.

Table 1 Review of experimental fiber orientation factors and related tensile parameters [a]

Reference	Specimen Fabrication	Straight steel fibers			Testing method[b]	Orientation effect		Tensile parameters		
		V_f (%)	l_f (mm)	d_f (mm)		μ_0 [d]	$\overline{\mu_1}$ [e]	f_{Utu} (MPa)	ε_{Utu} (‰)	G_f (kJ/m²)
Abrishambaf et al. [17]	Individual specimens Orient fibers in a magnetic field 430×40×30 mm	3.0	9.0 — 12.0	0.175	DTT Image analysis	0.45 ~ 0.71	0.89 ~ 0.98	6.38 ~ 14.05	1.3 ~ 4.7	4.10 ~ 17.07
Bastien-Masse et al. [10]	Extracted specimens Horizontally cast panel from one edge 580×580×50 mm 1000×1000×50 mm	3.0	13.0	0.16	DTT Eq.(1)	0.39 ~ 0.60	0.86 ~ 0.95	5.50 ~ 9.20	0.28 ~ 2.01	-
					4PBT Eq.(1)	0.37 ~ 0.89	0.85 ~ 1.00	5.50 ~ 14.60	0.54 ~ 5.08	-
Duque et al. [11]	Extracted specimens Horizontally cast panel from one end 3048×914×50.8 mm	2.0	12.7	0.20	DTT Image analysis	0.37 ~ 0.72	0.84 ~ 0.99	6.60 ~ 13.0	2.30 ~ 7.80	-
Oesterlee [9]	Extracted specimens Vertically cast panel from top end 3000×1500×50 mm	3.0	13.0	0.16	DTT Image analysis	0.19 ~ 0.79	0.48 ~ 1.00	2.90 ~ 14.90	3.30 ~ 6.10	-
Zhou et al. [12,13]	Extracted specimens at different angles Horizontally cast circular panel from center Φ1200×50mm	2.0	15.0	0.20	3PBT Image analysis	0.09 ~ 0.57	0.23 ~ 0.94	-	-	-
Nunes et al. [18,19]	Individual specimens Orient fibers in a magnetic field 304×150×25 mm	3.0	9.0 — 12.0	0.175	DEWS [c] test NDT	0.28 ~ 0.81	0.72 ~ 1.00	16.54 ~ 3.27	-	-

[a] only the testing data of strain hardening UHPFRC in this review
[b] tensile test method and fiber orientation measurement method
[c] Double-Edge Wedge Tensile test
[d] The fiber orientation factor μ_1 is determined using equation (2) according to the number of fibers provided in [12,13]
[e] The fiber efficiency factor μ_1 is determined based on Figure 3(b)

The objective of present study is to determine and investigate quantitatively the influence of local fiber distribution on the tensile behavior of UHPFRC. Special emphasis is given on the strain-hardening response, by means of an extensive experimental campaign using a specific UHPFRC mix. Firstly, the NDT method using a magnetic probe is applied for investigating the local fiber distribution within a 50mm thick slab element. Afterward, the representative tensile response is

characterized using direct tensile test (DTT) method and Digital Image Correlation (DIC) system. The test results are used to characterize the degree of uniformity of local fiber distribution in UHPFRC by introducing the uniformity factor μ_2. Then the influence of μ_2 on the strain-hardening response of UHPFRC is investigated and validated against literature data. Finally, the representative uniformity factor and tensile behavior are determined for the UHPFRC layers with different thicknesses.

2. Strain-hardening response of UHPFRC

2.1 Overview

A notable feature of UHPFRC in uniaxial tension is the significant strain-hardening domain, where only smeared discontinuities in the bulk matrix appear. This domain is characterized by tensile stress varying between the elastic and tensile strength, the corresponding hardening strain, as well as the number and spacing of matrix discontinuities, matrix discontinuity opening, and energy absorption [3,17,28].

In the following, these parameters characterizing the strain-hardening domain and fiber distribution of UHPFRC are described briefly, and the uniformity factor accounting for the degree of uniformity of local fiber distribution is introduced.

2.2 Tensile strength

2.2.1 Basic formulation

For a given strain-hardening UHPFRC, the tensile strength is determined by the well-known fiber orientation factor μ_0 and efficiency factor μ_1 valid for the fracture zone. The corresponding Equation 1 is proposed and applied by different authors [29,30]:

$$f_{Utu} = \mu_0 \mu_1 \tau_f V_f \frac{l_f}{d_f} \tag{1}$$

where τ_f is the maximum pull-out stress or bond strength between fibers and the cementitious matrix, V_f is the fiber volume fraction, and l_f/d_f is the aspect ratio of fibers.

2.2.2 Fiber orientation factor

The fiber orientation factor μ_0 is defined as the probability of a single fiber being intersected by a considered section, obtained by the ratio between the real number of fibers crossing a unit area n_f and the nominal one (Equation 2), where A_f is the cross section of a fiber [10,31]:

$$\mu_0 = n_f \frac{A_f}{V_f} \tag{2}$$

Based on stereological analysis [10,31,32], $\mu_0 = 1.0$ is for unidirectional fibers in the tensile direction (1D), and $\mu_0 = 2/\pi$ is for fibers oriented randomly in an ideal plan (2D). $\mu_0 = 0.5$ is

for fibers oriented randomly in volume (3D). A wide variation of μ_0 values is observed (Table 1), and average values are found to be in the range of 0.53~0.60 for UHPFRC specimen with a thickness of 50mm [10].

2.2.3 Fiber efficiency factor

The fiber efficiency factor μ_1 is defined as the expected value of the fiber efficiency function according to Equation 3, where $g(\theta)$ is the ratio between the pull-out force of an inclined fiber with angle θ with respect to the main stress direction and that of a perfectly aligned one, and $f_i(\theta)$ is the probability density function of the orientation angle θ of the fibers crossing the considered section:

$$\mu_1 = \int_0^{\frac{\pi}{2}} g(\theta) f_i(\theta) \, d\theta \tag{3}$$

As shown in Table 1, a relatively small variation of μ_1 values is observed for thin UHPFRC specimens. This is attributed to the fact that the orientation angle θ in a wide range influences little the pull-out force, as shown experimentally by several researchers (Figure 3a) [3,9,29,33]. One simplified function, proposed by C. Oesterlee [9], is plotted in Figure 3a: $g(\theta) = 1.0$ when $\theta \leq \frac{\pi}{3}$; $g(\theta) = -\left(\frac{6\theta}{\pi}\right) + 3$ when $\frac{\pi}{3} < \theta \leq \frac{\pi}{2}$. The calculated μ_1 based on [9], hereafter, is called average fiber efficiency factor $\overline{\mu_1}$. Bastien-Masse et al. [10] established a relation between the average efficiency factor $\overline{\mu_1}$ and the orientation factor μ_0 based on stereological principles, as illustrated in Figure 3b. Note that the influence of $\overline{\mu_1}$ on the tensile strength decreases gradually when $\mu_0 \geq 0.28$; and once $\mu_0 \geq 0.75$, the influence is negligible when $\overline{\mu_1}$ is equal to 1.0.
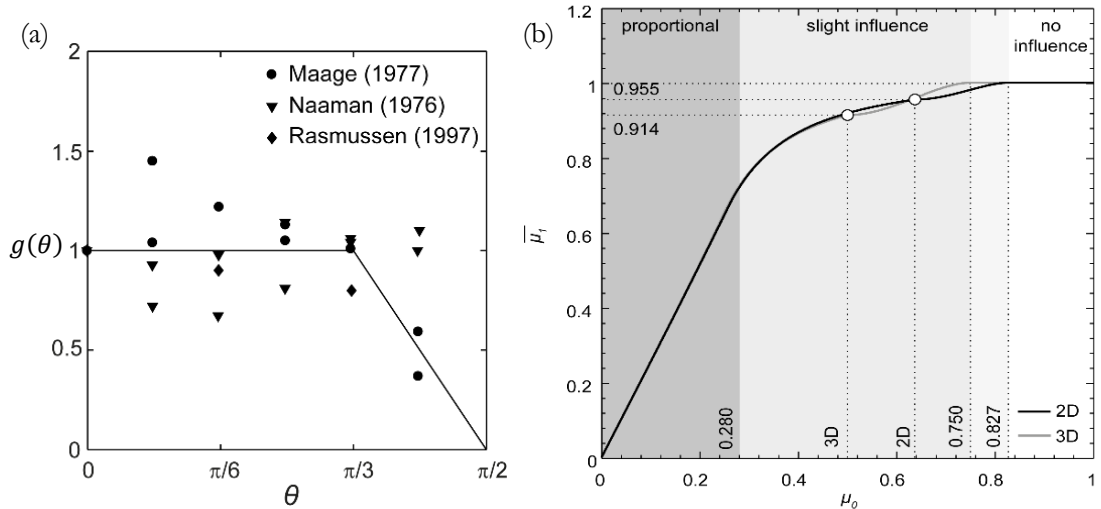
Figure 3 (a) Fiber efficiency depending on the pull-out angle; (b) relation between μ_0 and μ_1 [9,10]

2.2.4 Estimation of μ_0 and $\overline{\mu_1}$

To determine the representative values of μ_0 and $\overline{\mu_1}$ for a given UHPFRC specimen or element, the method of image analysis on cut specimen surfaces was extensively applied in the literature [9–11,16–18,34–37], although it is time-consuming. Alternatively, several non-destructive testing (NDT) methods, including magnetic measurement [18,19,38,39], electrical resistivity measurement [40] and AC-impedance spectroscopy [37,41], have been developed for fast estimation of μ_0 and μ_1 in both UHPFRC laboratory specimens and structural elements. These NDT methods have potential for quality control in UHPFRC applications. In this paper, the NDT method using a magnetic probe, developed in [19,42], is applied in section 3.2.

2.3 Matrix discontinuities

As proposed by several researchers [30,38,39], the spacing (S_r) of matrix discontinuities is associated directly with the equivalent fiber anchorage length (ℓ_{tr}) required to transmit tensile force. S_r varies between ℓ_{tr} and $2\ell_{tr}$, and is generally set as $1.5\ell_{tr}$.

Following the assumption by Aveston et al. [43], the tensile stress is sustained by fibers only once matrix discontinuities form (beyond the elastic limit). Thus, at each matrix discontinuity:

$$\sum_{i=1}^{N_f} \ell_{tr}\pi d_f \tau_{f,i} = f_{mt} A_U (1 - V_f)$$ (4)

where N_f is the absolute number of fibers at the surface of the considered matrix discontinuity, and proportional to fiber orientation factor μ_0, see Equation 2; $\tau_{f,i}$ is the pull-out stress of i-th fiber, and proportional to fiber efficiency factor μ_1, see Equation 3; f_{mt} is the tensile strength of the matrix, and A_U is the cross-section area.

With Equations 2 and 3, Equation 4 transforms as follows to obtain the anchorage length ℓ_{tr} for the considered matrix discontinuity:

$$n_f \ell_{tr}\pi d_f \overline{\mu_1}\tau_f = f_{mt}(1 - V_f)$$ (5)

$$\ell_{tr} = \frac{f_{mt}d_f(1-V_f)}{4\mu_0\overline{\mu_1}\tau_f V_f}$$ (6)

Then, the potential spacing $S_{r,i}$ for i-th matrix discontinuity is determined:

$$S_{r,i} = 1.5\ell_{tr,i} = \frac{3f_{mt}d_f(1-V_{f,i})}{8\mu_{0,i}\overline{\mu_{1,i}}\tau_f V_{f,i}}$$ (7)

where $\ell_{tr,i}$, $V_{f,i}$, $\mu_{0,i}$ and $\mu_{1,i}$ are determined from the surface of considered matrix discontinuity.

Since the local fiber distribution varies within UHPFRC [25–27], the anchorage length and spacing differ at each matrix discontinuity. In addition, the matrix discontinuities are expected to appear mainly on the local weak zones with relatively unfavorable fiber distribution, while the matrix discontinuities at the remaining part cannot fully develop since the tensile strength is reached at

one or several of the weak zones. Thus, the average spacing $\overline{S_r}$ largely depends on the degree of uniformity of local fiber distribution. Considering this, an uniformity factor μ_2 is introduced to obtain $\overline{S_r}$:

$$\overline{S_r} = \frac{S_{r,c}}{\mu_2} = \frac{3 f_{mt} d_f (1 - V_f}{8 \mu_0 \mu_1 \mu_2 \tau_f V_f} \tag{8}$$

where $S_{r,c}$ is the spacing determined from the critical matrix discontinuity leading to the final crack of the specimen.

As illustrated schematically in Figure 4, $\mu_2 = 1.0$ when all fibers within UHPFRC are oriented and spaced equally, referring to homogeneous material in loading direction; otherwise $\mu_2 < 1.0$ (anisotropy). A similar concept was proposed simply in [35,36] to consider the discontinuous fiber distribution, where a constant value of 0.4 was introduced. The uniformity factor μ_2 has direct impact on the spacing and number of matrix discontinuities, and thus the deformation capacity of UHPFRC under tension.
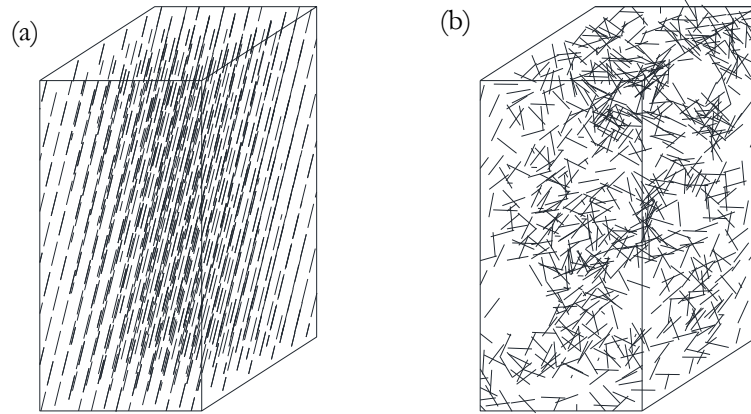
Figure 4 Schematic representation of the uniformity factor: (a) $\mu_2 = 1.0$; (b) $\mu_2 < 1.0$.

2.4 Energy absorption

Following the basic concept introduced by Hillerborg [45], the energy absorption of UHPFRC in tension is divided into two different parts, namely matrix discontinuities energy g_{Uf} and fracture energy G_{Uf}, as illustrated in Figure 1. g_{Uf} is defined as the amount of dissipated energy to generate matrix discontinuities per unit volume. This energy depends on the number of matrix discontinuities, and can be regarded as a parameter evaluating the strain-hardening performance of UHPFRC [3,46]. G_{Uf} is the dissipated energy per unit fracture surface during softening. The two energy values are determined as follows:

$$g_{Uf} = \int_0^{\varepsilon_{Utu}} \sigma(\varepsilon) \, d\varepsilon - \frac{1}{2} \frac{f_{Utu}^2}{E_{Uu}} \tag{9}$$

$$G_{Uf} = \int_{\delta_{Utu}}^{l_f/2} \sigma(\delta)\, d\delta + \frac{1}{2}\frac{f_{Utu}^2}{E_{Uu}} L_{MEA} \qquad (10)$$

where E_{Uu} is the unloading modulus when the tensile strength is reached, it can be determined according to [3]: $E_{Uu} = 1000V_f + 3900\,[MPa]$; L_{MEA} is the mearuement length.

3. Experiments

3.1 Specimen design and preparation

The tested UHPFRC is an industrial premix containing 3.8% by volume of straight steel fibers with length of 13mm and diameter of 0.175mm, and its water to cement ratio is 0.15 (Table 2). At 28 days, the UHPFRC has average elastic modulus of 49GPa and compressive strength of 185MPa, measured on cylinders of 70mm diameter. One slab element (T1) with dimensions of 1100mm × 1100mm × 50mm was fabricated.

Table 2 Composition of UHPFRC

Components		Quantity
Premix (cement. Additions, quartz sand)		1970
Water	kg/m³	175
Specific superplasticizer		29
Steel fibers ($l_f/d_f = 13/0.175$, $V_f = 3.8\%$)		298.3

The fresh self-compacting UHPFRC (with slump flow of 700mm) was poured on the center area of the formwork from where it has flown (without any pulling or vibration) to fill entirely the formwork. After casting, a plastic sheet was pulled over the slab to allow for curing. The formwork was removed 24 hours later. The slab was then kept under moist curing conditions at 20℃ and 100% humidity during the following seven days, and subsequently was stored inside the laboratory until testing. The age at testing was more than 60 days when over 90% of the UHPFRC final material properties were attained [6,47].

At the age of 60 days, five dumbbell specimens for DTT were cut from the slab as shown in Figure 5. Each specimen had a length of 880mm with a constant cross section of 80mm × 50mm that extended over 240mm in the central part. The wider end zones were prepared for fixing the specimen in the testing machine. The Neuber's spline [48] was adopted to design the transition from the wider end zone to the central width of the specimen.

3.2 Non-destructive testing (NDT) using a magnetic probe

A high-precision Agilent E4980A LCR Meter with test frequency of 20Hz and signal level of 2V (AC) was used to measure inductance using a magnetic probe. Inductance measurements were performed on the slab before cutting the DTT specimens (Figure 6). The inductance measurement

was conducted largely on the central area of the specimens on both surfaces along two orthogonal directions (X and Y). It should be mentioned that the casting surface of the slab was polished ahead to remove the uneven part. The distance between each measurement point was 25mm in X direction and 30mm in Y direction (based on the size of the magnetic probe). Totally, 48 pairs of measurements were carried out for each DTT specimen along both orthogonal directions. The Y-direction was selected to be aligned with the main tensile force direction. The inductance measurement along two directions and, for the purpose of reference, in the air are defined as L_x, L_y and L_{air}, respectively. Accordingly, the relative magnetic permeability in two directions is given by $\mu_{r,x} = L_x/L_{air}$ and $\mu_{r,y} = L_y/L_{air}$.
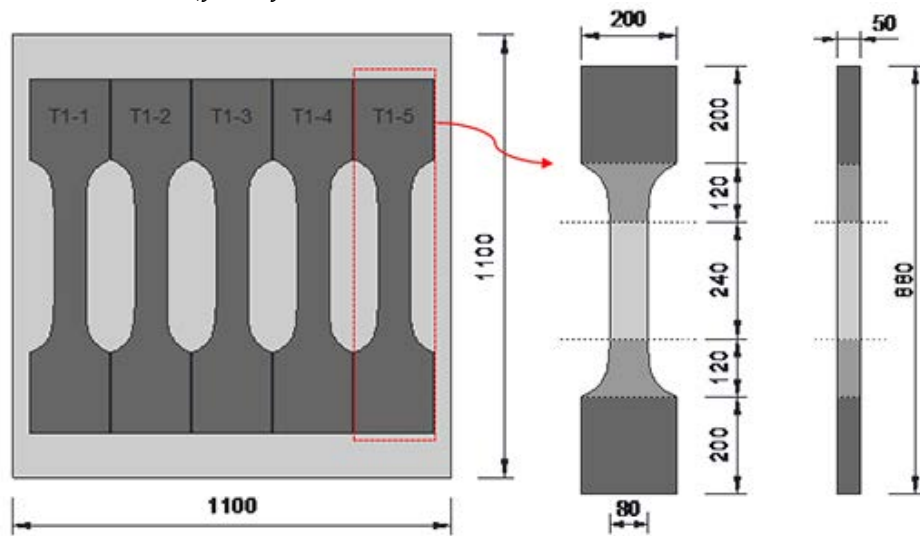
Figure 5 Dumbbell specimens for DTT cut from quadratic slab element (unit: mm)
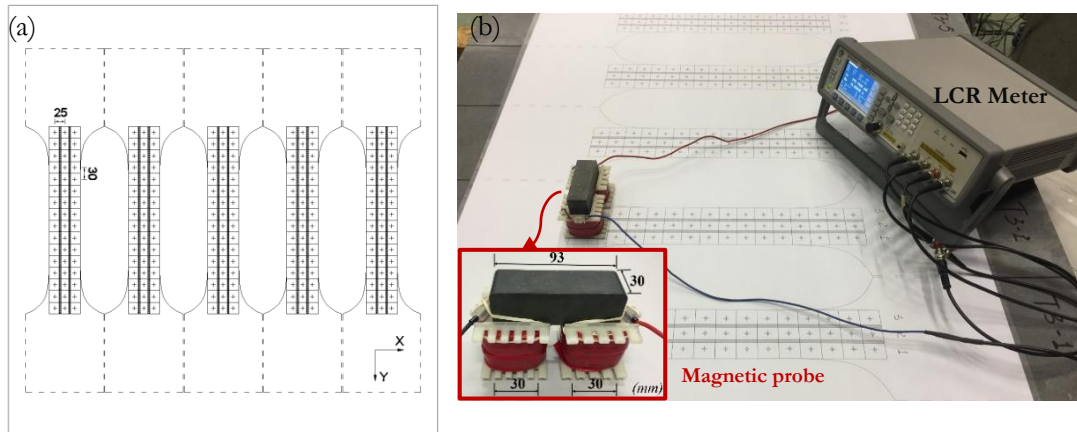
Figure 6 Inductance measurement using a magnetic probe:
(a) location and direction of measurements; (b) test setup (unit: mm)

3.3 Direct tensile test (DTT)

In order to prevent specimen eccentricities producing bending effects in the specimen due to clamping of the specimen in the test machine, the DTT specimens were fixed in the testing machine by means of a special metallic device for specimen fixation described in [49]. As illustrated in Figure 7, the space between specimen and metallic device was filled out with epoxy resin glue. Prior to applying the glue, the metallic surface was coated with release agent avoiding adherence between glue and metallic device. Thus, through interlocking, the tensile force was introduced to the UHPFRC specimen via the teeth formed by the glue along the lateral surface. Both the bottom and top steel base plates were tightly bolted on the machine's heads without any hinge. In this way, the boundary condition of the DTT specimen at its ends was of full fixity to allow for stable propagation of matrix discontinuities and fictitious cracks under uniform tensile deformation.

In order to avoid specimen failure in the transition zone and following an idea proposed by Graybeal et al. [17,50], four tapered aluminum plates were affixed on the sides of each specimen's wider heads. These plates were 4 mm thick and were tapered linearly to 0.5mm of thickness at tip over a length of 50mm (Figure 8).
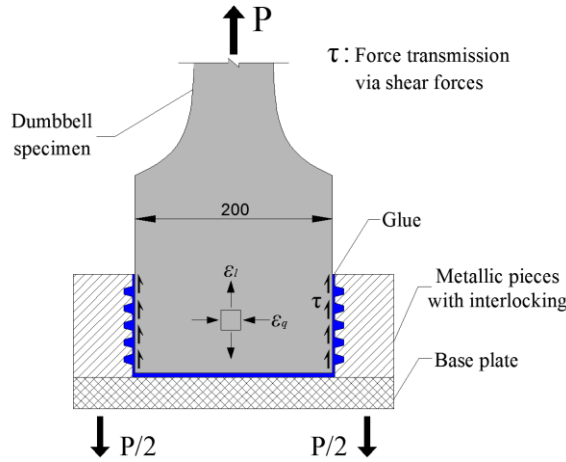
Figure 7 Device for the fixation of the DTT in the testing machine (unit: mm)
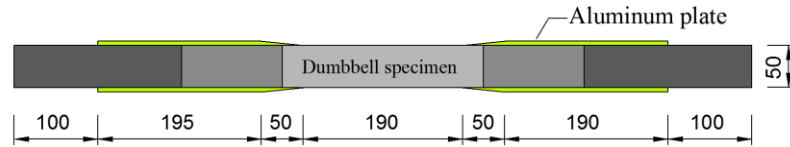
Figure 8 DTT specimen strengthened in the transition zone using aluminum plates (unit: mm)

The DTT was performed on a servo-hydraulic testing machine with a capacity of 1000kN. The 3D Digital Image Correlation (DIC) system and two different series of sensors were adopted to measure the deformation and fracture process of UHPFRC during testing (Figure 9):

(1) By means of the DIC technique, full-field strains and fracture process were observed during the whole test. Two digital cameras were placed vertical to the specimen at a distance of

0.45m and an angle of 20 degree to the horizontal plane. The targeted area was 150mm × 80mm on the sheathed surface at the central part of the specimen. During preparation, this surface was painted with matte white paint, and then sprayed to obtain a black speckle pattern with a size of about 0.5mm. For the present case, the expected DIC measurement accuracy was about 0.5μm.

(2) Two short Linear Variable Displacement Transducers (LVDTs) with a measuring base of 240 mm were placed on both narrow sides of the specimen to measure the global deformation over the central part of the specimen with constant width;

(3) Two long LVDTs with a measuring base of 500 mm were fixed on both narrow sides of the specimen to measure the global deformation over the total length of the specimen.

The test was displacement-controlled using the average value of the 2 short LVDTs to obtain stable specimen response during the entire test. The displacement rate was 0.05 mm/min in the pre-peak domain. In the post-peak domain, it was increased to 0.1 mm/min. The recordings of the two cameras of the DIC system were synchronized via wired computer control with a frequency of 0.2 Hz, while the recording by the other sensors was 5 Hz.
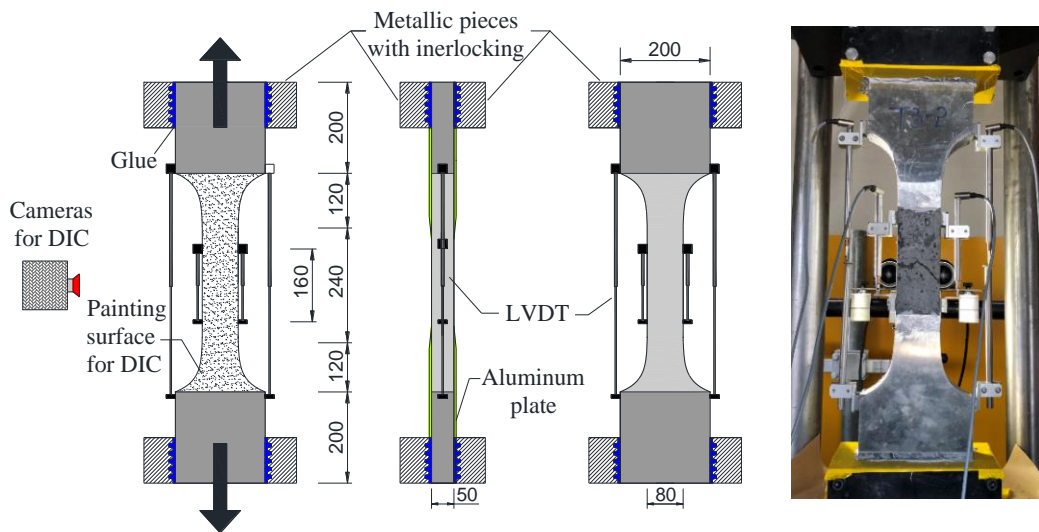
Figure 9 DTT setup and instrumentation of the specimen (unit: mm)

4. Test results

4.1 Local fiber distribution within UHPFRC specimens

For a given UHPFRC with steel fibers, Nunes et al.[18,42] determined the mean relative magnetic permeability ($\mu_{r,mean}$) and the fiber orientation indicator ($\rho_X - \rho_Y$) from the inductive measurements in two orthogonal directions. The two properties have linear relationship with the

fiber volume fraction V_f and orientation factor μ_0, respectively. The corresponding formulations are shown in Equations 10 to 13, where the equation 12 is slightly adapted by using a value of 4.55 as obtained by calibration, because of the different magnetic probe applied in the present study. Then the efficiency factor μ_1 is determined based on the curve shown in Figure 3(b) [10]. Note that local fiber distribution within each measured area (25×30mm) is assumed to be uniform, and the results based on Equations 11 to 14 are approximate estimation.

$$\mu_{r,mean} = (\mu_{r,X} + \mu_{r,Y})/2 \tag{11}$$

$$V_f = (\mu_{r,mean} - 1)/4.55 \tag{12}$$

$$(\rho_X - \rho_Y) = 0.5 \frac{\mu_{r,X} - \mu_{r,Y}}{\mu_{r,mean} - 1} \tag{13}$$

$$\mu_0 = 0.57 + 1.85(\rho_X - \rho_Y) \tag{14}$$

Accordingly, Figures 10 and 11 show the contour maps of local fiber volume fraction V_f, orientation factor μ_0 and efficiency factor μ_1 for each specimen based on NDT measurements from both casting and sheathed surfaces. Besides, the corresponding mean values and coefficient of variations $\hat{c}_v$ for each specimen and the whole slab are summarized in Table 3. It should be mentioned that the measured average fiber volume fraction in the slab is 3.7%, close to the nominal value 3.8%.

Compared with μ_0 and μ_1, the local fiber volume fraction V_f scatters in a smallest range, giving $4.2\% \leq \hat{c}_v \leq 12.1\%$ (Figure 10). The slightly higher and more uniform distribution of V_f from the sheathed side measurement than those from casting side can be attributed to: (1) fibers in the bottom part of the slab element tended to settle parallel to the bottom due to wall effect, and (2) fibers in the upper part were oriented slightly vertically due to the flow of fresh UHPFRC as also reported in [6].

As illustrated in Figure 11, the most significant anisotropy $(11.9\% \leq \hat{c}_v \leq 22.5\%)$ is observed for the fiber orientation factor μ_0 within the slab. Specimens T1-2, T1-3 and T1-4 cut from the area around the pouring point of fresh UHPFRC show larger scatter of μ_0. Whereas T1-1 and T1-5 with longest distance from the pouring point show small scatter and higher mean values of μ_0, indicating progressive fiber rotation with preferential alignment perpendicularly with respect to the flow direction. The fiber efficiency factor μ_1 shows similar trends with μ_0, although the scatter is smaller.

Assuming uniform local fiber distribution $(\mu_2 = 1.0)$ within each measured area (25×30mm) using the magnetic probe, the parameter $\lambda = V_f \mu_0 \mu_1$ is introduced here as a scalar description of local fiber distribution for each measured area in UHPFRC with respect to the tensile loading direction. The contour maps of normalized λ values are illustrated in Figure 13, where a low value refers to a weak zone in terms of tensile performance based on Equation 1. Similarly, large variation of λ can be observed in T1-2 to T1-4, whereas relatively uniform and high values of λ are found in T1-

1 and T1-5. It should be noted that a linear weak zone crossing the whole section in T1-5 and a large weak zone in T1-3 on the casting surface are observed, as indicated by red dashed lines in Figure 13(a). Furthermore, the expected fracture process zone with the discrete softening crack of each specimen is predicted according to the smallest values of λ within the central specimen zone, for both specimen surfaces, as indicated by grey bold lines in Figure 12.
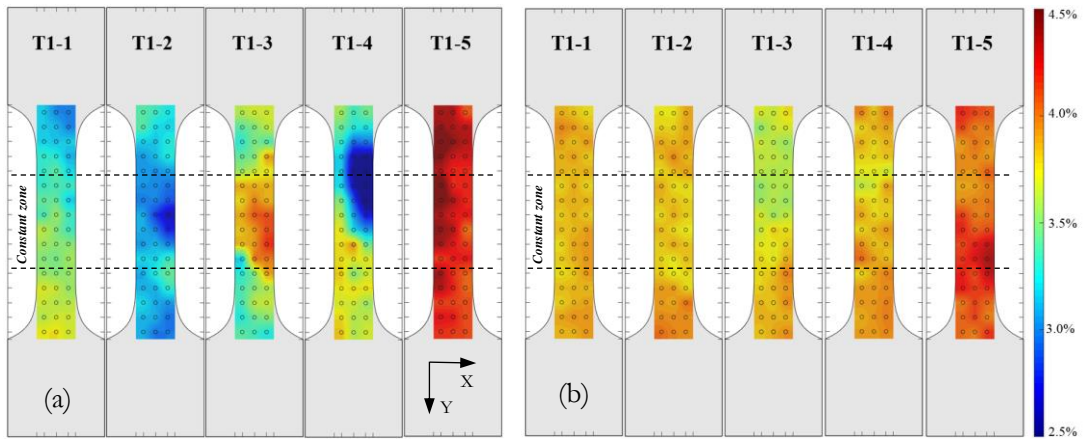
Figure 10 Contour maps for fiber volume fraction V_f: (a) casting surface; (b) sheathed surface.
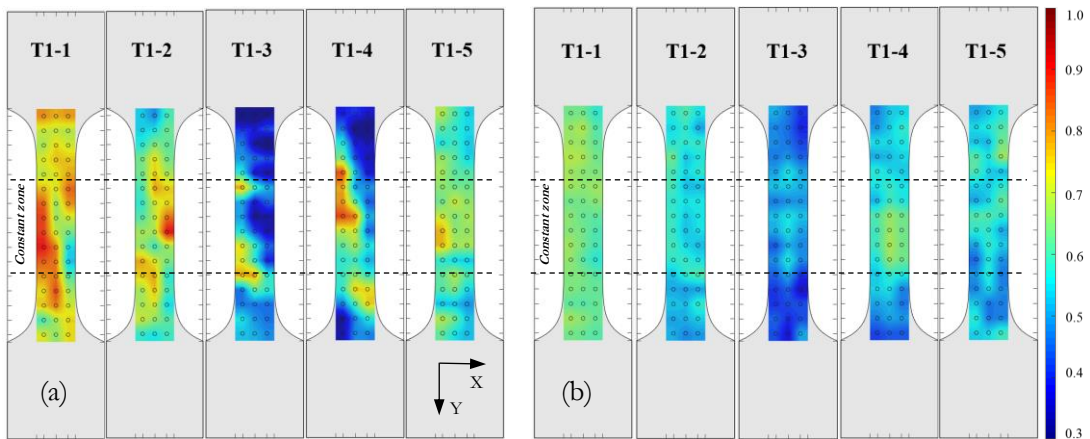
Figure 11 Contour maps for fiber orientation factor μ_0: (a) casting surface; (b) sheathed surface
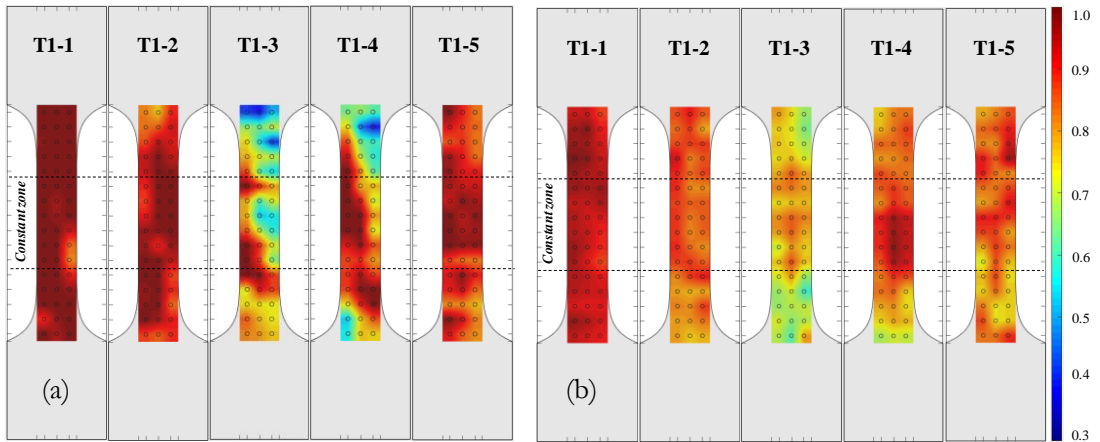
Figure 12 Contour maps for fiber orientation factor μ_1: (a) casting surface; (b) sheathed surface
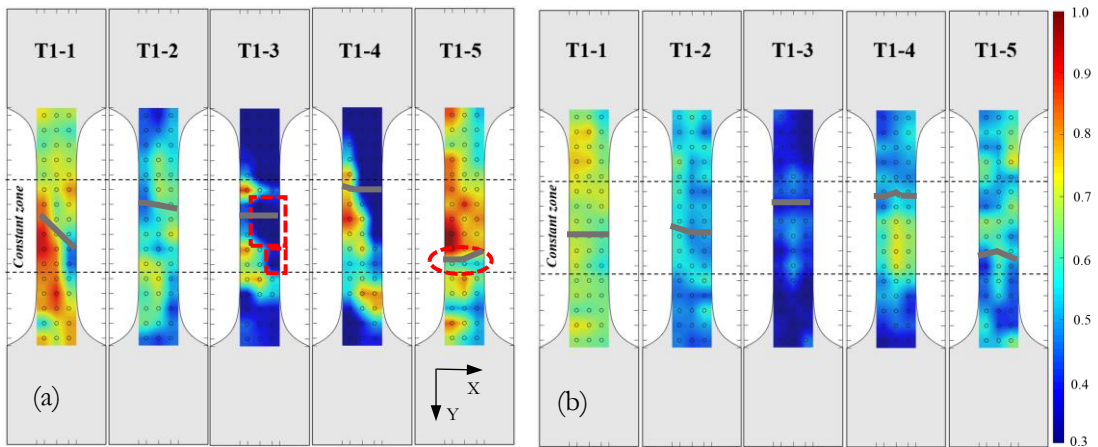
Figure 13 Contour maps of normalized $\lambda = V_f \mu_0 \mu_1$: (a) casting surface; (b) sheathed surface
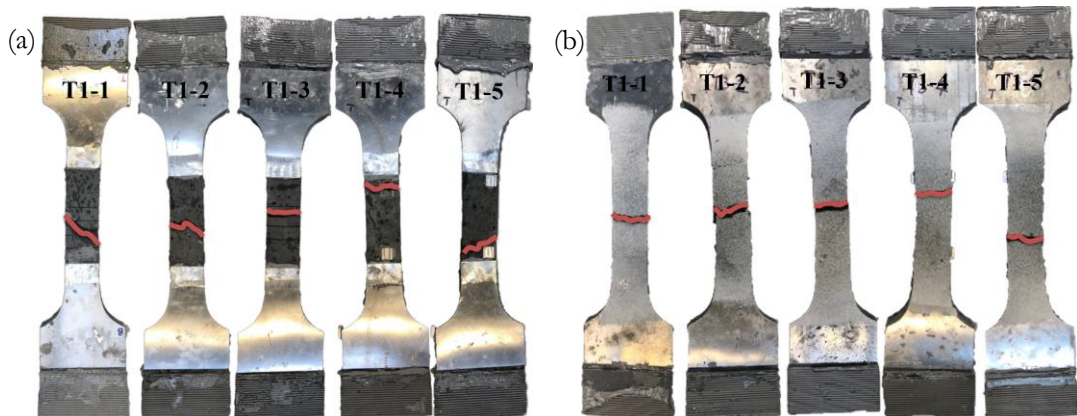
Figure 14 Location of discrete softening cracks of all DTT specimens (marked by red lines):
(a) casting surface; (b) sheathed surface

4.2 DTT results

4.2.1 Location of the discrete softening crack

Figure 14 shows the location of discrete softening cracks leading to specimen fracture for all DTT specimens. These crack locations coincide well with the predictions from NDT results (Figure 13). All discrete cracks occurred in the central constant zone of specimen, and distributed along the flow direction of fresh UHPFRC, as expected. These results validate the design of the DTT specimen shape and testing method, and the test results characterize objectively the tensile performance of UHPFRC.

4.2.2 Stress – strain response

The DTT results are presented in terms of stress vs. strain (ε-σ) curves, in which the thick black line corresponds to the average response (Figure 15). The stress is defined as the measured force divided by the constant cross-section area (50mm × 80mm), while strain is the average value measured from the two short LVDTs divided by the measurement base length.

Table 4 summarizes the main tensile parameters for each specimen, including elastic modulus E_U, elastic limit (stress f_{Ute} and corresponding strain ε_{Ute}, ultimate limit (tensile strength f_{Utu} and hardening strain ε_{Utu}. The elastic modulus E_U is determined by the secant modulus of ε-σ curve from $0.3f_{Ute}$ to $0.6f_{Ute}$, such as to eliminate the initial nonlinear stress carrying effects [51]. The inverse analysis method recommended in SIA 2015 is applied to determine the elastic limit [8,52]: the elastic limit corresponds to the starting point where the first irreversible reduction of the secant modulus of more than 5% occurs. Similarly, the first irreversible reduction of more than 2% of the force is applied to determine the ultimate limit. This method effectively avoids underestimation of the hardening strain, considering the slight fluctuations of stress within a large portion of the strain-hardening domain in this study.

Besides, the maximum pull-out stress τ_f is assumed to be 7MPa following the experimental test results from Wuest [35], who used similar steel fibers and cementitious matrix. Then the fiber orientation factor μ_0 and efficiency factor μ_1 at fracture surface are estimated based on Equation 1, in which the relation between μ_0 and μ_1 based on Figure 3(b) is assumed and the nominal $V_f = 3.8\%$ is applied. These results are also summarized in Table 4.
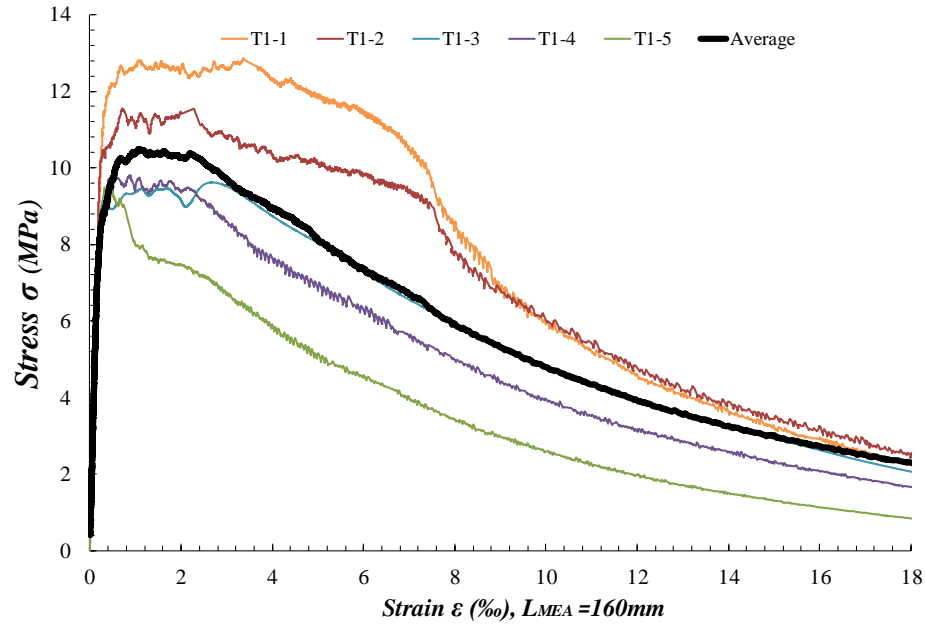
Figure 15 Stress - strain response of 5 specimens

As shown in Figure 15 and Table 4, the DTT results show the range of possible tensile response of UHPFRC as obtained from the thin slab with a thickness of 50mm. All specimens exhibit significant strain-hardening behavior ($f_{Utu}/f_{Ute} \geq 1.15$) with f_{Utu} being in the range of *9.49* to *12.85MPa* and ε_{Utu} being in the range of *0.82‰* to *3.84‰*. This variation of f_{Utu} can be explained mainly by the range of fiber orientation and efficiency (μ_0 and μ_1) as determined for the fracture surface, which depends on the flow distance of fresh UHPFRC mixture from the pouring point. Note that the specimens T1-3 to T1-5 show significant variation of ε_{Utu}, although they have similar values of μ_0 and μ_1. This is related to the variation of local fiber distribution within the specimen (Table 3), and is discussed in the next chapter.

4.2.3 Energy absorption

The strain hardening energy g_{Uf} and fracture energy G_{Uf} of UHPFRC, according to Equations 8 and 9, for each specimen are summarized in Table 4.

Obviously, the strain hardening energy is related to the measured hardening strain: specimens T1-2 to T1-4 have similar value of strain hardening energy, while T1-1 has a very pronounced strain hardening behavior with $g_{Uf,A}$ of 31.81*kJ/m³*. On the contrary, T1-5 has almost no strain hardening and thus $g_{Uf,A}$ is only 1.29*kJ/m³*. Again, it can be stated that strain hardening behavior is directly dependent on local fiber distribution. Already some local unfavorable fiber distribution becomes critical for the whole specimen as the remaining parts of the specimen cannot develop their strain hardening capacity. The DTT is thus discriminating defects in local fiber distribution.

Compared with strain hardening energy g_{Uf}, the variation of fracture energy G_{Uf} (12.40~25.28 kJ/m^2) is smaller. This is reasonable since the fracture process zone leading to final fracture of the specimen is dependent on the fiber distribution over the fracture surface with a variation being smaller than the one of local fiber distribution within UHPFRC specimen, as shown in Table 4.

4.2.4 DIC analysis

4.2.4.1 Matrix discontinuities

Based on DIC analysis using VIC-3D, the whole fracture process of each specimen under testing was captured. Note that initiation and propagation of matrix discontinuities in the strain-hardening domain are invisible to the naked eye and could not be measured using traditional sensors, but are detected on DIC strain maps. On this basis, the DIC strain map at ultimate limit state for each specimen is presented in Table 4, where the lines stand for matrix discontinuities. Accordingly, the number n, average spacing $\overline{S_r} = L_{MEA}/n$ and pattern of matrix discontinuities are detertemined to characterize the strain-hardening response of each specimen. Wide ranges of n and $\overline{S_r}$ values are observed in Table 4.

Besides, the uniformity factor μ_2, serving as a scalar indicator of uniformity degree of local fiber distribution within UHPFRC, is determined for each specimen using Equations 7 and 8. As expected, a wide range of μ_2 (0.11~0.64) is obtained, but each single value is consistent for the corresponding specimen, as shown in Figure 13.

4.2.4.2 Fracture process

Figure 16 shows three graphs of representative fracture processes from specimens T1-1, T1-3 and T1-5, respectively. In each graph, point A' refers to the moment when the first matrix discontinuity is activated based on DIC analysis, point A and B correspond to the elastic limit and ultimate limit (as determined in section 4.2.2), and point C is a random point on the softening branch.

All graphs show that there is only one short matrix discontinuity generated at point A, after which the number of matrix discontunities increases rapidly. It should be mentioned that the initiation of matrix discontinuity (point A') occurs before point A. However, the propagation of matrix discontinuity from point A' to A is insignificant, and therefore the specimen can still be considered as elastic material. This indicates that point A, as determined based on the criteria described in section 4.2.2, is an objective threshold. Point B is characterized by the formation of the fracture process zone with formation of the single localized fictitious crack by grouping of several matrix discontinuities. Afterward, the opening fictitious crack is increasing, while stress is decreasing, until maximum crack opening of $w = l_f/2$. Simultaneously, the parts outside the fracture process zone, including matrix discontinuities, are unloading.
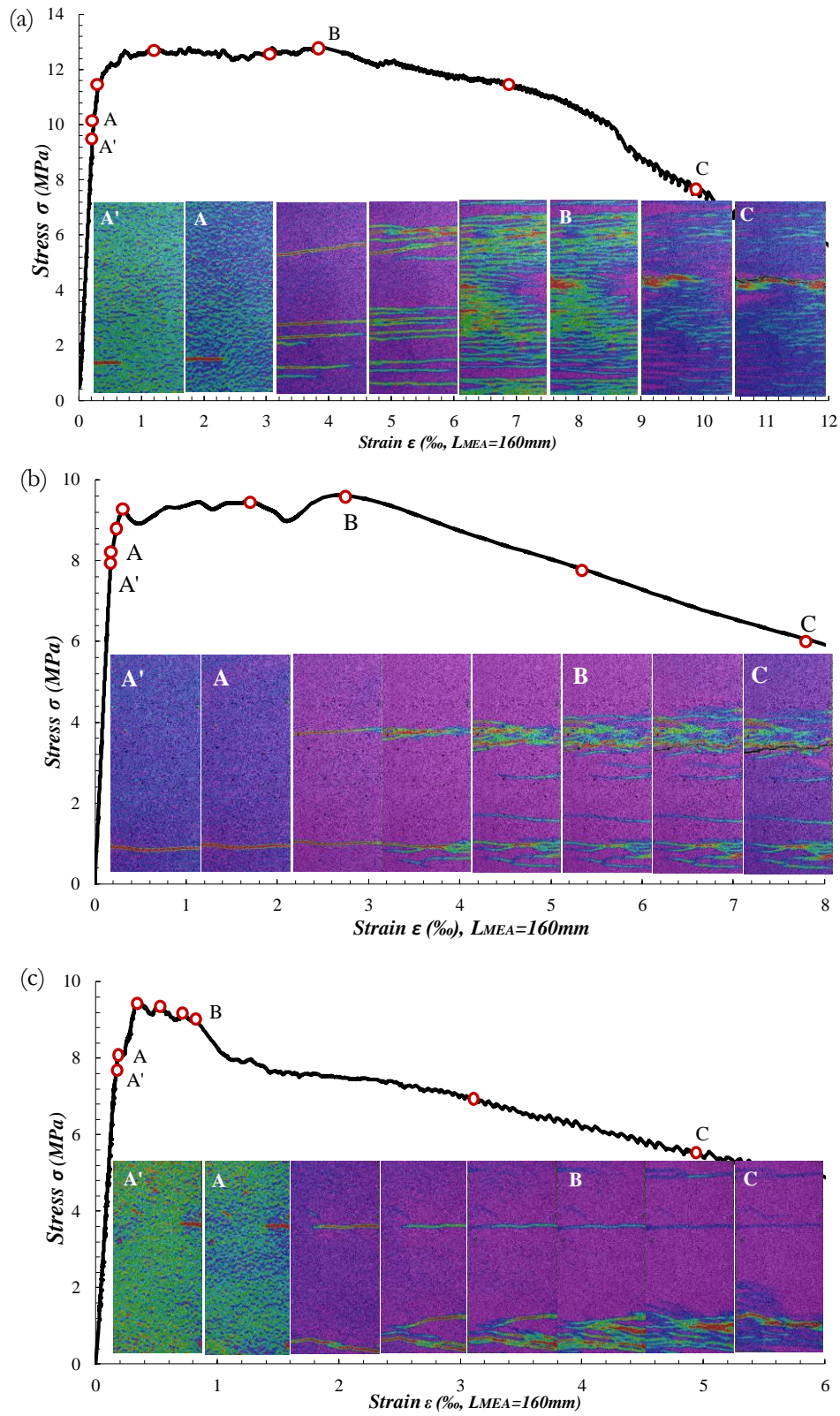
Figure 16 Fracture processes of specimen (a) T1-1, (b) T1-3, (c) T1-5

4.2.4.3 Development of matrix discontinuities and fictitious crack opening

Using the virtual extensometers of the DIC analysis tool, the opening response of every single matrix discontinuity and fictitious crack is recorded over the entire test. The virtual extensometers, with measurement length of about 3mm, are set separately to be aligned to the tensile direction and are located at the center of the specimen width. In order to obtain actual opening values, the contribution from the elastic deformation within the measurement length is deduced. All specimens show similar opening vs. stress *(w-σ)* curves as illustrated in Figure 17 for Specimen T1-1, where the red line represents the fictitious crack and the blue lines refer to the different matrix discontinuities.

Figure 17 shows openings of the matrix discontinuities ranging from 8 to 26μm with an average opening $\overline{w}_i = 13$μm at the ultimate limit. For the other specimens, the determined values of matrix discontinuity opening mainly range from 10 to 30μm, although one single high value of 50μm is recorded for specimen T1-3. The average opening $\overline{w}_i$ for each specimen is in the range of 13 to 21μm, and the average value of all specimens is 15μm (Table 4). This is slightly lower than reported average values $\overline{w}_i = 22$μm for other UHPFRC types with lower fiber volume fraction ($V_f = 2.5$ to $3.0\%, \tau = 12MPa$) in [3] and $\overline{w}_i = 18$μm ($V_f = 3.0\%, \tau = 11MPa$) in [17]. Such difference may be attributed to the assumed low fiber pull-out stress ($\tau = 7MPa$) and high fiber volume fraction ($V_f = 3.8\%,$) in this study. This aspect is not further studied here.

(a)

Stress (MPa) vs *Opening w (mm)*

Fictitious crack

matrix discontinuities
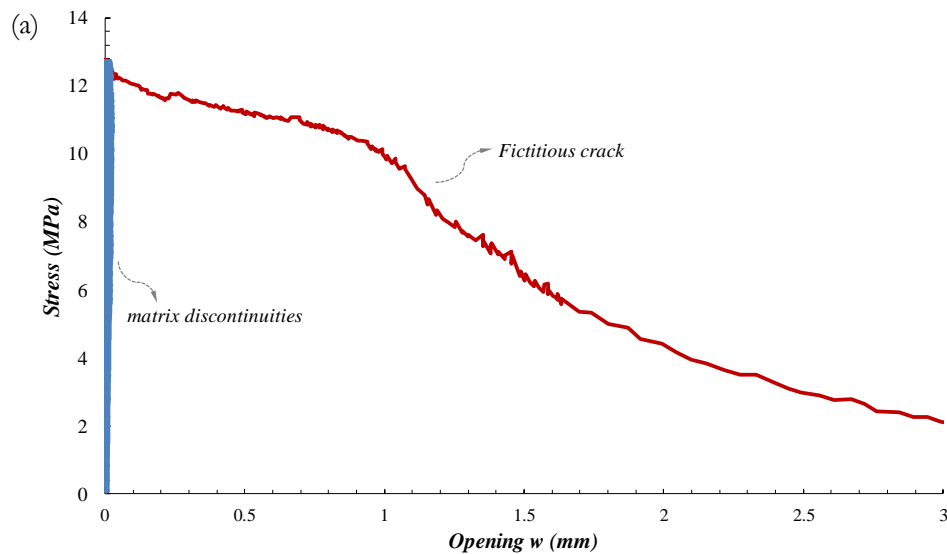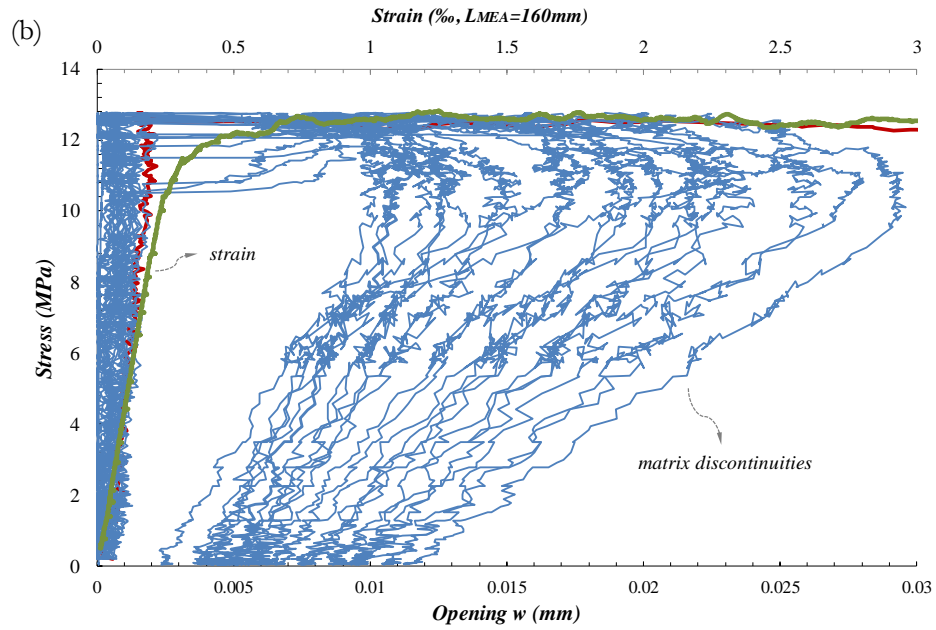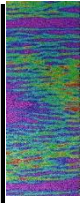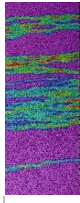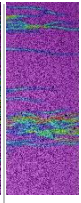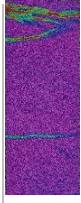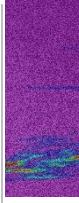
Figure 17 Representative stress – opening curve of UHPFRC specimen T1-1: (a) overview, (b) zoom on opening values up to 0.03mm.

Based on the aforementioned testing results, the considerable variation of local fiber distribution within UHPFRC, as quantitatively characterized by uniformity factor μ_2, is confirmed. Compared with fiber orientation μ_0 and efficiency μ_1, μ_2 has much higher variation in this study, which corresponds well to the wide range of analyzed strain-hardening responses, especially hardening strain ε_{Utu} and matrix discontinuity energy $g_{Uf,A}$

Table 3 Statistical analysis of fiber distribution

Item		T1-1 Casting	T1-1 Sheathed	T1-1 Both	T1-2 Casting	T1-2 Sheathed	T1-2 Both	T1-3 Casting	T1-3 Sheathed	T1-3 Both	T1-4 Casting	T1-4 Sheathed	T1-4 Both	T1-5 Casting	T1-5 Sheathed	T1-5 Both	Slab T1
V_f	$\bar{V}_f$ (%)	3.41	3.86	3.63	3.10	3.85	3.47	3.66	3.72	3.69	3.32	3.86	3.59	4.28	4.08	4.18	3.71
	$\hat{c}_v$	6.3%	1.4%	7.5%	5.3%	2.2%	11.4%	7.5%	3.3%	5.8%	14.3%	2.5%	12.1%	3.6%	3.1%	4.2%	10.7%
μ_0	$\bar{\mu}_0$	0.74	0.74	0.69	0.66	0.55	0.61	0.48	0.47	0.47	0.54	0.55	0.55	0.62	0.54	0.58	0.58
	$\hat{c}_v$	11.6%	3.8%	11.9%	13.6%	6.8%	14.5%	29.6%	11.5%	22.5%	29.8%	11.6%	22.4%	11.1%	9.8%	12.3%	20.6%
μ_1	$\bar{\mu}_1$	0.98	0.94	0.96	0.94	0.85	0.89	0.74	0.75	0.74	0.81	0.84	0.83	0.91	0.83	0.87	0.86
	$\hat{c}_v$	4.1%	3.2%	4.3%	6.7%	5.0%	8.0%	21.7%	9.0%	16.5%	20.4%	8.6%	15.5%	7.3%	7.3%	8.5%	13.8%
λ	λ	0.72	0.67	0.69	0.56	0.52	0.54	0.39	0.38	0.39	0.45	0.52	0.49	0.70	0.53	0.62	0.54
	$\bar{\hat{c}}_v$	15.4%	7.6%	12.9%	17.4%	11.0%	15.2%	48.3%	19.0%	37.0%	50.8%	19.8%	37.1%	19.4%	16.1%	22.8%	31.1%

Table 4 Tensile parameters from DTT

Notation	E_U (GPa)	f_{Ute} (MPa)	f_{Utu} (MPa)	$\dfrac{f_{Utu}}{f_{Ute}}$	ε_{Ute} (‰)	ε_{Utu} (‰)	$\varepsilon_{Utu,cal}$ (‰)	μ_0	$\bar{\mu}_1$	g_{Uf} (kJ/m²)	n	$\bar{s}_r$ (mm)	G_{Uf} (kJ/m²)	w_i (μm)	$\bar{w}_i$ (μm)	$s_{r,c}$ (mm)	μ_2	Matrix discontinuities at f_{Utu}
T1-1	45.6	10.33	12.85	1.24	0.24	3.84	4.03	0.68	0.96	31.81	40	4.00	25.28	10 ~ 26	13	2.54	0.64	
T1-2	49.09	9.82	11.55	1.18	0.22	2.29	2.30	0.62	0.94	15.98	22	7.27	20.58	7 ~ 29	14	2.85	0.39	
T1-3	47.39	8.46	9.62	1.14	0.21	2.67	2.08	0.53	0.92	17.93	20	8.00	15.93	8 ~ 50	21	3.41	0.43	
T1-4	49.64	8.51	9.8	1.15	0.23	2.18	1.88	0.53	0.93	13.1	11	14.55	14.09	7 ~ 36	18	3.37	0.23	
T1-5	48.38	8.14	9.49	1.17	0.19	0.82	0.76	0.52	0.92	1.29	6	26.67	12.40	8 ~ 18	13	3.47	0.13	
Average	48.02	9.05	10.66	1.17	0.22	2.36	2.21	0.58	0.93	16.02	21	10.97	17.66	-	15.8	-	0.39	-
Std. dev.	1.59	0.96	1.48	0.04	0.02	1.08	1.18	0.07	0.02	10.94	12	8.97	5.24	-	3.6	-	0.18	-
$\widehat{c_v}$	0.03	0.11	0.14	0.04	0.09	0.46	0.53	0.12	0.02	0.68	0.6	0.82	0.30	-	0.23	-	0.46	-

[a] The tensile strength of the matrix $f_{Utu} = 7.0\,MPa$.

5. Influence of local fiber distribution on tensile behavior of UHPFRC

Similarly, the local fiber distribution is characterized by the local fiber volume fraction, local orientation factor and efficiency factor in this study. And the uniformity factor serves as a scalar indicator of uniformity degree of local fiber distribution. The influence of uniformity factor on strain hardening response of UHPFRC is highlighted and analyzed in this chapter.

5.1 Matrix discontinuities

As shown in Table 4 and Figure 16, characteristics of matrix discontinuities observed on specimens differ from each other. This phenomenon is explained by the degree of uniformity of local fiber distribution within UHPFRC (as described in section 4.1).

Specimen T1-1 (Figure 16-a) with relatively uniform distribution of preferential alignment of fibers in the tension direction as evidenced by $\mu_2 = 0.64$, large amount of matrix discontinuities appear in the strain-hardening domain (A-B). Due to important deformation redistribution along the specimen, the matrix discontinuities pattern changes continuously with increasing force: many matrix discontinuities appear in groups, accompanied by multiple branches. Some of them initiate separately from one edge, cross each other or merge when propagating toward the other edge. When reaching the ultimate limit (B), the matrix discontinuities are distributed uniformly over the specimen length with small spacings ($\bar{s}_r = 4mm$). Smeared matrix discontinuities may be assumed, and therefore the specimen is still considered to behave as a homogeneous material. Consequently, high hardening strain and hardening energy values ($\varepsilon_{Utu} = 3.84‰$, $g_{Uf} = 31.81\ kJ/m^3$) are obtained.

In specimen T1-3 (Figure 16-b), two large clusters of matrix discontinuities occur along the specimen length, and between them, there are several matrix discontinuities with relatively large spacing ($> l_f$) distributed ramdonly ($\mu_2 = 0.43$). In this case, several local weak zones, which do not extend through the whole specimen width, are found based on NDT analysis. Matrix discontinuities initiate and propagate mainly in these areas, although slight stress distribution is observed. As a consequence, several clusters of matrix discontinuities form in specific zones in the strain-hardening domain.

Regarding specimen T1-5 (Figure 15-c), the obvious weak zone crossing the section width ($\mu_2 = 0.13$) results in concentration of matrix discontinuities. Subsequently, localized fictitious crack is formed with extremely low hardening strain and matrix discontinuity energy ($\varepsilon_{Utu} = 0.82‰$, $g_{Uf} = 1.29\ kJ/m^3$).

It can be stated that the local fiber distribution within the specimen has an important influence on the strain-hardening behavior of UHPFRC in tension. It is obvious that higher degree of uniformity of local fiber distribution results in more pronounced matrix discontinuities, and subsequent higher hardening strain and matrix discontinuities energy at ultimate limit. On the contrary, the matrix discontinuities concentrate largely in the local weak zones, leading to one or several clusters of matrix discontinuities at ultimate limit.

5.2 Analytical model and comparison with data from literature

According to equation 8, the average spacing of matrix discontinuities $\overline{S_r}$ is proportional to $1/(\mu_0\mu_1\mu_2)$ for a given UHPFRC mix. The hardening strain ε_{Utu}, hence, can be assumed to vary linearly with $\mu_0\mu_1\mu_2$ considering an average opening of matrix discontinuity $\overline{w}_i$. In order to verify this assumption, experimental results from a previous study [53] and other researchers [3,17,28,35] using different UHPFRC mixes are reviewed, and the corresponding uniformity factors are calculated, as summarized in Table 5. Based on a statistical regression analysis, a regression line is determined for the relation between ε_{Utu} and $\mu_0\mu_1\mu_2\tau V_f/(d_f f_{mt})$ for different UHPFRC mixes. The relatively high correlation coefficients R² confirm the linear relation between ε_{Utu} and $\mu_0\mu_1\mu_2$ for a given UHPFRC mix (Figure 18a). Similarly, a linear relation is also found between g_{Uf} and $\mu_0\mu_1\mu_2$ (Figure 18b).
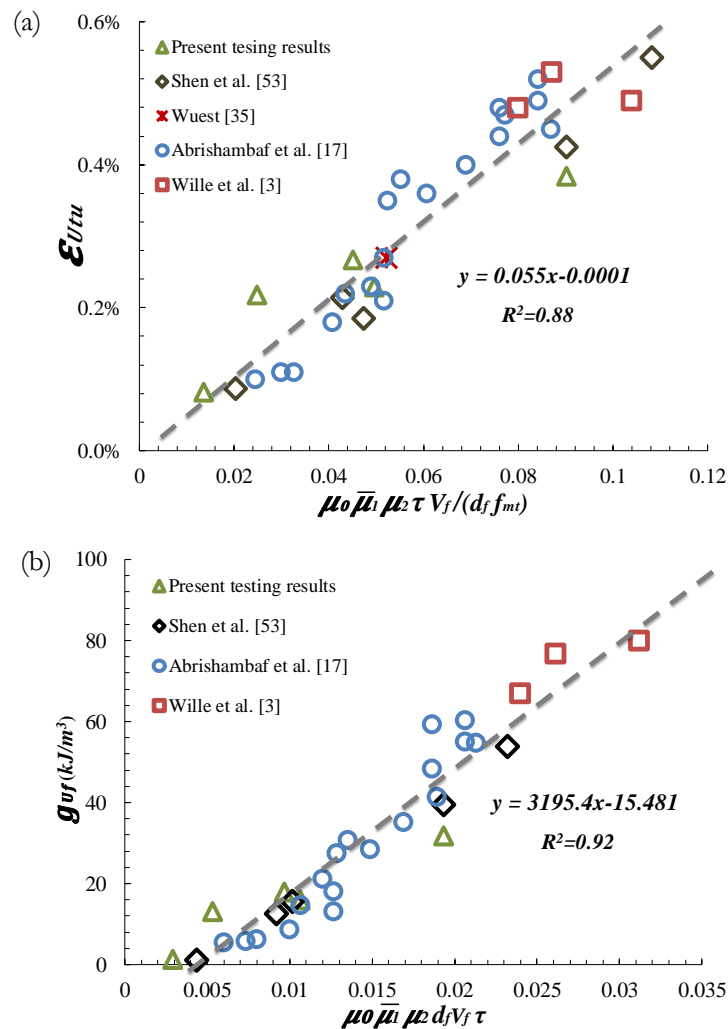
Figure 18 Relation between local fiber distribution and (a) hardening strain ε_{Utu}; and (b) matrix discontinuity energy g_{Uf}

Following the fictitious crack model by Hillerborg [1,35], the total elongation δ_{Utu} of UHPFRC at tensile strength is related to the opening w_i of each matrix discontinuity and the elastic deformation of the remaining part. Thus, the hardening strain ε_{Utu} can be calculated using Equation 15:

$$\varepsilon_{Utu} = \frac{\delta_{Utu}}{L_{MEA}} = \frac{\sum_{i=0}^{n} w_i(f_{Utu})}{L_{MEA}} + \frac{f_{Utu}}{E_U} \tag{15}$$

By assuming an average matrix discontinuity opening $\overline{w}_i$ for a given UHPFRC mix, Equation 15 is transformed to:

$$\varepsilon_{Utu} = \frac{n \cdot \overline{w}_i(f_{Utu})}{L_{MEA}} + \frac{f_{Utu}}{E_U} = \mu_2 \frac{\overline{w}_i(f_{Utu})}{S_{r,c}} + \frac{f_{Utu}}{E_U} \tag{16}$$

The comparison between the measured ε_{Utu} and calculated $\varepsilon_{Utu,cal}$ using Equation 16 is illustrated in Figure 19, where a good agreement with R^2=0.93 is observed.
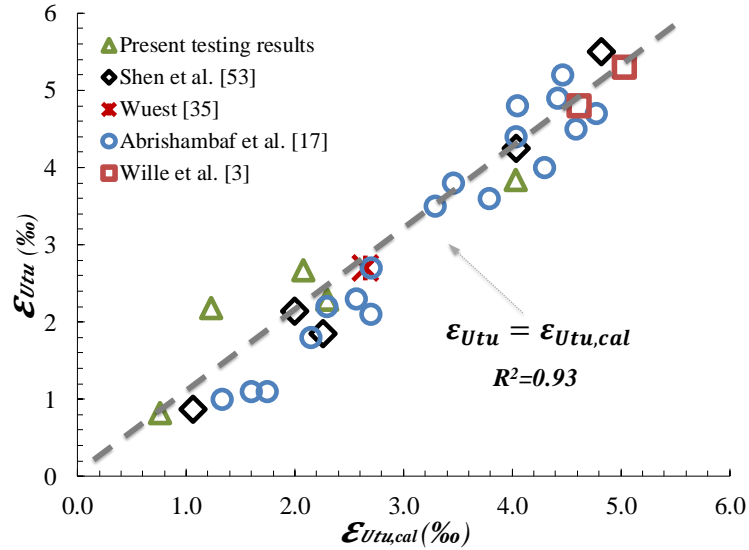
Figure 19 Comparison between hardening strain as obtained analytically ε_{Utu} and experimentally $\varepsilon_{Utu,exp}$

The results by [3,17] in Table 5 indicate that, slender and thin specimens cast in layers using individual molds lead to high fiber uniformity factors μ_2 with small variation. Thus, these specimens with preferential fiber orientation in the loading direction obviously result in a significant strain hardening response, even for low $V_f \frac{l_f}{d_f}$ value.

However, the specimens cut from plates, which are representative of structural applications, exhibit a wide range of μ_2. Even some poor strain-hardening response with limited hardening strain was observed for some of them. In this case, the uniformity factor should be considered to adjust accordingly the measured values to link the actual local fiber distribution in view of intended applications.

As proposed in [9,10,51], the representative tensile response should correspond to the average local fiber distribution within the considered structural UHPFRC element as shown in the next chapter.

6. Application to a UHPFRC layer

In the following, the average fiber orientation factor $\mu_0 = 0.58$, efficiency factor $\mu_1 = 0.95$, and uniformity factor $\mu_2 = 0.39$ determined from the present experimental campaign are used for the 50mm UHPFRC layer using a different mix in [10]. The calculated hardening strain $\varepsilon_{Utu,cal} = 1.68‰$, calculated according to Equation 15, is close to that of testing result ($\varepsilon_{Utu} = 1.71‰$), as given in Table 6.

Table 6 Prediction of hardening strain considering local fiber distribution within the UHPFRC layer

Ref.	V_f (%)	l_f/d_f	h_U (mm)	E_U (GPa)	τ (MPa)	f_{Utu} (MPa)	$s_{r,c}$ (mm)	$\overline{w}_i$ (µm)	μ_0	μ_1	μ_2	ε_{Utu} (‰)	$\varepsilon_{Utu,cal}$ (‰)
Present	3.8	13/0.175	50	48.2	7	10.7	4.26		0.58	0.95	0.39	2.36	2.16
[10]	3.0	13/0.16	50	40.3	6.7	8.0	5.56	15	0.58	0.95	0.39	1.71	1.68
			25	40.3	6.7	9.5	3.74		0.6	0.96	0.58	2.59	2.54
[9]	3.0	13/0.16	40	40.3	6.7	9.8	4.17		0.57	0.95	0.52	2.25	2.19

This suggests that the average μ_2 within UHPFRC is thickness dependent, similar with μ_0 and μ_1 as proposed in [10]. Thus the average μ_2 for UHPFRC layers with thickness of 25mm and 40mm are determined to be 0.58 and 0.52, considering μ_0 and μ_1 from the corresponding testing results in [10] and [9], respectively. The results are also summarized in Table 6 and validate the proposed analytical model using the uniformity factor.

Table 5 Review of tensile parameters of UHPFRC from other studies

Ref.	V_f (%)	l_f (mm)	d_f (mm)	τ (MPa)	f_{mt} (MPa)	L_{MEA} (mm)	f_{Utu} (MPa)	ε_{Utu} (‰)	$\varepsilon_{Utu,exp}$ (‰)	μ_0	$\overline{\mu_1}$ [a]	g_{Uf} (kJ/m³)	G_{Uf} (kJ/m)	n	$\overline{w}_i$ [a] (μm)	$\overline{s}_r$ (mm)	$s_{r,c}$ (mm)	μ_2
Shen et al.[53]	3.8	13	0.175	7.0	7.0	160	14.33	4.25	4.0	0.74	0.98	39.53	16.01	40	15	4.00	2.30	0.57
							10.59	0.87	1.1	0.57	0.94	1.14	13.85	9		17.78	3.10	0.17
							10.21	2.14	2.0	0.55	0.93	12.6	16.01	19		8.42	3.23	0.38
							13.98	1.85	2.3	0.73	0.97	15.63	21.66	21		7.62	2.34	0.31
							15.50	5.50	4.8	0.78	0.99	53.86	21.48	48		3.33	2.15	0.64
Wuest [35]	4.0	13	0.20	6.5	7.0	350	13.50	2.70	2.65	0.66	0.97	-	-	45	16	6.90	2.60	0.35
	3.0	9 12	0.175	11.1	8.0	134	14.46	4.50	4.59	0.73	0.97	54.81	17.24	32		4.19	2.16	0.52
							13.72	4.40	4.04	0.73	0.97	48.42	18.27	28		4.79	2.16	0.45
							12.74	4.90	4.42	0.66	0.96	55.10	15.48	31		4.32	2.42	0.56
							15.02	5.20	4.46	0.73	0.97	60.39	18.49	31		4.32	2.14	0.50
							14.32	4.80	4.05	0.71	0.97	59.34	16.96	28		4.79	2.23	0.47
							7.48	2.70	2.70	0.47	0.91	18.12	7.27	19	18	7.05	3.59	0.51
							7.32	2.10	2.70	0.51	0.92	13.17	6.14	19		7.05	3.28	0.46
							7.37	2.30	2.57	0.47	0.91	21.22	7.68	18		7.44	3.60	0.48
Abrishambaf et al. [17]	1.5	9 12	0.175	11.1	8.0	134	7.24	2.20	2.29	0.46	0.90	14.74	5.85	16		8.38	3.69	0.44
							6.09	1.00	1.333	0.46	0.90	5.51	7.18	9	22	14.89	3.70	0.25
							6.71	1.10	1.75	0.45	0.90	6.32	5.44	12		11.17	3.78	0.34
							6.64	1.80	2.15	0.46	0.90	8.71	6.51	15		8.93	3.73	0.42
							6.08	1.10	1.60	0.44	0.89	5.86	5.24	11		12.18	3.91	0.32
							8.82	4.70	4.77	0.90	0.99	41.42	10.47	28		4.79	3.46	0.72
							9.65	4.00	4.30	0.87	0.99	35.23	11.57	25		5.36	3.57	0.67
							8.55	3.50	3.29	0.79	0.99	27.55	9.26	19		7.05	3.95	0.56
							8.86	3.60	3.79	0.84	0.99	28.53	10.36	22		6.09	3.69	0.61
							8.76	3.80	3.46	0.82	0.99	30.81	9.75	20		6.70	3.79	0.57
Wille et al. [3]	2.0	13	0.2	12.0	7.5	76	15.00	4.80	4.62	0.96	1.00	67.00	22.92	17	23	4.60	2.39	0.52
	2.5						16.50	5.30	5.03	0.85	1.00	76.80	26.83	18		4.20	2.15	0.51
	3.0						17.80	4.90	5.02	0.76	0.99	80.00	28.88	24		3.50	2.03	0.58

[a] The fiber efficiency factor μ_1 is determined based on Figure 3(b).

7. Conclusions

This paper introduces the uniformity factor μ_2 for considering the degree of uniformity of local fiber distribution within UHPFRC elements. Accompanied with the fiber orientation and efficiency factors μ_0 and μ_1, the significant influence of μ_2 on the strain-hardening response of UHPFRC under uniaxial tension is investigated quantitatively. The main conclusions are:

(1) Important variation of local fiber distribution, including fiber volume fraction V_f, orientation μ_0 and efficiency μ_1, is observed within a UHPFRC slab element based on NDT analysis. Among the relevant parameters, fiber orientation factor μ_0 shows the largest variation ($11.9\% \leq \hat{c}_v \leq 22.5\%$).

(2) The uniformity factor μ_2 as determined by the spacing of matrix discontinuities, is proposed to characterize quantitatively local fiber distribution within a UHPFRC element. It is observed that high μ_2-value is the result of more pronounced formation of matrix discontinuities, leading to higher hardening strain ε_{Utu} and matrix discontinuities energy g_{Uf} values at ultimate limit.

(3) Compared with the μ_0 and μ_1 factors, the uniformity factor μ_2 exhibits a wider range (0.13 to 0.64) within the tested UHPFC slab and has a stronger influence on the strain-hardening response of UHPFRC. Based on present testing results and compared to results in the literature, ε_{Utu} and g_{Uf} vary linearly with $\mu_0\mu_1\mu_2$ for a given UHPFRC mix.

(4) For a given structural element, average values of μ_2, μ_0 and μ_1 factors should be used to determine the representative tensile response of UHPFRC for the intended application.

(5) For a given UHPFRC layer, the uniformity factor μ_2 is thickness dependent: for UHPFRC layers with thickness of 25mm, 40mm and 50mm, the determined μ_2-factors are 0.58, 0.52 and 0.39, respectively.

(6) The NDT method using the magnetic probe allows fine and reliable contour mapping of the actual fiber distribution in UHPFRC element. It is shown to be an efficient method to determine local fiber distribution in a UHPFRC element, thus eventually replacing fracture testing.

8. References

[1] A. Hillerborg, Analysis of one single crack, Fracture Mechanics of Concrete (Developments in Civil Engineering). (1983) 223–249.

[2] E. Brühwiler, "Structural UHPFRC" to enhance bridges, in: Keynote Lecture, 2nd International Conference on UHPC Materials and Structures (UHPC 2018 - China), Fuzhou, China, 2018: pp. 140–158.

[3] K. Wille, S. El-Tawil, A.E. Naaman, Properties of strain hardening ultra high performance fiber reinforced concrete (UHP-FRC) under direct tensile loading, Cement and Concrete Composites. 48 (2014) 53–66.

[4] E. Denarié, E. Brühwiler, Cast-on site UHPFRC for improvement of existing structures–achievements over the last 10 years in practice and research, in: 7th Workshop on High Performance Fiber Reinforced Cement Composites, 1-3, June 2015, Stuttgart, Germany, 2015.

[5] M. Bastien-Masse, E. Brühwiler, Experimental investigation on punching resistance of R-UHPFRC–RC composite slabs, Materials and Structures. 49 (2016) 1573–1590.

[6] K. Habel, Structural behaviour of elements combining ultra-high performance fibre reinforced concretes (UHPFRC) and reinforced concrete, Doctoral Thesis (EPFL). (2004).

[7] J.-P. Charron, E. Denarié, E. Brühwiler, Permeability of ultra high performance fiber reinforced concretes (UHPFRC) under high stresses, Mater Struct. 40 (2007) 269–277.

[8] SIA 2052, Technical Leaflet SIA 2052 UHPFRC – Materials, design and construction, 2016.

[9] C. Oesterlee, Structural response of reinforced UHPFRC and RC composite members (doctoral thesis, 4848), École polytechnique fédérale de Lausanne (EPFL), 2010.

[10] M. Bastien-Masse, E. Denarié, E. Brühwiler, Effect of fiber orientation on the in-plane tensile response of UHPFRC reinforcement layers, Cement and Concrete Composites. 67 (2016) 111–125.

[11] L.F.M. Duque, B. Graybeal, Fiber orientation distribution and tensile mechanical response in UHPFRC, Mater Struct. 50 (2017) 1–17.

[12] B. Zhou, Y. Uchida, Influence of flowability, casting time and formwork geometry on fiber orientation and mechanical properties of UHPFRC, Cement and Concrete Research. 95 (2017) 164–177.

[13] B. Zhou, Y. Uchida, Relationship between fiber orientation/distribution and post-cracking behaviour in ultra-high-performance fiber-reinforced concrete (UHPFRC), Cement and Concrete Composites. 83 (2017) 66–75.

[14] D.-Y. Yoo, N. Banthia, Mechanical properties of ultra-high-performance fiber-reinforced concrete: A review, Cement and Concrete Composites. 73 (2016) 267–280.

[15] E. Denarié, L. Sofia, E. Brühwiler, Characterization of the tensile response of strain hardening UHPFRC - Chillon Viaducts, AFGC-ACI-Fib-RILEM Int. Symposium on Ultra-High Performance Fibre-Reinforced Concrete, UHPFRC 2017. (2017).

[16] D.-Y. Yoo, S.-T. Kang, J.-H. Lee, Y.-S. Yoon, Effect of shrinkage reducing admixture on tensile and flexural behaviors of UHPFRC considering fiber distribution characteristics, Cement and Concrete Research. 54 (2013) 180–190.

[17] A. Abrishambaf, M. Pimentel, S. Nunes, Influence of fibre orientation on the tensile behaviour of ultra-high performance fibre reinforced cementitious composites, Cement and Concrete Research. 97 (2017) 28–40.

[18] S. Nunes, M. Pimentel, F. Ribeiro, P. Milheiro-Oliveira, A. Carvalho, Estimation of the tensile strength of UHPFRC layers based on non-destructive assessment of the fibre content and orientation, Cement and Concrete Composites. 83 (2017) 222–238.

[19] S. Nunes, M. Pimentel, A. Carvalho, Non-destructive assessment of fibre content and orientation in UHPFRC layers based on a magnetic method, Cement and Concrete Composites. 72 (2016) 66–79.

[20] Voo Yen Lei, Foster Stephen J., Voo Chen Cheong, Ultrahigh-Performance Concrete Segmental Bridge Technology: Toward Sustainable Bridge Construction, Journal of Bridge Engineering. 20 (2015) B5014001.

[21] N. AFNOR, P18-710: National addition to Eurocode 2–Design of concrete structures: Specific rules for ultra-high performance fiber-reinforced concrete (UHPFRC), Association Française de Normalisation, 2016.

[22] O. Bayard, O. Ple, G. Bernier, Internal Heterogeneity in a Reactive Powder Concrete, in: 6th RILEM Symposium on Fibre-Reinforced Concretes, Varenna-Lecco, Italy, 2004: pp. 20–22.

[23] O. Bayard, Approche multi-échelles du comportement mécanique des bétons à ultra hautes performances renforcés par des fibres courtes, PhD Thesis, Cachan, Ecole normale supérieure, 2003.

[24] M. di Prisco, P. Martinelli, A numerical approach for the evaluation of the structural redistribution coefficient KRd, Computational Modelling of Concrete Structures-Proc. of EURO-C. 1 (2014) 503–512.

[25] M. Pimentel, S. Nunes, Determination of the fibre content and orientation in UHPFRC layers using NDT–application to the simulation of the behaviour of strengthened beams, in: Maintenance, Monitoring, Safety, Risk and Resilience of Bridges and Bridge Networks, Brazil, 2016: p. 214.

[26] P. Hadl, J. Gröger, N.V. Tue, Experimentelle Untersuchungen zur Streuung im Zugtragverhalten von Stahlfaserbeton, Bautechnik. 92 (2015) 385–393.

[27] P. Hadl, H. Kim, N.V. Tue, Experimental investigations on the scattering in the post cracking tensile behaviour of UHPFRC, in: Proceedings of the Internatinal Symposium on Ultra-High Performance Concrete and High Performance Materials (HiperMat 2016), Kassel, 2016.

[28] M. Xu, K. Wille, Fracture energy of UHP-FRC under direct tensile loading applied at low strain rates, Composites Part B: Engineering. 80 (2015) 116–125.

[29] A.E. Naaman, A statistical theory of strength for fiber reinforced concrete, PhD Thesis, Massachusetts Institute of Technology, 1972.

[30] P.J. Hannant, Fiber Cements and FIber Conretes, England: Wiley & Sons. (1978) 231.

[31] J. Aveston, A. Kelly, Theory of multiple fracture of fibrous composites, J Mater Sci. 8 (1973) 352–362.

[32] D. Dupont, L. Vandewalle, Distribution of steel fibres in rectangular sections, Cement and Concrete Composites. 27 (2005) 391–398.

[33] M. Maage, Interaction between steel fibers and cement based matrixes, Mat. Constr. 10 (1977) 297–301.

[34] J. Wuest, E. Denarié, E. Brühwiler, L. Tamarit, M. Kocher, E. Gallucci, Tomography Analysis of Fiber Distribution and Orientation in Ultra High–Performance Fiber-Reinforced Composites with High-Fiber Dosages, Experimental Techniques. 33 (2009) 50–55.

[35] W. John, Comportement structural des bétons de fibres ultra performants en traction dans des éléments composés, Doctoral thesis No.3987, EPFL, 2007.

[36] A. Abrishambaf, M. Pimentel, S. Nunes, A meso-mechanical model to simulate the tensile behaviour of ultra-high performance fibre-reinforced cementitious composites, Composite Structures. 222 (2019) 110911.

[37] N. Ozyurt, L.Y. Woo, T.O. Mason, S.P. Shah, Monitoring Fiber Dispersion in Fiber-Reinforced Cementitious Materials: Comparison of AC-Impedance Spectroscopy and Image Analysis, ACI Materials Journal; Farmington Hills. 103 (2006) 340–347.

[38] L. Ferrara, M. Faifer, S. Toscani, A magnetic method for non destructive monitoring of fiber dispersion and orientation in steel fiber reinforced cementitious composites—part 1: method calibration, Mater Struct. 45 (2012) 575–589.

[39] M. Faifer, L. Ferrara, R. Ottoboni, S. Toscani, Low frequency electrical and magnetic methods for non-destructive analysis of fiber dispersion in fiber reinforced cementitious composites: an overview, Sensors. 13 (2013) 1300–1318.

[40] S.J. Barnett, J.-F. Lataste, T. Parry, S.G. Millard, M.N. Soutsos, Assessment of fibre orientation in ultra high performance fibre reinforced concrete and its effect on flexural strength, Mater Struct. 43 (2009) 1009–1023.

[41] Ferrara Liberato, Park Yon-Dong, Shah Surendra P., Correlation among Fresh State Behavior, Fiber Dispersion, and Toughness Properties of SFRCs, Journal of Materials in Civil Engineering. 20 (2008) 493–501.

[42] S. Nunes, M. Pimentel, Characterization and comparison of two magnetic probes (Technical report), Faculdade de Engenharia Universidade do Porto, 2016.

[43] J. Aveston, Single and Multiple Fracture, The Properties of Fiber Composites. (1972) 15–26.

[44] A.P. Fantilli, H. Mihashi, P. Vallini, Multiple cracking and strain hardening in fiber-reinforced concrete under uniaxial tension, Cement and Concrete Research. 39 (2009) 1217–1229.

[45] A. Hillerborg, The theoretical basis of a method to determine the fracture energyGFof concrete, Materials and Structures. 18 (1985) 291–296.

[46] K. Wille, A.E. Naaman, Fracture energy of UHPFRC under direct tensile loading, in: FraMCoS-7 International Conference, Jeju, Korea, 2010.

[47] K. Habel, M. Viviani, E. Denarié, E. Brühwiler, Development of the mechanical properties of an Ultra-High Performance Fiber Reinforced Concrete (UHPFRC), Cement and Concrete Research. 36 (2006) 1362–1370.

[48] H. Neuber, Der zugbeanspruchte Flachstab mit optimalem Querschnittsübergang, Forschung Im Ingenieurwesen. 35 (1969) 29–30.

[49] A. Helbling, E. Brühwiler, Eine neue Halterung für Zugversuche mit Beton-Probekörper (in German), Material Und Technik. 4 (1987) 103–107.

[50] B.A. Graybeal, F. Baby, Development of Direct Tension Test Method for Ultra-High-Performance Fiber-Reinforced Concrete., ACI Materials Journal. 110 (2013) 177–186.

[51] T. Makita, E. Brühwiler, Tensile fatigue behaviour of ultra-high performance fibre reinforced concrete (UHPFRC), Mater Struct. 47 (2014) 475–491.

[52] M.A. Hafiz, Tensile response of Strain-Hardening Ultra High Performance Fiber Reinforced Concretes under low loading rates and low temperatures, Doctoral thesis No.7336, École polytechnique fédérale de Lausanne (EPFL), 2019.

[53] Xiujiang Shen, E. Brühwiler, Tensile Behavior of UHPFRC under Uniaxial and Biaxial Stress Conditions, Journal of Asian Concrete Federation. 4.2 (2018) 67–78.

Paper II

Biaxial Flexural Behavior of Strain-Hardening UHPFRC Thin Slab Elements

ABSTRACT

The biaxial flexural response of strain-hardening UHPFRC circular slab element is investigated experimentally and analytically using the ring-on-ring test. The Digital Image Correlation (DIC) technology is applied to capture the 3D full-field of strain and deflection of the tensile surface through the whole loading process. Based on DIC analysis, a quasi-elastic limit is determined additionally to characterize the flexural response of UHPFRC under biaxial stress condition. The random and uniform distribution of matrix discontinuities in UHPFRC in the quasi-elastic domain, as well as multiple fictitious crack formation in hardening domain, is highlighted. In addition, ring-on-ring test and Four-Point Bending Test (4PBT) results are compared with special emphasis on flexural strength and characteristics of matrix discontinuity development. The results show higher ultimate flexural strength and energy absorption capacity at ultimate limit from the ring-on-ring test, and almost same flexural strength at the quasi-elastic limit for both tests. Finally, a simplified inverse analysis is proposed for the ring-on-ring test based on the elastic slab bending and yield line theories. The calculation results indicate a 19% lower tensile elastic limit stress of the UHPFRC, while an almost equivalent value of tensile strength is obtained from the ring-on-ring test, compared with the 4PBT results.

1. Introduction

Tensile strain-hardening Ultra High Performance Fibre Reinforced Cementitious Composite (UHPFRC) materials show relatively high tensile strength (≥ 10MPa) and ductility [1]. A notable feature of UHPFRC under uniaxial tension is the strain-hardening response with non-visible multiple fine micro-cracks, hereafter called matrix discontinuities, in the bulk matrix before reaching the tensile strength [2]. Afterward, damage concentrates in the fracture process zone characterized by the formation and propagation of a single discrete crack (macrocrack), hereafter called fictitious crack following the classical definition by Hillerborg [3] (Figure 1).
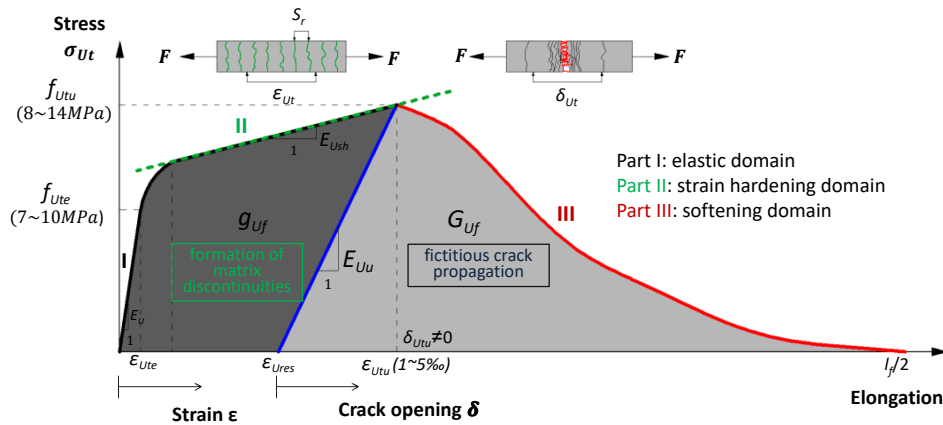
Figure 1 Schematic representation of tensile response of strain-hardening UHPFRC (not in scale)

UHPFRC is used in slab-like applications with relatively thin thickness typically of 50mm subjected to biaxial stresses. Typical structural applications include cast-in place UHPFRC layer for strengthening of reinforced concrete slabs [1,4], slabs of new bridges and buildings as well as shells [5,6]. Such structural UHPFRC systems are subjected to biaxial stresses [7], exhibiting important stress redistribution capacity with high fracture energy dissipation. Consequently, a test method is required to characterize accurately the biaxial stress state in slab-like UHPFRC elements representing actual structural conditions.

UHPFRC standards like SIA 2052 [8] and NF P18-710 [9] recommend uniaxial test methods, either direct tensile test (DTT) or four-point bending test (4PBT), using standardized specimens for material characterization or specimens cut from plates for suitability tests to determine the tensile response of UHPFRC. These specimens are in the uniaxial tensile loading condition and do not represent thin UHPFRC elements subjected to biaxial tensile stress.

As reported by Kim et al. [7], the ultimate flexural strength and energy absorption capacity of UHPFRC are stress state dependent, where considerably higher values have been found under biaxial stress condition. Unlike specimens for uniaxial testing typically showing one fracture plane, complex cracking pattern with large crack surfaces and fracture energy dissipation is observed in UHPFRC elements subjected to biaxial stresses [6,7,10–12]. This reveals significant stress redistribution capacity resulting from fiber bridging effect in various directions.

Furthermore, uniaxial testing results, in particular from extracted specimens, exhibit large scatter due to variation of fiber distribution within the UHPFRC specimen [2,13–16]. Besides, the intrinsic heterogeneity of local fiber distribution would penalize considerably the tensile response of UHPFRC when small-scale specimen is applied [17,18]. Fortunately, this unfavorable influence can be considerably compensated when large cracking surfaces are involved in the fracture process due to stress redistribution during testing, which is well documented for fiber reinforced concrete (FRC) [18–25]. Consequently, a structural redistribution factor was introduced in the *fib* Model Code 2010 for structural FRC application [26,27].

To the best of the authors' knowledge, UHPFRC tensile properties have not yet been characterized under biaxial stresses. Unfavorable misinterpretation of the tensile properties of UHPFRC for structural applications is likely to occur, since the scatter and characteristic values from the uniaxial tests are not representative of UHPFRC slab-like elements.

Regarding biaxial flexural test, the centrally loaded circular slab element test with three support points at 120°, has been widely used to characterize FRC properties [7,12,21,24,25,28–30]. This methodology with circular slab element having a diameter of 800mm and a thickness of 75mm is standardized by ASTM C.1550 for measurement of flexural toughness of FRC [31]. Different studies indicate that the circular slab element test has the advantage of formation of multiple crack pattern and high precision of determining post-cracking behavior of FRC with small scatter.

Recently, this method was extended to UHPFRC panels [12] using two different loading methods: one according to ASTM C.1550, the other one has a ring support and central loading ring originated from ASTM C.1499-05 for ceramics and glass [32], hereafter called ring-on-ring test. It was found that the UHPFRC circular slab elements using the first method always generated three major cracks located between the support points, owning to the triple axisymmetric stress distribution. In the ring-on-ring test, a uniform tensile stress field was observed within the loading ring on the bottom surface of the panels, leading to random initiation and distribution of fictitious cracks. Compared with the first test, larger crack surfaces and higher number of fictitious cracks were observed in the ring-on-ring test, which is expected to better reflect the material volume and failure mechanism in UHPFRC structural elements. Furthermore, to the best of the authors' knowledge, no studies are available in the literature focusing on the tensile strain-hardening response of UHPFRC under biaxial stress condition, which is of utmost importance both under service conditions and at ultimate limit state of UHPFRC elements.

Only few analytical models are available in the literature to predict the flexural behavior of UHPFRC slabs. Most of them [6,11,33] focused on the determination of the ultimate flexural resistance using yield line methods which have been applied for FRC slabs [21,34–37]. Spasojevic [6] observed a plastic behavior of UHPFRC slabs of various thickness (40~60mm), similar to RC slabs. The resistant plastic moment was calculated by assuming pseudo-plastic yielding in tension of UHPFRC. However, this assumption neglects the contributions from both the stress increase in the strain-hardening domain and from fictitious cracks in the tensile softening domain, leading to underestimate the flexural resistance.

The present research has the objective to investigate experimentally and analytically the biaxial flexural response of strain-hardening UHPFRC circular slab elements, with special emphasis on the tensile strain-hardening behavior of UHPFRC. First, the biaxial flexural response of circular UHPFRC slab elements is characterized by means of the ring-on-ring test. The fracture process, in particular the development of matrix discontinuities, is studied using digital image correlation (DIC) analysis. Then, a simplified inverse analysis based on slab bending and yield line theories is proposed to determine the tensile properties of strain-hardening UHPFRC under biaxial stress condition. Finally, the flexural and tensile responses as obtained from the ring-on-ring test and 4PBT results are compared.

2. Experimental investigation

2.1 Material and specimen preparation

The tested UHPFRC is an industrial premix containing 3.8% by volume of straight steel fibers with length of 13mm and diameter of 0.175mm. The water to cement ratio is 0.15 (Table 1). At 28 days, the UHPFRC has an average elastic modulus of 49GPa and compressive strength of 185MPa, measured using cylinders of 70mm diameter.

Table 1 Composition of UHPFRC

Components		Quantity
Premix (cement. Additions, quartz sand)		1970
Water	kg/m³	175
Specific superplasticizer		29
Steel fibers ($l_f = 13mm$, $d_f = 0.175mm$, $V_f = 3.8\%$)		298.3

Table 2 gives an overview of different types of specimens used in the present experimental program, in which 4 circular slab elements with diameter of 1200mm and thickness of 50 mm are used for the ring-on-ring test, and 14 extracted plates from one circular slab element for 4PBT (Figure 3-c). A thickness of 50mm is representative of the thin elements as found in numerous UHPFRC applications.

Table 2 Overview of tested specimens

Test Method	Dimension	Number of specimens	Fabrication
Ring-on-ring test	Φ1200×50 mm	4	Cast from the center in the circular formwork individually
4PBT	500×100×50 mm	10	Extracted from one circular slab element

Regarding the casting for circular slab elements, the fresh self-compacting UHPFRC (with slump flow of 700mm) was poured on the center area of the formwork from where it has flown (without any pulling or vibration) to fill entirely the formwork (Figure 2-b). After casting, a plastic sheet was pulled over the slabs to allow for curing. The formworks were removed 24 hours later. The slab elements were then kept under moist curing conditions at 20℃ and 100%

humidity during the following seven days, and subsequently were stored inside the laboratory until testing. The age at testing was more than 60 days when over 90% of the UHPFRC final material properties were attained [38,39].

Figure 2 Specimen preparation:
(a) circular formwork; (b) casting method; (c) extracted plates for 4PBT

2.2 Test method and procedure

2.2.1 Ring-on-ring test

Figure 3 shows the full test setup and instrumentation for the ring-on-ring test. The circular slab element was simply supported on a support ring with *R=500 mm* (span *l=1000mm*) and thickness of 50 mm. The loading was imposed by a hydraulic jack under displacement control, acting at the center of the slab through a force transmitting ring with *r=150 mm* and height of 30mm. Based on slab bending theory [40], the inner part of the UHPFRC slab is under pure bending by a uniformly distributed unit moment m_i given by equation (1):

$$m_i = \frac{F_i}{8\pi}\left[\frac{(1-v)(R^2-r^2)}{R^2} - 2(1+v)\ln\frac{r}{R}\right] \tag{1}$$

As derived from a liner elasticity theory [40,41], the maximum flexural strength σ_i at the bottom surface of the slab under biaxial stress condition is equal to

$$\sigma_i = \frac{3F_i}{2\pi h^2}\left[\frac{(1-v)(R^2-r^2)}{2R^2} - (1+v)\ln\frac{r}{R}\right] \tag{2}$$

where F_i is the recorded force, v is the Poisson's ratio and *h* is the thickness of the specimen.

The slabs were tested with the casting surface facing up, allowing the observation of tensile crack propagation on the smooth sheathed surface. Before testing, the casting surface was polished using a hand-held grinding machine, and a mortar layer was placed between the support ring and the bottom surface to level out both surfaces. Two rubber pads (thickness of *10 mm*, *E=500 MPa*) were positioned between the slab surfaces and the two rings to distribute the force evenly.

During testing, all the UHPFRC slabs were subjected first to three loading–unloading cycles to *15 kN* with an actuator displacement rate of 1.0 *mm/min*. Afterwards, a monotonic loading with the same displacement rate was applied up to the maximum force. Then, a rate of *4.0*

mm/min was applied until the actuator displacement reached 80 mm or the steel plate above the force transmitting ring touched the specimen. A force cell installed between the jack and the specimen was used to record the force with a frequency of *5 Hz*.

The 3D Digital Image Correlation (DIC) system and two series of LVDTs were adopted to measure the damage processes and deflection during the whole testing:

By means of the DIC technique, full-field strains and fracture process were observed during the whole test. Two digital cameras were placed underneath the slab at a distance of *0.5m* and an angle of 23 degrees to the vertical. The targeted area was about *Ø600mm* on the on the sheathed surface at the slab center. During preparation, this surface was painted with matte white paint and then sprayed to obtain a black speckle pattern with a size of about 0.5mm. For the present case, the expected DIC measurement accuracy was about 1μm.

On the top surface of the slab, one Linear Variable Displacement Transducers (LVDT) was placed at the center to measure the central deflection, and three LVDTs at an angle of 120 degrees were placed above the position of rubber pad to record the corresponding deformation.

The recordings of the two cameras of the DIC system were synchronized via wired computer control with a frequency of 0.2 Hz, while the recording by the LVDTs was 5 Hz. All deflection measurements were made with respect to the strong floor.
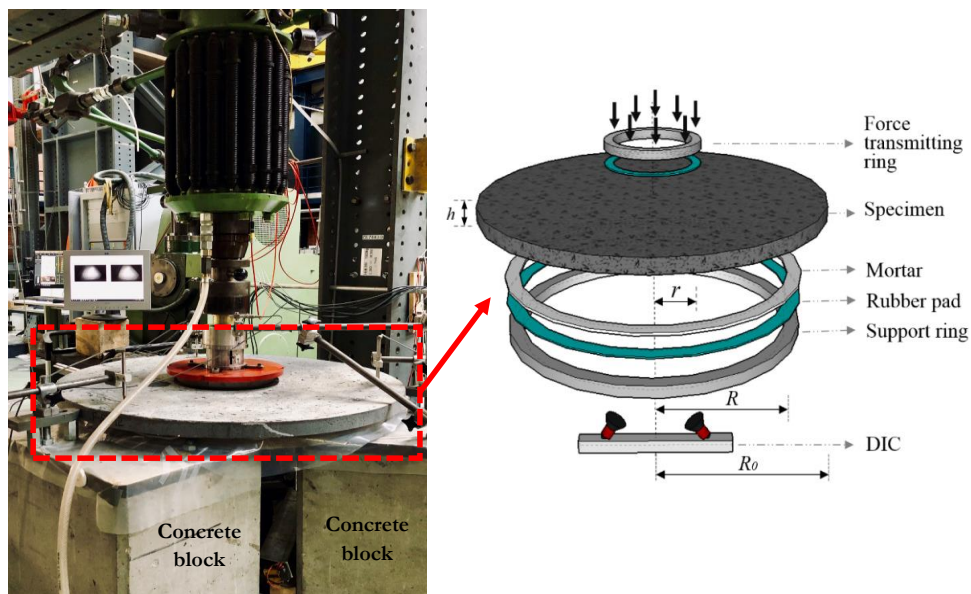

Figure 3 Schematic description of test setup and devices

2.2.2 Four-point bending test (4PBT)

The extracted plates for 4PBT were tested and instrumented according to Figure 4, with a span *l=420mm*. Based on the liner elasticity theory, the flexural strength σ_i at the bottom surface of the plate under uniaxial stress condition is determined using equations (3):

$$\sigma_i = \frac{F_i l}{bh^2} \qquad (3)$$

During testing, the plates were placed with their sheathed surface down where under the tensile stress, similar with the UHPFRC slabs for ring-on-ring test. Besides the two symmetrical LVDTs measuring the central deflection, the DIC was applied to record the damage process: the targeted area was 160×100 mm on the sheathed surface covering the constant moment part of the plates during the whole testing. The speckle size was around 0.5mm, and the corresponding DIC measurement accuracy can reach around 1µε. The 4PBT was performed on a servo-hydraulic testing machine with displacement rate of 0.5 mm/min pre-peak and 5 mm/min post-peak.

(a) two application points of the displacements;
(b) reference wafer fixed on the upper specimen surface;
(c) metallic frame placed at mid-height of the specimen.
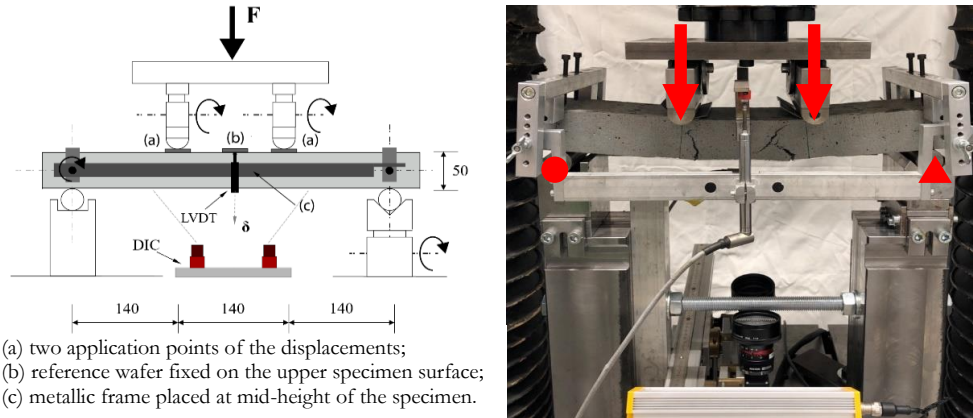
Figure 4 4PBT setup and instrumentation for rectangular plates (unit: mm)

3. Experimental results and discussion

3.1 Ring-on-ring test results

3.1.1 Force-deflection response

The ring-on-ring test results of four UHPFRC circular slab elements are presented in terms of force vs. central deflection (F-δ), in which the thick curve refers to the average response (Figure 5). Accordingly, Table 3 summarizes the characteristic flexural parameters for each slab, including the elastic limit (corresponding to force F_e and deflection δ_e), peak point (F_p and δ_p). Here, the deflection values are determined by DIC analysis on the bottom surface, excluding the deformation of rubber pad measured from three LVDTs on the top surface. The recorded force values are modified considering the real thickness of each slab by using the term $(h/h_i)^2$, where $h = 50mm$ is the nominal thickness and h_i is the measured thickness of each slab. The average curve is obtained through averaging the four curves, which are normalized by each ultimate limit, respectively. The determination of elastic limit (point A, corresponding to F_e and δ_e) is determined when an irreversible decrease of 5% of the moving scant modulus of F-δ curve is observed firstly. This result is validated against the DIC analysis results in section 3.1.3, where the first matrix discontinuity is detected.

As shown in Figure 5 and Table 3, all slabs show consistent flexural responses with small scatter under ring-on-ring testing. In the elastic domain (O-A), a linear F-δ response is observed, and the elastic limit is in the range of *0.18 F_p ~ 0.22 F_p* with average of *0.20F_p*. Afterwards, a large non-linear part until the peak limit (point C) is highlighted, where significant stress redistribution in the slab is expected. It is noted that the scant modulus of the curve decreases slightly at the beginning of this domain, hereafter called quasi-elastic domain (A-B). The determination of the quasi-elastic limit (point B) is based on DIC analysis, as described in the following section. The rest of the non-linear part (B-C) with significant deflection hardening behavior is called hardening domain in this study. Beyond maximum force, during the softening domain (C-D), the slabs exhibited important ductility with high residual resistance. D is a random point at the end of the softening domain.
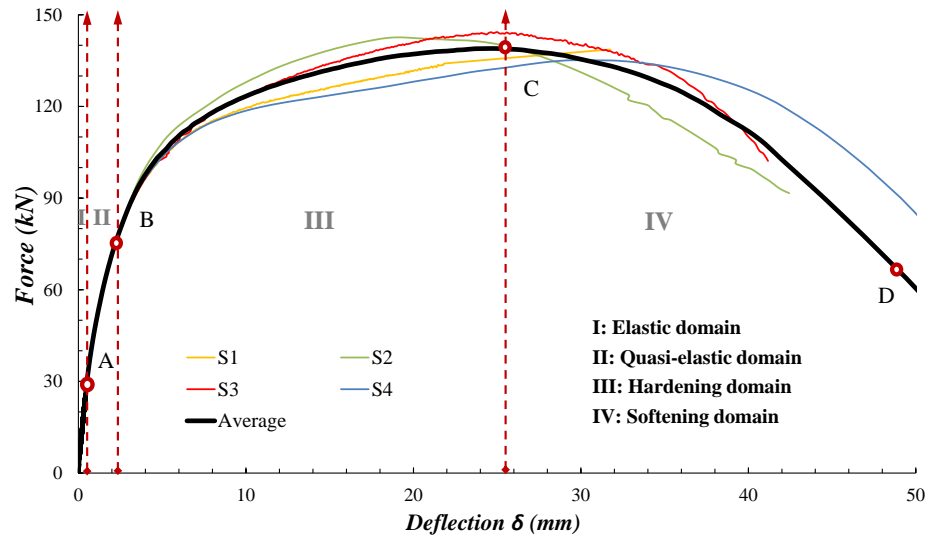
Figure 5 Force-deflection response from ring-on-ring tests

Table 3 Biaxial flexural parameters from ring-on-ring tests

No.	F_e (kN)	$\sigma_e(f_{Ute})$ (MPa)	δ_e (mm)	w_e (mm)	F_{qe} (kN)	σ_{qe} (MPa)	δ_{qe} (mm)	w_{qe} (mm)	F_p (kN)	σ_p (MPa)	f_{Utu} (MPa)	δ_p (mm)	w_p (mm)	n	h (mm)
S1	25.43 (0.18F_p)	8.31	0.40	0.014	75.15 (0.54F_p)	24.61	2.20	0.089	138.66	45.42	14.21	31.75	3.60	8	50.30
S2	28.89 (0.20F_p)	9.46	0.53	0.011	83.70 (0.59F_p)	27.41	2.65	0.087	142.64	46.72	14.62	19.06	1.70	7	51.81
S3	28.23 (0.20F_p)	9.17	0.45	0.011	74.14 (0.51F_p)	24.29	2.14	0.087	144.38	47.29	14.80	25.01	2.85	6	50.48
S4	29.40 (0.22F_p)	9.62	0.66	0.009	82.40 (0.56F_p)	26.99	2.08	0.067	146.74	48.07	13.35	29.46	4.63	7	46.43
Average	27.99 (0.20F_p)	9.14	0.51	0.011	78.85 (0.55F_p)	25.83	2.27	0.083	143.11	46.87	14.08	26.32	3.20	-	-
Std. dev.	1.77	0.58	0.11	0.002	4.90	1.60	0.26	0.01	3.14	1.12	0.30	5.59	1.24	-	-
CV	0.06	0.06	0.22	0.18	0.06	0.06	0.11	0.13	0.02	0.02	0.02	0.21	0.39	-	-

3.1.2 Failure mode

All UHPFRC slabs failed in flexural fracture mode with pronounced cracking, characterized by several randomly distributed dominant fictitious or real cracks surrounded by multiple fine fictitious cracks. Figure 6 illustrates the cracking pattern (visible by the naked eyes) on the bottom surface of the four UHPFRC slabs at the end of testing, in which the thick lines refer to dominant fictitious cracks or real cracks and the thin ones stand for fine fictitious cracks.

Notably, in all UHPFRC slabs, the fictitious and real cracks are largely concentrated within the area surrounded by the force transmitting ring; the numbers of dominant fictitious cracks and real cracks (n) are similar, ranging from 6~8 (Table 3). However, the cracking patterns, especially the distribution of fine fictitious cracks, are random and the propagation paths of cracks are irregular. This enables the slight variation in F-δ curves once the fictitious cracks start to propagate (after B). For example, compared with the rest, S1 generated the most amount of fine fictitious cracks, allowing for more contribution from fiber bridging effect, and consequently, leading to the highest deflection hardening behaviour given δ_p=31.75mm (65% more than that from S2 with least number of fine fictitious cracks).
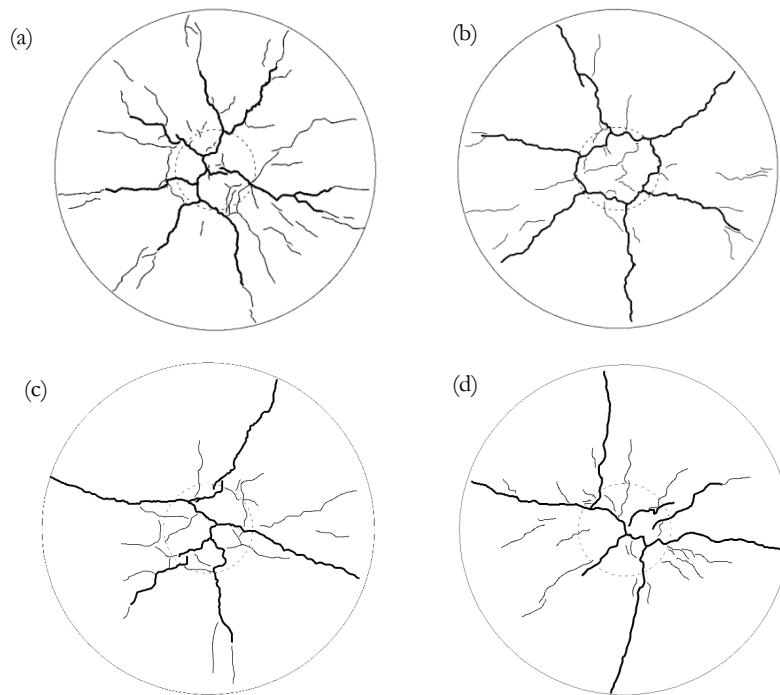
Figure 6 Final fracture patterns after testing (a) S1, (b) S2, (c) S3, (d) S4

3.1.3 Fracture process

Based on DIC analysis using VIC-3D, the whole fracture process of each UHPFRC slab under testing was captured. Note that initiation and propagation of matrix discontinuities are invisible to the naked eye and could not be measured using traditional sensors, but are detected on DIC strain contours. Figure 7 shows the fracture process observed on slabs S3 and S4,

considered to be representative. Several DIC strain contours are selected to illustrate the fracture characteristics in different phases in terms of F-δ curve. The white dashed circle marks the position of the force transmitting ring on the bottom surface of UHPFRC slab, and the lines with different colors mark the matrix discontinuities and fictitious cracks. On this basis, the elastic limit (point A) can be validated by the first existence of matrix discontinuity, shown on the DIC strain contour. The quasi-elastic limit (point B) is determined when the strain concentration starts on one or several matrix discontinuities, represented by the green lines on the DIC strain contour in this study. The corresponding values (F_{qe} and δ_{qe}) are also given in Table 3. F_{qe} is in the range of $0.51F_p$ to $0.59F_p$ with an average of $0.55F_p$.

It was observed that all the slabs under ring-on-ring test show similar fracture process (Figure 7), characterized as follows:

(1) Once the elastic limit (A) is reached, single or several matrix discontinuities indicated by the blue lines, initiate randomly on the bottom surface of the slab within the force transmitting ring area, where pure bending moment is acting. Afterwards, these matrix discontinuities propagate irregularly, and a large amount of new matrix discontinuities are produced and distributed randomly within the force transmitting ring area in this quasi-elastic domain.

(2) At the quasi-elastic limit (point B), one or several fine fictitious cracks (green lines) are firstly detected by DIC analysis, and more appear as the force increases. These fine fictitious cracks develop from some of previous matrix discontinuities in Phase II. They concentrate within the force transmitting ring area.

(3) At ultimate limit (point C), several fictitious cracks become dominant, and cannot be covered by DIC strain contours due to the large opening. They propagate radially from the center to the edge in the subsequent softening domain (phase IV). No more new matrix discontinuities or fictitious cracks appear in this domain.
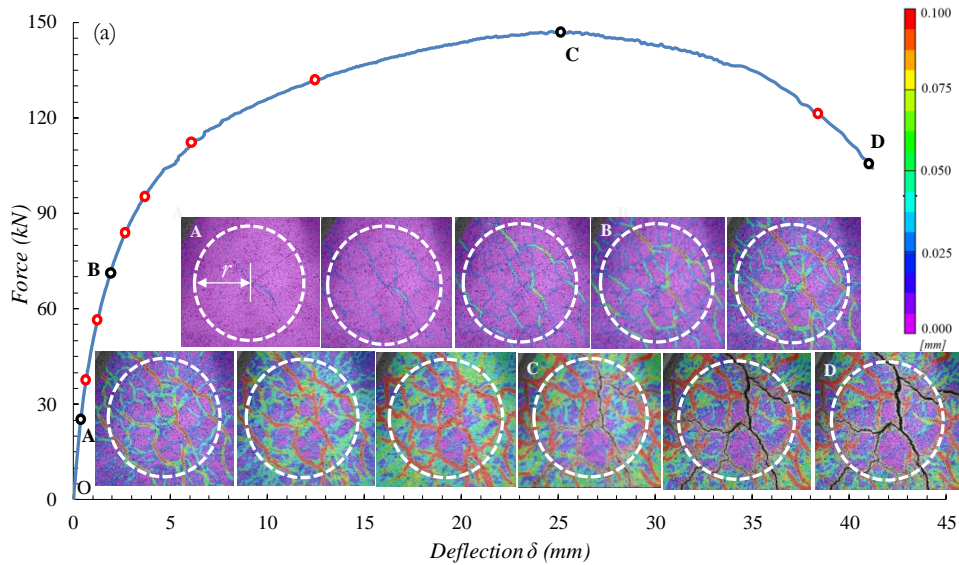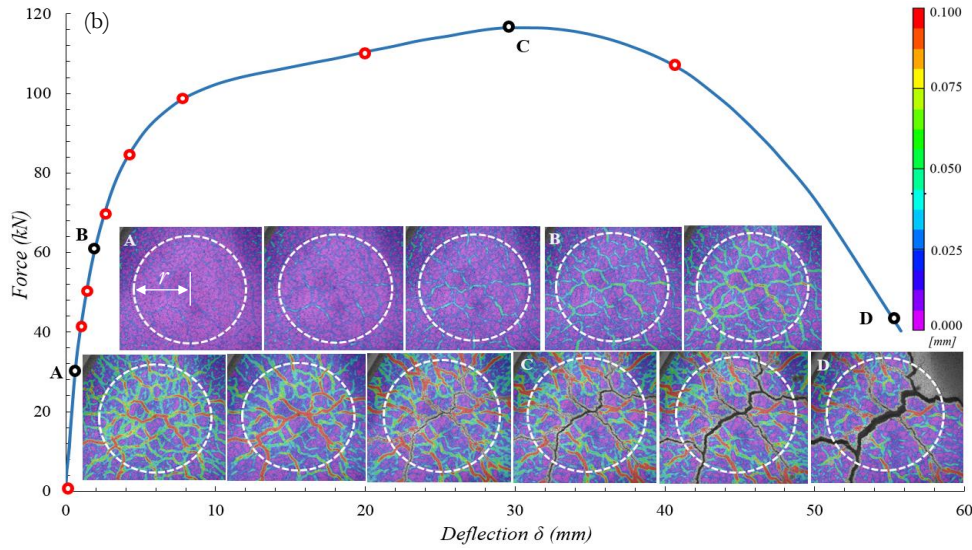
Figure 7 Fracture process of UHPFRC slab under ring-on-ring test: (a) S3; (b) S4

3.1.4 Development of matrix discontinuities and fictitious cracks opening

Using the virtual extensometers of the DIC analysis tool, the opening response of every single matrix discontinuity and fictitious crack is recorded over the entire testing duration. The virtual extensometers, with measurement length of about 15mm, are set separately to be perpendicular to the propagation path and located at the critical part of each target. In order to obtain actual opening values, the contribution from the elastic deformation within the measurement length is deduced. All UHPFRC slabs show similar opening development responses, Figures 8 and 9 present the opening vs. force *(w-F)* and opening vs. deflection *(w-δ)* curves from slab S3 as example.

A large amount of matrix discontinuities and fictitious cracks with a wide range of openings is observed, and three characteristic types of opening responses can be identified. The green lines, referring to the development of matrix discontinuities, has maximum opening less than 0.1mm, and start to close partially before ultimate limit. It is noted that the residual openings of matrix discontinuities at the end of testing are all less than 0.05mm. Part of the fictitious cracks with maximum opening less than 1.5mm, indicated by the blue lines, nearly stop development once reaching the peak limit. The others (black lines) become dominant fictitious cracks and develop rapidly with increase in deflection in the softening domain.

In accordance with the F-δ response and cracking process (Figure 7), the opening development responses can be subdivided into four phases. The maximum openings at different characteristic limits (w_e, w_{qe} and w_p) are determined for each slab, as summarized in Table 3. In the elastic domain, all curves nearly coincide together, and only the deformation of matrix is measured. The curves in the quasi-elastic domain show almost linear responses although lower scant modulus is found compared with the elastic domain. Only the matrix discontinuities are observed, and the maximum opening is less than 0.1mm in this domain. Afterward, the hardening domain is characterized by propagation of multiple fictitious cracks

developed from previous matrix discontinuities. Some of these fictitious cracks become dominant once the specimen is reaching its maximum resistance, and propagate rapidly in the softening domain.
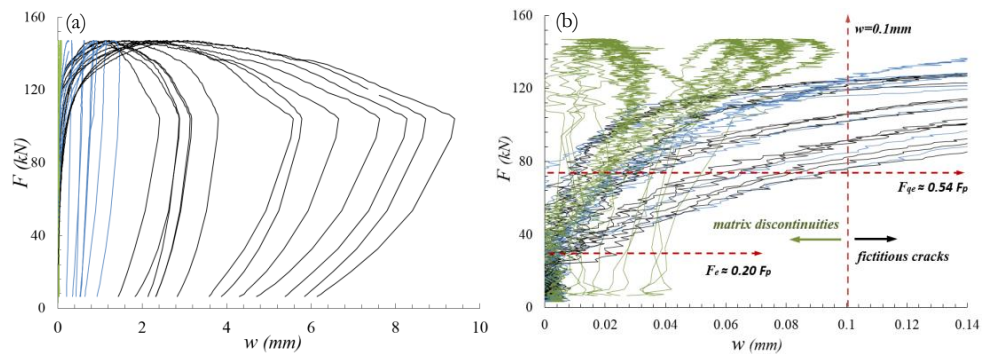
Figure 8 Representative opening – force response (w-F) of UHPFRC circular slab element: (a) overview, (b) zoom in the crack opening up to 0.14mm
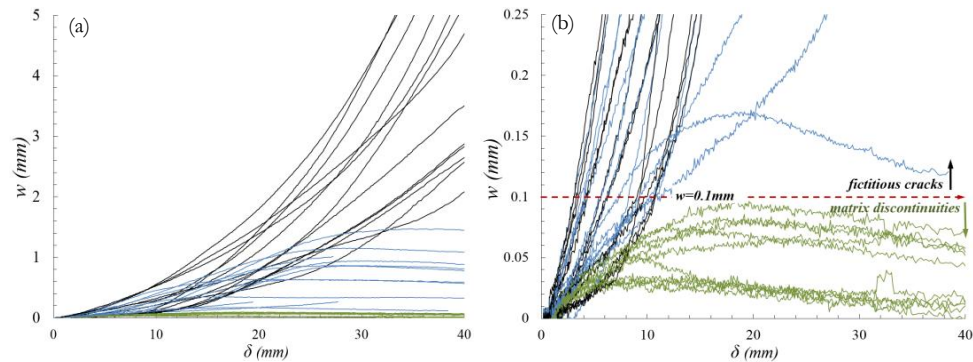
Figure 9 Representative opening – deflection response (w-δ) of UHPFRC circular slab element: (a) overview, (b) zoom in the crack opening up to 0.25mm

3.2 4PBT results

The force-deflection curves from different UHPFRC plates under 4PBT are shown in Figure 10, where a four-domain response can be identified. The characteristic flexural parameters for each plate are summarized in Table 4. The determination of these parameters is based on the aforementioned methodology used for ring-on-ring tests. In addition, the DIC strain contours on tensile surface within the constant moment zone are given for all plates at the elastic limit point B, quasi-elastic limit point C and end of testing (point D), respectively. In general, the flexural responses from different plates agree well until reaching the quasi-elastic limit, and afterward, varying largely in terms of force-deflection curve and cracking pattern with increase of deflection.
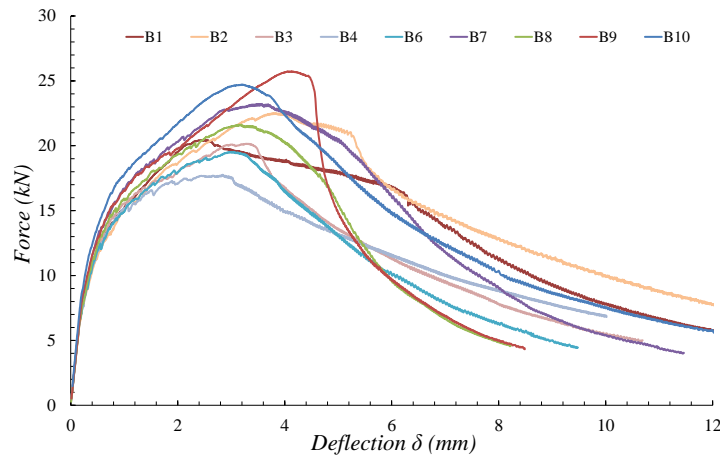
Figure 10 Force-deflection responses from 4PBT

With respect to the fracture process and opening response, all UHPFRC plates show consistent responses under 4PBT. The example of specimen B1 is illustrated in Figures 11 and 12. The first matrix discontinuity initiates randomly at elastic limit ($F_e \approx 0.31F_p$). Afterward, the multiple matrix discontinuities develop in the quasi-elastic domain. Once reaching the quasi-elastic limit (at $F_{qe} \approx 0.70F_p$), the strain starts to concentrate on one or several adjacent matrix discontinuities, and propagate from one edge to the other of the plate, evolving into one single fictitious crack (or narrow fracture zone) at maximum force (F_p). It's interesting to note that the force-opening curves change sharply at around F_{qe}, as shown in Fig12(b). During the softening domain, the single fictitious crack develops rapidly in terms of opening, while the other matrix discontinuities unload partially with residual opening less than 0.02mm at the end of testing.
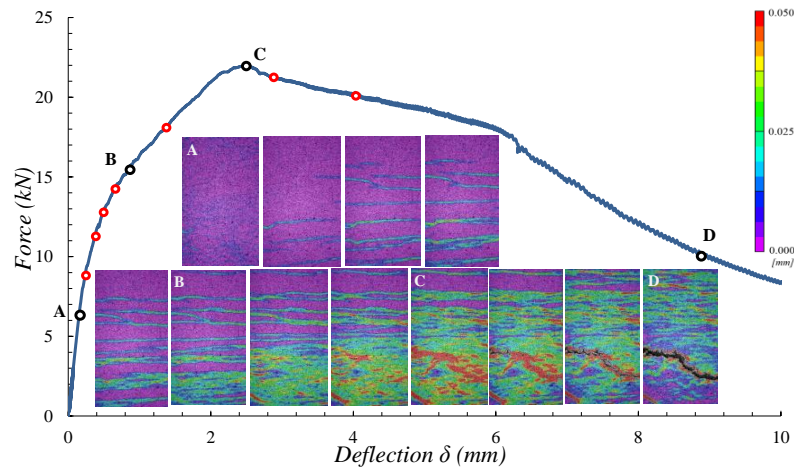
Figure 11 Representative fracture process of UHPFRC plate under 4PBT (B1)
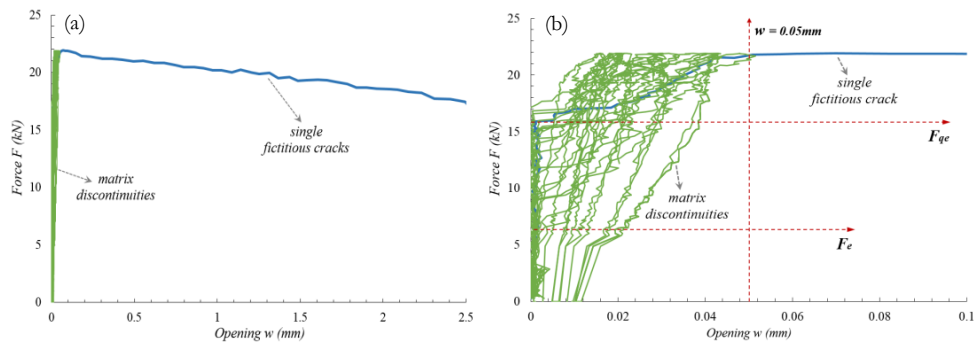
Figure 12 Representative force – opening (F-w) curve of UHPFRC plate:
(a) overview, (b) zoom in the opening up to 0.1mm

3.3. Comparison between ring-on-ring test and 4PBT results

Based on previous testing results, the flexural strength, fracture process (including development and opening of matrix discontinuities and fictitious crack), and energy absorption capacity are compared in different characteristic domains. For direct comparison, the flexural strength vs. normalized deflection referring to the span length (σ-δ/l) curves from two different tests are shown in Figure 13. The flexural strength under ring-on-ring test and 4PBT are calculated using equation (2) and (3), respectively. The corresponding values at different characteristic limits are summarized in Tables 3 and 4.
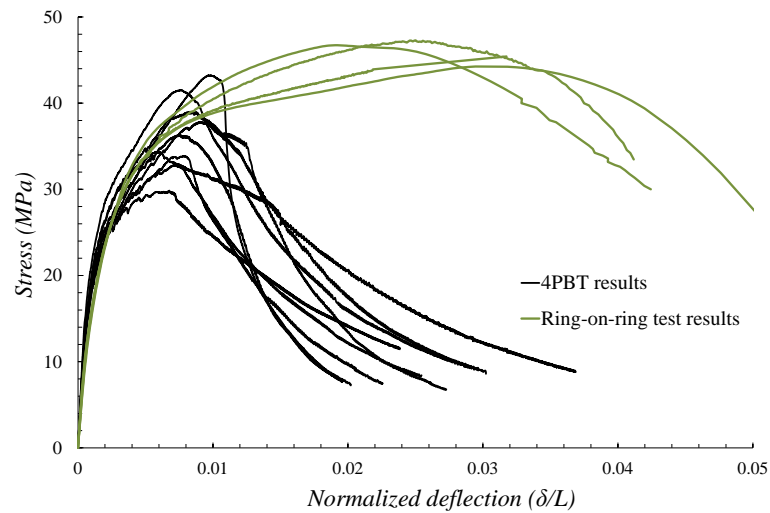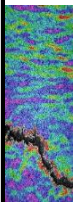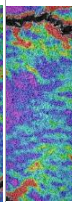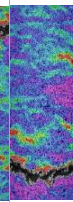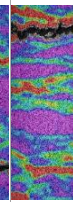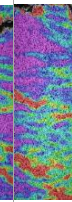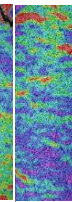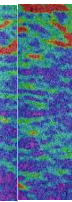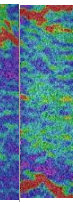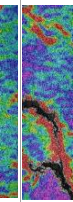
Figure 13 Equivalent flexural tensile stress vs. normalized deflection (σ-δ/l) curves

Table 4 Uniaxial flexural parameters from 4PBT

No.	F_e [kN]	$\sigma_e(f_{te})$ [MPa]	F_{qe} [kN]	σ_{qe} [MPa]	w_{qe} [mm]	F_p [kN]	σ_p [MPa]	f_{Utu} [MPa]	w_p [mm]	DIC strain contours at F_{qe} (point B)	at F_p (point C)	at point D	Remark
B1	6.12 (0.30 F_p)	10.29	14.82 (0.73 F_p)	24.89	0.031	20.42	34.30	13.16	0.07				-
B2	6.40 (0.28 F_p)	10.74	16.41 (0.73 F_p)	27.56	0.029	22.47	37.74	14.49	0.06				Two localized cracks, the first one is out of constant moment zone.
B3	6.15 (0.31 F_p)	10.33	14.36 (0.71 F_p)	24.13	0.039	20.15	33.86	12.97	0.12				-
B4	6.19 (0.35 F_p)	10.40	12.72 (0.72 F_p)	21.37	0.035	17.70	29.74	11.43	0.18				Two localized cracks, the second one is out of constant moment zone.
B6	7.10 (0.36 F_p)	11.93	12.98 (0.66 F_p)	21.80	0.025	19.52	32.79	12.56	0.20				The localized crack is under the loading point or slightly out of constant moment zone, so the corresponding datas are still considered as valid in present study.
B7	6.71 (0.29 F_p)	11.27	16.34 (0.71 F_p)	27.46	0.040	23.16	38.90	14.94	0.20				
B8	6.70 (0.31 F_p)	11.26	14.94 (0.69 F_p)	25.10	0.041	21.57	36.24	13.91	0.12				
B9	7.79 (0.30 F_p)	13.09	17.00 (0.66 F_p)	28.55	0.036	25.70	43.17	16.56	0,20				
B10	7.61 (0.31 F_p)	12.79	16.38 (0.66 F_p)	27.52	0.025	24.69	41.48	15.90	0.13				The localized crack initiate slightly out of constant moment zone
Average	6.75 (0.31 F_p)	11.34	15.11 (0.70 F_p)	25.38	0.03	21.71	36.47	13.99	0.14				
Std. dev.	0.63	1.05	1.55	2.61	0.01	2.56	4.30	1.65	0.06				
CV	0.09	0.09	0.10	0.17	0.19	0.12	0.12	0.12	0.40				

[a] B5 with strain-softening behavior is not considered in this study.

In the elastic domain, the flexural responses in terms of σ-δ/l curves from both tests almost coincide with little scatter, as shown in Figure 13. It appears, however, that the flexural strength σ_e at elastic limit from ring-on-ring test is in average around 19% smaller than the one from 4PBT. This can be attributed to the fact that a large zone of circular slab element is under pure bending field in arbitrary directions, while a relatively small zone of the rectangular plate is under pure bending field in only one direction. Thus, it is plausible that the initiation of the first matrix discontinuity occurs earlier in the ring-on-ring test, given the stochastic nature of UHPFRC material. However, this finding does not coincide with Kim et al. [7] who reported a lower value of σ_e from 4PBT.

Regarding the quasi-elastic domain, the flexural response under 4PBT varies slightly among the different plates due to the variation of matrix discontinuities distribution (Table 4). This mainly results from the intrinsic heterogeneity of local fiber distribution, as reported by [17,18,42]. In the case of the ring-on-ring test, the influence of heterogeneity can be largely compensated by the stress redistribution in the circular slab elements, where a nearly uniform network of matrix discontinuities at quasi-elastic limit is observed (Figure 7). The consistent response thus is obtained in this domain in the ring-on-ring test. It is noted that the matrix discontinuity openings at quasi-elastic limit (w_{qe}) from the ring-on-ring test is in the range of 0.050mm to 0.089mm with average of 0.08mm, more than two times larger than the one from the 4PBT ($0.029mm \leq w_{qe} \leq 0.041mm$ with average of $0.03mm$); while the corresponding flexural strength (σ_{qe}) from both tests are nearly identical in average.

During the hardening domain, only single fictitious crack form in the 4PBT. Large scatter of flexural response is obtained due to the variation of fiber distribution in the different plates. Similar experimental evidence is reported from different studies [13–16,43,44]. In contrast, the circular slab elements show stable results in the hardening domain, and are characterized by much larger fracture zones with multiple fictitious cracks. This implies the important stress redistribution owing to the fiber bridging effect in different directions. Regarding ultimate flexural strength at ultimate limit F_p, the average value from the ring-on-ring test is 46.87MPa, comparable to the average value (50.77 MPa) reported in [12], where a different UHPFRC mix (V_f=2.0%, l_f/d_f=19.5/0.2) and circular slab element geometry (Φ=480mm, h=48mm) was used. This value is roughly 28% higher than the one from the 4PBT. Furthermore, the corresponding average energy absorption capacity at F_p is more than 3 times higher than the one from the 4PBT (36.47 MPa). Furthermore, the corresponding average energy absorption capacity at F_p is more than 3 times higher than the one from the 4PBT.

4. Simplified inverse analysis

Different inverse analysis methods based on the force-deflection curve from 4PBT have been proposed as an indirect method for characterizing the uniaxial tensile behavior of UHPFRC [45–49], and even standardized in UHPFRC codes [8,9]. It appears, however, that inverse analysis of ring-on-ring test results has not yet been conducted.

Stating that the flexural tensile stress obtained from the elastic limit of the force-deflection curve is equal to the elastic limit stress of UHPFRC material (as described in section 3.3), this chapter focuses on the determination of the tensile strength of UHPFRC based on inverse analysis from both types of testing. The inverse analysis of 4PBT results standardized in [8] is briefly described [30], and the inverse analysis of ring-on-ring test results is proposed based on the yield line theory [50,51].

4.1 Four-point bending test (4PBT)

Based on a series of finite element analysis for strain hardening UHPFRC under 4PBT [13,45], it has been observed that the position of the neutral axis of a bending specimen at maximum force F_p is consistently at $0.82h$ from the tensile surface. Thus, the tensile strength of UHPFRC is calculated according to equation (4) following the stress distribution shown in Figure 14(b):

$$f_{Utu} = 0.383 \frac{F_p l}{b h^2}$$

(4)
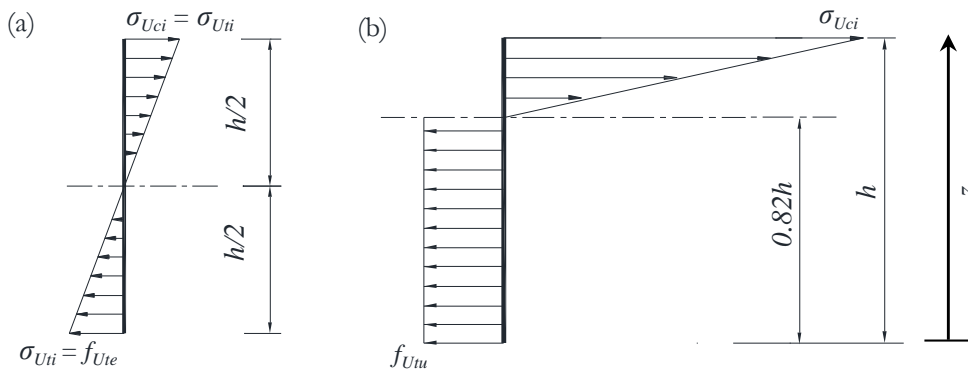
Figure 14 Sectional distributions of stress: (a) at elastic limit; (b) at maximum force

4.2 Ring-on-ring test

Based on the static boundary conditions of the UHPFRC circular slab element under ring-on-ring test, radial and circumferential yield lines are assumed as illustrated in Figure 15. This yield lines correspond to actual failure modes presented in section 3.1.

The external work W_{ext} for the virtual displacement δ_p at ultimate limit F_p is

$$W_{ext} = F_p \delta_p \tag{5}$$

Based on the assumed yield lines, the internal work W_{int} is

$$W_{int} = 2\pi m_r{}^u \varphi + 2\pi(R-r)m_t{}^u \varphi = 2\pi\delta_p(m_r{}^u \frac{r}{R-r} + m_t{}^u) \tag{6}$$

where $\varphi = \frac{\delta_p}{R-r}$ is the rotation angle of single segment, $m_r{}^u$ and $m_t{}^u$ are the moments per unit length along the radial and tangential directions, respectively.

Thus, considering energy balance $W_{ext} = W_{int}$, the F_p is obtained:

$$F_p = 2\pi(m_r{}^u \frac{r}{R-r} + m_t{}^u) \tag{8}$$
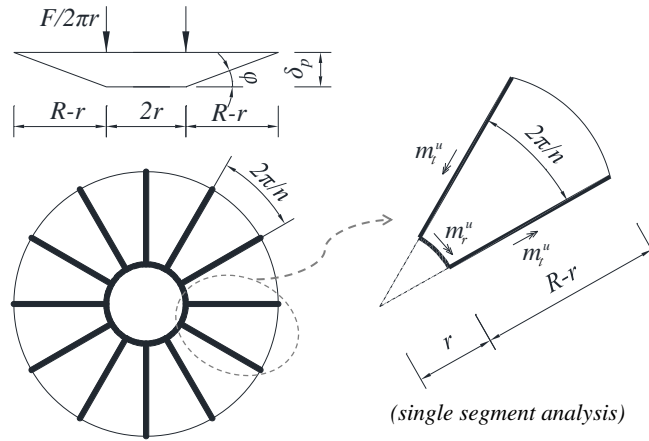
Figure 15 Assumed yield lines

As reported by Baril et al. [11], the flexural plastic moment per unit length of thin UHPFRC slab element at ultimate limit is close to the one from bending beam under 4PBT. Thus, following the sectional stress distribution given in Figure 14(b) for 4PBT:

$$m_r{}^u = m_t{}^u = \frac{1}{2.3}h^2 f_{Utu} \tag{9}$$

Combining equations (8) and (9), the biaxial tensile strength of UHPFRC is obtained:

$$f_{Utu} = 1.15 \frac{F_p}{\pi h^2} \frac{R-r}{R} \tag{10}$$

4.3 Comparison

The calculated values of uniaxial and biaxial tensile strength f_{Utu} of UHPFRC material using respectively equations (4) and (10) are given in Tables 3 and 4. It is observed that the ring-on-ring test yields consistent results, while 4PBT shows considerable variation. The average value of biaxial tensile strength from the ring-on-ring test is almost equivalent to the uniaxial tensile strength obtained from the 4PBT as determined from inverse analysis.

5. Conclusions

The biaxial flexural response of strain-hardening UHPFRC circular slab elements is investigated experimentally and analytically using the ring-on-ring test. By means of DIC analysis, the full fracture process of UHPFRC circular slab element is captured. Particularly, the quasi-elastic limit is determined, and the development of matrix discontinuities in the quasi-elastic domain is studied. Additionally, ring-on-ring and 4PBT testing results are compared based on experimental evidence and simplified inverse analysis. The ring-on-ring test yields stable results towards a consistent characterization of the biaxial flexural response of UHPFRC.

The main conclusions are:

(1) The quasi-elastic limit, representing the initiation of strain concentration based on DIC analysis, corresponds to roughly 55% of maximum force under ring-on-ring testing condition, while it is at 70% of maximum force under 4PBT. The corresponding flexural tensile stresses at the quasi-elastic limit as obtained from both tests, are nearly identical.

(2) At the quasi-elastic limit, a larger number of matrix discontinuities with maximum opening of 0.08mm is observed on the UHPFRC slab element under ring-on-ring testing, while less matrix discontinuities with maximum opening of 0.03mm are found for the 4PBT. This implies that the strain-hardening behavior of UHPFRC is further developed under biaxial stress condition compared with uniaxial stress condition.

(3) The flexural strength at ultimate limit under ring-on-ring testing is roughly 28% higher than the one obtained from 4PBT. The corresponding energy absorption capacity under ring-on-ring testing is more than 3 times higher than the one from 4PBT, suggesting significant strain redistribution capacity of UHPFRC.

(4) The biaxial flexural responses from the ring-on-ring tests show random distribution and uniform network of matrix discontinuities in the quasi-elastic domain, as well as multiple fictitious cracks in the hardening domain. This represents realistically the large volume involved and fracture mechanism of real UHPFRC structural elements.

(5) According to the simplified inverse analyses based on, respectively, the slab bending theory and the yield line theory, the elastic limit of strain-hardening UHPFRC under biaxial tensile stress condition is in average around 19% smaller than under uniaxial stress condition, while the tensile strength is almost equivalent to the one obtained under uniaxial condition.

6. References

[1] Brühwiler E. "Structural UHPFRC" to enhance bridges. Keynote Lecture, 2nd International Conference on UHPC Materials and Structures (UHPC 2018 - China), Fuzhou, China: 2018, p. 140–158.

[2] X. Shen, E. Brühwiler, Characterization of Tensile Beahvior in UHPFRC Thin Slab Using NDT Method and DIC System, in: Proceedings PRO 129, Fuzhou, China, 2018.

[3] A. Hillerborg, Analysis of one single crack, Fracture Mechanics of Concrete (Developments in Civil Engineering). (1983) 223–249.

[4] E. Denarié, E. Brühwiler, Cast-on site UHPFRC for improvement of existing structures–achievements over the last 10 years in practice and research, in: 7th Workshop on High Performance Fiber Reinforced Cement Composites, 1-3, June 2015, Stuttgart, Germany, 2015.

[5] T. Guenet, F. Baby, P. Marchand, L. Sorelli, S. Bernardi, F. Toutlemonde, Flexural failure modes and ductility assessment of ribbed triangular UHPFRC plates, in: HiPerMat 2016-4th International Symposium on Ultra-High Performance Concrete and High Performance Construction Materials, 2016: p. 9p.

[6] A. Spasojevic, Structural implications of ultra-high performance fibre-reinforced concrete in bridge design, École polytechnique fédérale de Lausanne (EPFL), 2008.

[7] J. Kim, D.J. Kim, S.H. Park, G. Zi, Investigating the flexural resistance of fiber reinforced cementitious composites under biaxial condition, Composite Structures. 122 (2015) 198–208.

[8] SIA 2052. Technical Leaflet SIA 2052 UHPFRC – Materials, design and construction, March 2016. (In German and French).

[9] N. AFNOR, P18-710: National addition to Eurocode 2–Design of concrete structures: Specific rules for ultra-high performance fiber-reinforced concrete (UHPFRC), Association Française de Normalisation, 2016.

[10] Ferrara L, Cremonesi M, Faifer M, Toscani S, Sorelli L, Baril M-A, et al. Structural elements made with highly flowable UHPFRC: Correlating computational fluid dynamics (CFD) predictions and non-destructive survey of fiber dispersion with failure modes. Engineering Structures 2017;133:151–71.

[11] Baril MA, Sorelli L, Réthoré J, Baby F, Toutlemonde F, Ferrara L, et al. Effect of casting flow defects on the crack propagation in UHPFRC thin slabs by means of stereovision Digital Image Correlation. Construction and Building Materials 2016;129:182–92.

[12] D.-Y. Yoo, G. Zi, S.-T. Kang, Y.-S. Yoon, Biaxial flexural behavior of ultra-high-performance fiber-reinforced concrete with different fiber lengths and placement methods, Cement and Concrete Composites. 63 (2015) 51–66.

[13] Bastien-Masse M, Denarié E, Brühwiler E. Effect of fiber orientation on the in-plane tensile response of UHPFRC reinforcement layers. Cement and Concrete Composites 2016;67:111–25.

[14] C. Oesterlee, Structural response of reinforced UHPFRC and RC composite members (doctoral thesis, 4848), École polytechnique fédérale de Lausanne (EPFL), 2010.

[15] Duque LFM, Graybeal B. Fiber orientation distribution and tensile mechanical response in UHPFRC. Mater Struct 2017;50:1–17.

[16] A. Simon, D. Corvez, P. Marchand, Feedback of a ten years assessment of fibre distribution using K factor concept, in: UHPFRC 2013 - International Symposium on Ultra-High Performance Fibre-Reinforced Concrete, MARSEILLE, France, 2013: pp. 669–678.

[17] O. Bayard, O. Ple, G. Bernier, Internal Heterogeneity in a Reactive Powder Concrete, in: 6th RILEM Symposium on Fibre-Reinforced Concretes, Varenna-Lecco, Italy, 2004: pp. 20–22.

[18] O. Bayard, Approche multi-échelles du comportement mécanique des bétons à ultra hautes performances renforcés par des fibres courtes, PhD Thesis, Cachan, Ecole normale supérieure, 2003.

[19] M. di Prisco, P. Martinelli, A numerical approach for the evaluation of the structural redistribution coefficient KRd, Computational Modelling of Concrete Structures-Proc. of EURO-C. 1 (2014) 503–512.

[20] Cavalaro SHP, Aguado A. Intrinsic scatter of FRC: an alternative philosophy to estimate characteristic values. Mater Struct 2015;48:3537–55.

[21] Minelli F, Plizzari G. Derivation of a simplified stress–crack width law for Fiber Reinforced Concrete through a revised round panel test. Cement and Concrete Composites 2015;58:95–104.

[22] D. Dozio, M. Di Prisco, SFRC Structures: Identification of the Uniaxial Tension Characteristic Constitutive Law: PhD Thesis: Academical Year 2007-2008, Politecnico di Milano, 2008.

[23] di Prisco M, Plizzari G, Vandewalle L. Fibre reinforced concrete: new design perspectives. Mater Struct 2009;42:1261–81.

[24] Rambo DAS, Silva F de A, Toledo Filho RD. Mechanical behavior of hybrid steel-fiber self-consolidating concrete: Materials and structural aspects. Materials & Design (1980-2015) 2014;54:32–42.

[25] Bernard ES. Correlations in the behaviour of fibre reinforced shotcrete beam and panel specimens. Mat Struct 2002;35:156–64.

[26] fib Model Code 2010, Comite´ Euro-International du Beton-Federation Interantional de la Precontrainte, Lausanne, 2010.

[27] Prisco M di, Colombo M, Dozio D. Fibre-reinforced concrete in fib Model Code 2010: principles, models and test validation. Structural Concrete 2013;14:342–61.

[28] P. Marti, T. Pfyl, V. Sigrist, T. Ulaga, Harmonized Test Procedures for Steel Fiber-Reinforced Concrete, MJ. 96 (1999) 676–685.

[29] Barnett SJ, Lataste J-F, Parry T, Millard SG, Soutsos MN. Assessment of fibre orientation in ultra high performance fibre reinforced concrete and its effect on flexural strength. Mater Struct 2009;43:1009–23.

[30] Mitchell MR, Link RE, Minelli F, Plizzari G. A New Round Panel Test for the Characterization of Fiber Reinforced Concrete: A Broad Experimental Study. J Test Eval 2011;39:103392.

[31] C. ASTM, 1550:'Standard Test Method for Flexural Toughness of Fiber-Reinforced Concrete (Using Centrally-Loaded Round Panel), ASTM, West Conshohocken, Pa, 2008.

[32] C. ASTM, 1499-05. Standard test method for monotonic equibiaxial flexural strength of advanced ceramics at ambient temperature, ASTM International, West Conshohocken, Pennsylvania. (2009).

[33] L. Moreillon, J. Nseir, R. Suter, Shear and flexural strength of thin UHPC slabs, in: Proceedings of Hipermat, 2012: pp. 748–756.

[34] Nour A, Massicotte B, De Montaignac R, Charron J-P. Derivation of a crack opening deflection relationship for fibre reinforced concrete panels using a stochastic model: Application for predicting the flexural behaviour of round panels using stress crack opening diagrams. Cement and Concrete Research 2011;41:964–74.

[35] D. Fall, J. Shu, R. Rempling, K. Lundgren, K. Zandi, Two-way slabs: Experimental investigation of load redistributions in steel fibre reinforced concrete, Engineering Structures. 80 (2014) 61–74.

[36] ACI Committee 544, ACI 544. 6R-15 Report on Design and Construction of Steel Fiber-Reinforced Concrete Elevated Slabs, American Concrete Institute, 2015.

[37] Salehian H, Barros JAO. Prediction of the load carrying capacity of elevated steel fibre reinforced concrete slabs. Composite Structures 2017;170:169–91.

[38] K. Habel, Structural behaviour of elements combining ultra-high performance fibre reinforced concretes (UHPFRC) and reinforced concrete, 2004.

[39] Habel K, Viviani M, Denarié E, Brühwiler E. Development of the mechanical properties of an Ultra-High Performance Fiber Reinforced Concrete (UHPFRC). Cement and Concrete Research 2006;36:1362–70.

[40] S. Timoshenko, S. Woinowsky-Krieger, Theory of plates and shells, (1959).

[41] Yoo D-Y, Banthia N, Zi G, Yoon Y-S. Comparative Biaxial Flexural Behavior of Ultra-High-Performance Fiber-Reinforced Concrete Panels Using Two Different Test and Placement Methods. Journal of Testing and Evaluation 2017;45:20150275.

[42] P. Hadl, H. Kim, N.V. Tue, Experimental investigations on the scattering in the post cracking tensile behaviour of UHPFRC, in: Proceedings of the Internatinal Symposium on Ultra-High Performance Concrete and High Performance Materials (HiperMat 2016), Kassel, 2016.

[43] Zhou B, Uchida Y. Influence of flowability, casting time and formwork geometry on fiber orientation and mechanical properties of UHPFRC. Cement and Concrete Research 2017;95:164–77.

[44] Zhou B, Uchida Y. Relationship between fiber orientation/distribution and post-cracking behaviour in ultra-high-performance fiber-reinforced concrete (UHPFRC). Cement and Concrete Composites 2017;83:66–75.

[45] Denarié E, Sofia L, Brühwiler E. Characterization of the tensile response of strain hardening UHPFRC - Chillon Viaducts. AFGC-ACI-Fib-RILEM Int Symposium on Ultra-High Performance Fibre-Reinforced Concrete, UHPFRC 2017, 2017.

[46] López JÁ, Serna P, Navarro-Gregori J, Coll H. A simplified five-point inverse analysis method to determine the tensile properties of UHPFRC from unnotched four-point bending tests. Composites Part B: Engineering 2016;91:189–204.

[47] López JÁ, Serna P, Navarro-Gregori J, Camacho E. An inverse analysis method based on deflection to curvature transformation to determine the tensile properties of UHPFRC. Mater Struct 2015;48:3703–18.

[48] SAMARIS D26, Modelling of UHPFRC in composite structures, European project 5th FWP / SAMARIS – Sustainable and Advanced MAterials for Road Infrastructures – WP 14: HPFRCC, http://samaris.zag.si/, 2006.

[49] Baby F, Graybeal B, Marchand P, Toutlemonde F. UHPFRC tensile behavior characterization: inverse analysis of four-point bending test results. Mater Struct 2013;46:1337–54.

[50] K.W. Johansen, Yield-line theory, Cement and Concrete Association, 1962.

[51] R. Park, W.L. Gamble, Reinforced concrete slabs, John Wiley & Sons, 1999.

Paper III

An Analytical Inverse Analysis to Determine Biaxial Tensile Behavior of Strain-Hardening UHPFRC from Ring-on-Ring Test

ABSTRACT

The equi-biaxial tensile properties of strain-hardening UHPFRC is determined and investigated based on an original analytical inverse analysis of results from ring-on-ring tests. First, the analytical inverse analysis method is developed based on the elastic slab bending and yield line theories. Using this method, a new objective criterion for the determination of the elastic limit stress of strain-hardening UHPFRC is provided, and a point-by-point inverse analysis is used to obtain the strain value at the end of hardening. This method reduces uncertainties regarding assumptions and avoids any iterative procedures. The inverse analysis results are put into perspective with experimental evidence, particularly based on DIC measurements. Moreover, the uniaxial tensile properties are also derived from the inverse analysis of 4PBT results and compared with the equi-biaxial tensile properties from the proposed inverse analysis. The inverse analysis results show a 18% lower elastic limit stress, and almost equivalent tensile strength of UHPFRC subjected to equi-biaxial stresses, compared with the corresponding values from uniaxial stress. Moreover, a relatively small equi-biaxial strain at the end of hardening is highlighted.

1. Introduction

The precise and reliable knowledge of tensile properties and constitutive laws of materials is most important for structural design and safety verification. This is particular so for tensile strain-hardening Ultra-High Performance Fiber Reinforced Cementitious Composites (UHPFRC), which exhibit relatively high elastic limit stress ($\geq$ 8 MPa), high tensile strength ($\geq$ 10 MPa) and significant deformation capacity with strain up to 5‰ at the end of hardening when subjected to uniaxial tension. Taking benefit from these properties, UHPFRC are generally used for thin slab-like structural elements, which provide the required resistance against bending, shear and fatigue even without ordinary steel reinforcement bars [1–3]. Typical structural applications include cast-in place UHPFRC layers for strengthening of reinforced concrete slabs [4,5], slabs of new bridges and buildings as well as shells [6,7]. These innovative applications are now spreading rapidly worldwide under the impulse of pioneering countries such as Switzerland [4,5], China [8], Malaysia [9] and others. Such structural UHPFRC systems are generally subjected to multiple-axial stresses [10], hereafter called equi-biaxial stresses, where different tensile properties may be expected compared to uniaxial stress condition. Thus, the equi-biaxial tensile response of UHPFRC needs to be known and characterized accurately.

It is well known that there is no unique tensile response for discontinuous fiber reinforced cementitious composites, especially for strain-hardening UHPFRC with relatively high fiber volume content ($V_f \geq$ 3.0%), which is influenced largely by the action of the fibrous skeleton in materials [11–13]. In the case of equi-biaxial tensile response, such influence may even be more significant, given that the effect of fiber distribution in different directions is involved. Swanepoe [14] conducted biaxial direct tensile tests (DTT) on strain-hardening cement-based composites (SHCC). The confinement effect was proven to occur due to the action of fibers in both directions, leading to different failure mechanism compared with that under uniaxial condition. Similar findings were observed by Yoo et al. [10,15] for UHPFRC specimens under equi-biaxial flexure, where considerably higher flexural strength and normalized energy absorption capacity were observed under equi-biaxial stresses condition compared to those under uniaxial stress condition.

The DTT appears to be the most suitable and straightforward method to quantify the tensile behavior of materials. The uniaxial DTT has been applied extensively for characterization of the uniaxial tensile response of UHPFRC by different researchers [16–19]. However, few studies to characterize the biaxial tensile response of UHPFRC are available. This can be attributed to the various difficulties in preparing and performing biaxial DTT, since at least two actuators in both perpendicular directions and a large frame are generally necessary. In addition, many challenges pertaining to uniform load distribution, frictional effect, accurate boundary condition and load control need to be addressed carefully. Ple et al. [20] investigated experimentally and numerically the biaxial tensile behavior of Reactive Powder Concrete (RPC, one specific type of UHPFRC) using an original biaxial cruciform specimen under a systematic program. However, the strains measured from two orthogonal directions were not symmetrical despite symmetric loading, which could be attributed to the asymmetry of rigidity between the specimen and the machine. Besides, the study in [20] was restricted to the linear behavior.

On the other hand, the flexural test provides an easy-to-conduct method to derive indirectly the tensile response of materials based on the inverse analysis of test results. This method is generally performed by means of either analytical solutions or numerical approach through reproducing the flexural measurement results like force-deflection curves. Currently, various inverse analyses have been widely applied to characterize the uniaxial tensile properties of UHPFRC [11,21–25] using four-point bending testing (4PBT), and some of them are even standardized in UHPFRC standards like SIA 2052 [26] and NF P18-710 [27].

In addition, a flexural test using circular slab specimen (circular slab test) was described as valuable alternative to the 4PBT and square slab test for fiber reinforced concrete (FRC) [28]. Based on a general theoretical approach considering the random fiber distribution and successive softening by fiber pullout, an effective flexural tensile strength and a fracture energy parameter were proposed to characterize the strength and toughness of FRC. Compared with the results from 4PBT and square slab test, the circular slab test provided more reliable results. This method is also standardized in the recommendation SIA 162/6 for FRC [29,30].

More recently, the ring-on-ring test similar to the one used to characterize ceramics and glass according to ASTM C. 1499-05 [31], has been applied successfully to investigate the equi-biaxial flexural behavior of UHPFRC [15,32]. A circular slab specimen is simply supported on a ring support and the external loading is uniformly distributed on a central loading ring from the top. Thus, the central part of the specimen is in pure bending condition, produced by a uniformly distributed moment according to the elastic slab bending theory [33]. Unfortunately, there is no study available in the literature concerning an inverse analysis from this test.

The principle objective of the present study is to determine the equi-biaxial tensile properties of strain-hardening UHPFRC based on an original inverse analysis method for the ring-on-ring test configuration. First, the analytical inverse analysis of the ring-on-ring test, extending from [11] for 4PBT, is developed based on the elastic slab bending and yield line theories. This method provides a new objective criterion for determining the elastic limit stress of strain-hardening UHPFRC, and a point-by-point inverse analysis is used to obtain the strain at the end of hardening of UHPFRC. Afterward, the inverse analysis results are validated against the experimental evidence, especially based on DIC analysis. Moreover, the uniaxial tensile properties are derived from the inverse analysis of 4PBT results and compared with the equi-biaxial tensile properties as obtained from the proposed inverse analysis of ring-on-ring test results.

2. Proposed analytical inverse analysis method

2.1 Overview

In this section, the proposed analytical inverse analysis, following the approach from [11] using an uniaxial flexural test (4PBT), is developed first based on the force-deflection response from a equi-biaxial flexural test (ring-on-ring test). Figure 1 shows the typical force–deflection curve of UHPFRC specimen under flexure, where points A' and C' stand for the elastic limit and peak force

of flexural response, respectively. It is well known that part of the UHPFRC material close to the tensile surface of the specimen is already in the strain softening domain at point C'. Thus, a damage localization point, hereafter referred as point B' in Figure 1, is expected between point A' and C', from which the softening response of UHPFRC specimen enters into play.
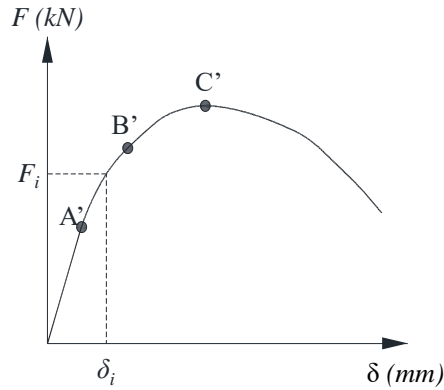
Figure 1 Typical force-deflection curve under flexure

The principle of the proposed method is to convert pairs of measured force F_i and deflection δ_i at characteristic points under equi-biaxial flexure into corresponding pairs of equi-biaxial tensile stress and strain at the surface of the specimen in the constant moment zone under tension. This is achieved based on: (1) the hypotheses of the classic elastic slab bending theory [33], and (2) the equilibrium of moments and normal forces in a sectional analysis. In addition, the strain distribution in the sectional analysis is considered as linear; and the compressive behavior of UHPFRC is assumed to be linear elastic. The curvature in the constant moment zone is assumed to be identical in all directions.

2.2 Analytical basis

As for the ring-on-ring test, the circular slab is simply supported on a ring with radius of R, and the recorded force F as a result of the imposed vertical actuator displacement is uniformly distributed along a small ring with radius r from the top. The notations and sign conventions used in the analysis are shown in Figure 2. Dividing the slab into two parts as shown in Figure 2 (b) and (c), it may be seen that the inner portion of the slab is in the condition of pure bending produced by the uniformly distributed moment m_i per unit length and that the outer part is bent by m_i and the shearing force q_i per unit length.
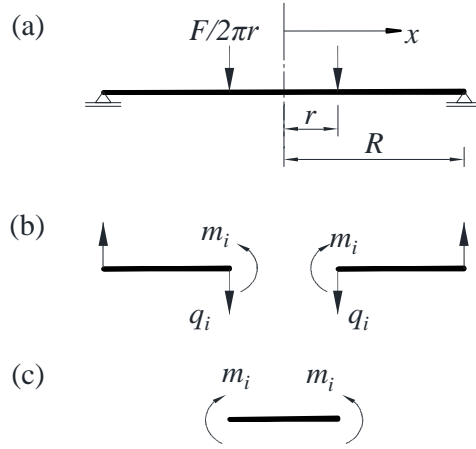
Figure 2 Schematic description of ring-on-ring test

Based on the elastic slab bending theory [33], the uniformly distributed moment m_i per unit length acting on the inner portion of slab is given by equation (1):

$$m_i = \frac{F_i}{8\pi}\left[\frac{(1-v)(R^2-r^2)}{R^2} - 2(1+v)\ln\frac{r}{R}\right] \tag{1}$$

with the central deflection δ_i:

$$\delta_i = \frac{F_i}{8\pi D}\left[\frac{(3+v)(R^2-r^2)}{2(1+v)} + r^2\ln\frac{r}{R}\right] \tag{2}$$

where v is the Poisson's ratio. The value of v is assumed as a typical value of 0.2 for UHPFRC during elastic domain and set as 0 after elastic limit in present study. The value $D = \frac{E}{1-v^2}\frac{h^3}{12}$ is the elastic flexural stiffness of the slab.

2.3 Determination of equi-biaxial tensile elastic modulus and elastic limit stress

The determination of equi-biaxial tensile elastic modulus and elastic limit stress requires using the elastic limit point A' under flexure. The point A' generally corresponds to the loss of linearity in the force-deflection curve. However, point A' is not easy to be obtained directly from the curve due to the high ductility of UHPFRC [11,21], and thus, a reliable and representative criterion to determine the elastic limit is necessary. In this section, a criterion based on an irreversible decrease of the moving average elastic modulus E_{mi}, similar with the one defined in [11], is introduced.

Transformed from equation (2), the elastic modulus E_i for each pair of measured force and central deflection (F_i, δ_i) is:

$$E_i = \frac{3(1-v^2)}{2\pi h^3}\frac{(F_i-F_0)}{(\delta_i-\delta_0)}\left[\frac{(3+v)(R^2-r^2)}{2(1+v)} + r^2\ln\frac{r}{R}\right] \tag{3}$$

where (F_0, δ_0) is the reference point at the beginning of the force-deflection curve.

Then the moving average E_{mi} is calculated from at least 10 values of E_i in the elastic domain after the initial domain of specimen response, and plotted as a function of the measured deflection δ_i. The point A' (corresponding to force F_e and deflection δ_e) thus is determined when an 1% irreversible decrease of E_{mi} is observed firstly, and the value of E_i given by equation (3) for F_e and δ_e is defined as the equi-biaxial tensile elastic modulus E_U of the UHPFRC material.

As derived from liner elasticity theory [33,34], the stress distribution in cross-section at point A' is assumed according to Figure 3 (a). Thus, the corresponding equi-biaxial tensile elastic limit stress f_{Ute} for F_e and δ_e is equal to

$$f_{Ute} = \sigma_{Uti} = \frac{3F_e}{2\pi h^2}\left[\frac{(1-\nu)\left(R^2-r^2\right)}{2R^2} - (1+\nu)\ln\frac{r}{R}\right] \tag{4}$$
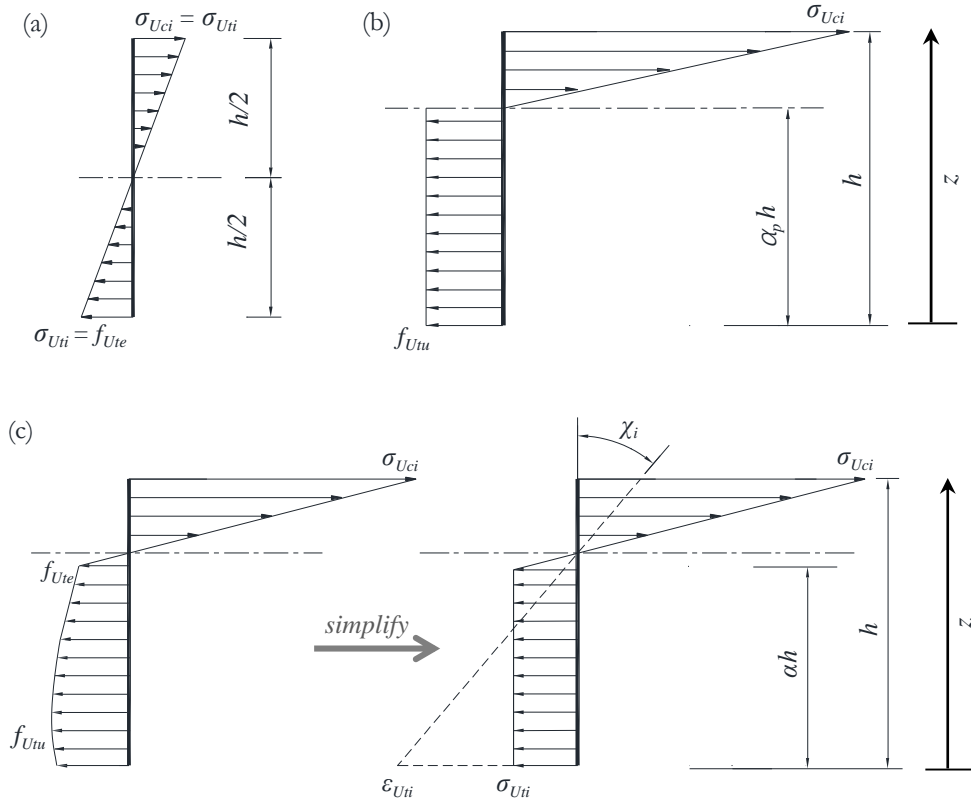
Figure 3 Stress and strain distribution of cross-section at:
(a) elastic limit; (b) ultimate limit; (c) damage localization point

2.4 Determination of equi-biaxial tensile strength

The ultimate limit point C' characterizes the maximum force measured during the ring-on-ring test of the UHPFRC slab. As demonstrated by several authors [7,35,36], the flexural resistance F_p of UHPFRC thin slab can be estimated using yield line theory [37,38]. Based on the boundary and loading conditions of UHPFRC circular slab under ring-on-ring test configuration, the crack pattern consisting of radial and tangential yield lines is assumed as shown in Figure 4, which will then be verified against the actual failure modes as observed from the test results.

The external work done, giving the virtual displacement δ_p at F_p (point C'), is

$$W_{ext} = F_p \delta_p \tag{5}$$

and the internal work done is

$$W_{int} = 2\pi m_t{}^u \varphi + 2\pi(R-r)m_r{}^u \varphi = 2\pi\delta_p(m_r{}^u \frac{r}{R-r} + m_t{}^u) \tag{6}$$

with:

$$\varphi = \frac{\delta_p}{R-r} \tag{7}$$

where φ is the rotation angle of single segment, $m_r{}^u$ and $m_t{}^u$ are the ultimate resistance moments per unit length along the radial and tangential directions, respectively.

Considering energy balance, $W_{ext} = W_{int}$, the flexural resistance F_p is determined:

$$F_p = 2\pi(m_r{}^u \frac{r}{R-r} + m_t{}^u) \tag{8}$$
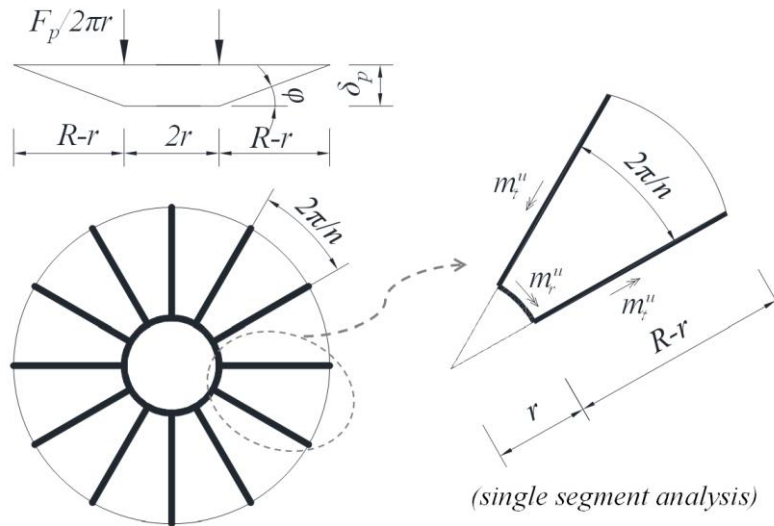
Figure 4 Assumed yield lines

At point C', multiple fictitious cracks are largely developed with relatively small stress transfer between fictitious crack surfaces, and a considerable part of the tensile zone of UHPFRC enters into the softening domain. Following [11], the stress distribution in the cross-section can thus be assumed as illustrated in Figure 3(b), in which $\alpha_p h$ is the height of neutral axis. As reported by Baril et al. [35], the maximum plastic moment of the UHPFRC slab is similar to the one obtained from beam bending under 4PBT configuration. Thus, the value of α_p is set as 0.82 at point C', following [11,12] based on non-linear finite element analysis. This leads to:

$$m_r{}^u = m_t{}^u = \frac{1}{2.3} h^2 f_{Utu} \tag{9}$$

Combining equations (8) and (9) allows to obtain the equi-biaxial tensile strength:

$$f_{Utu} = 1.15 \frac{F_p}{\pi h^2} \frac{R-r}{R} \tag{10}$$

2.5 Determination of equi-biaxial strain at the end of hardening

The damage localization point B' is required for the determination of equi-biaxial strain at the end of hardening. In present method, an additional criterion linked to the equi-biaxial tensile strength as determined using equation (10) is introduced. Noting that the inverse analysis is invalid beyond point B'.

In the central portion of UHPFRC slab under the force transmitting ring, considering the uniformly distributed moment m_i per unit length, the values of curvature χ_i are given by equation (11); they are assumed to be identical in all directions.

$$\chi_i = \frac{m_i}{D(1+v)} \tag{11}$$

Combined with equations (1) and (3), the curvature χ_i from equation (11) in the central portion of slab is obtained for every pair of measured force and central deflection (F_i, δ_i) according to:

$$\chi_i = \frac{2(1-v)(R^2-r^2)/R^2 - 4(1+v)\ln\frac{r}{R}}{(3+v)(R^2-r^2) + 2r^2(1+v)\ln\frac{r}{R}} \delta_i \tag{12}$$

It should be noted that equation (12) is based on elastic structural mechanics and considered as reasonably valid for nonlinear behavior. Similar approach is adopted in [11,24,25].

For the points between the elastic and ultimate limits, the sectional stress and strain distribution in a section is determined according to Figure 3 (c). By assuming that E_U is constant in all directions, the stress is thus expressed as a function of depth z from tensile surface, the yielding zone height αh and σ_{Uti}

$$\sigma(z) = \begin{cases} \sigma_{Uti} & if\ 0 \leq z \leq \alpha h \\ \sigma_{Uti} + \frac{(z-\alpha h)\chi_i E_U}{1-\nu} & if\ \alpha h \leq z \leq h \end{cases} \qquad (13)$$

Consequently, the distributed axial force N_i and moment m_i per unit length in a section are obtained using equation (14) and equation (15), respectively:

$$N_i = h\sigma_{Uti} + \frac{1}{2}(1-\alpha)^2 h^2 \frac{\chi_i}{1-\nu} E_U \qquad (14)$$

$$m_i = \frac{1}{2}h^2\sigma_{Uti} + (\frac{1}{3} - \frac{\alpha}{2} + \frac{\alpha^3}{6})^2 h^3 \frac{\chi_i}{1-\nu} E_U \qquad (15)$$

Based on the equilibrium of forces in sectional analysis, namely $N_i = 0$:

$$2\alpha^3 - 3\alpha^2 + 1 - \frac{12(1-\nu)m_i}{h^3\chi_i E_U} = 0 \qquad (16)$$

Based on the equilibrium of moments in sectional analysis, namely combining equation (16) with equation (1), the value of α_i is determined. Subsequently, the equi-biaxial tensile stress σ_{Uti} and deformation ε_{Uti} at the tensile surface of the central part of slab are determined using equation (17) and equation (18), respectively:

$$\sigma_{Uti} = \frac{1}{2}(1-\alpha_i)^2 h \frac{\chi_i}{1-\nu} E_U \qquad (17)$$

$$\varepsilon_{Uti} = \frac{(1-\nu)\sigma_{Uti}}{E_U} + \alpha_i\chi_i h \qquad (18)$$

The inverse analysis then is performed for a series of points evenly distributed between the force range of $0.50F_p$ to $0.80F_p$. The first point "j" for which the calculated stress σ_{Utj} is larger than the value of f_{Utu} according to equation (10) gives an estimate of the equi-biaxial strain at the end of hardening of the UHPFRC, namely $\varepsilon_{Utu} = \varepsilon_{Utj}$.

3. Results of inverse analyses

3.1 Experimental campaign

Two experimental campaigns are conducted to investigate the uniaxial and equi-biaxial flexural behavior of UHPFRC elements. A total of four circular slabs (diameter of 1200mm, thickness of 50 mm) are used for the ring-on-ring test; the metallic support ring and force transmitting ring have a radius of R = 500 mm and r = 150 mm, respectively. Ten rectangular plates (length of 500, width of 100mm and thickness of 50 mm), extracted from a circular slab of same fabrication, are used for 4PBT with a span of 420mm. The real geometry, especially the thickness, of each specimen has been measured precisely before testing. Figure 5 shows the full test setups and instrumentations for both tests. The net central deflection under ring-on-ring test is determined

by digital image correlation (DIC) analysis on the bottom surface, excluding the deformation of rubber pad measured from three LVDTs on the top surface. The net mid-span deflection under 4PBT is directly obtained from DIC analysis.

The tested UHPFRC is an industrial premix containing 3.8 % by volume of straight steel fibers with length of 13 mm and diameter of 0.175 mm. At 28 days, the UHPFRC has compressive strength of 185MPa, measured using cylinders of 70 mm diameter and 140 mm height.

The experimental details are reported in [32]. Only the main testing results are summarized in the following.

(a) two application points of the displacements;
(b) reference wafer fixed on the upper specimen surface;
(c) metallic frame placed at mid-height of the specimen.
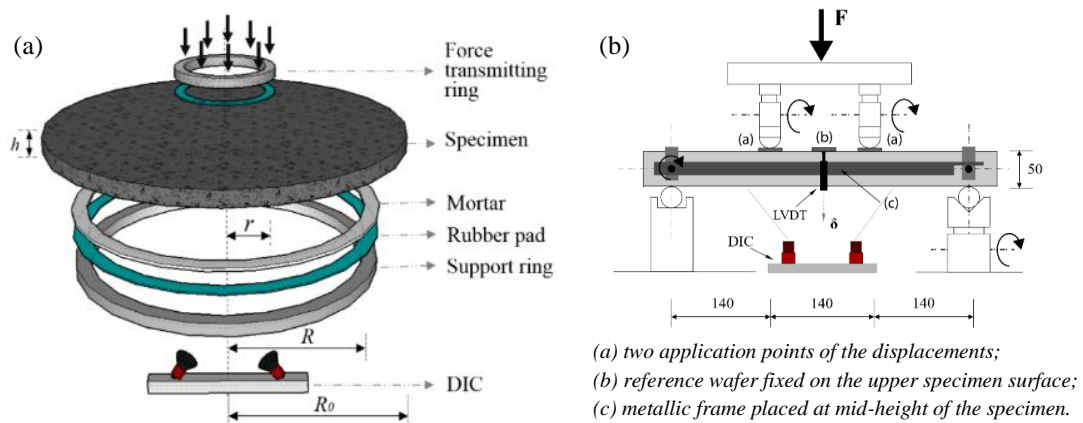
Figure 5 Schematic description of test setup and devices: (a) Ring-on-ring test; (b) 4PBT

3.2 Inverse analysis results from ring-on-ring test

3.2.1 Experimental results

The force versus central deflection (F-δ) curves of four UHPFRC circular slabs from the ring-on-ring test are presented in Figure 6, where the thick curve refers to the average response. Based on digital image correlation (DIC) analysis, Figure 7 shows the fracture process observed on bottom surface of slab S3 as representative example, in which the white dashed circle marks the position of the force transmitting ring.

In general, the ring-on-ring test yields consistent equi-biaxial flexural response. Four characteristic domains in terms of F-δ curves can be distinguished, namely, the elastic domain (OA), quasi-elastic domain (AB), hardening domain (BC) and softening domain (CD), as marked with letters A-D in Figure 7. Based on the DIC strain contours, the elastic limit (described by F_e, δ_e and w_e at point A) is determined when the first matrix discontinuity is detected, while the quasi-elastic limit (described by F_{qe}, δ_{qe} and w_{qe} at point B) refers to the start of strain concentration on one or several matrix discontinuities, implying the formation of first fictitious cracks. Accordingly, Table 1 summarizes the characteristic parameters, including force, deflection and maximum opening, at the end of each domain (point A, B and C) and for all slabs.
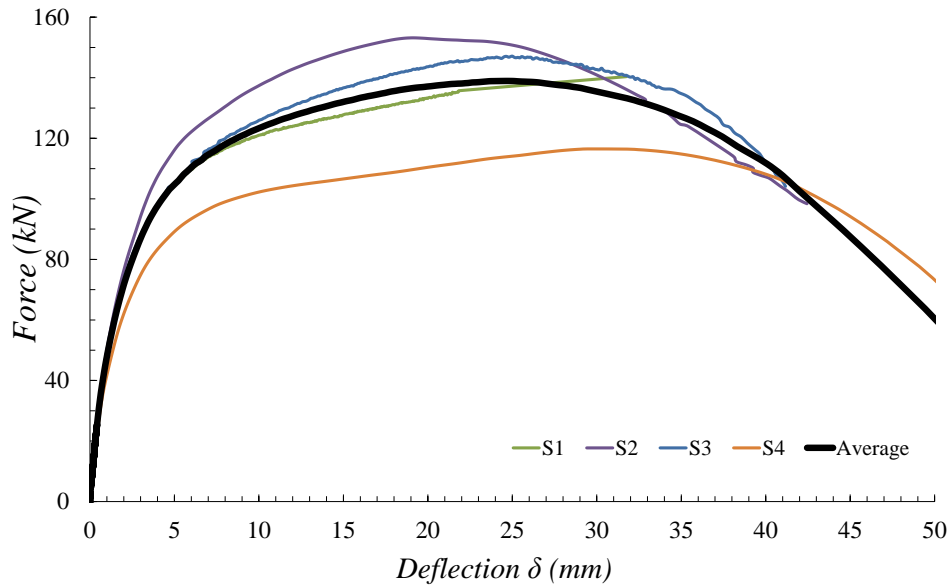
Figure 6 Force- central deflection (F-δ) curves from four quasi-static ring-on-ring tests
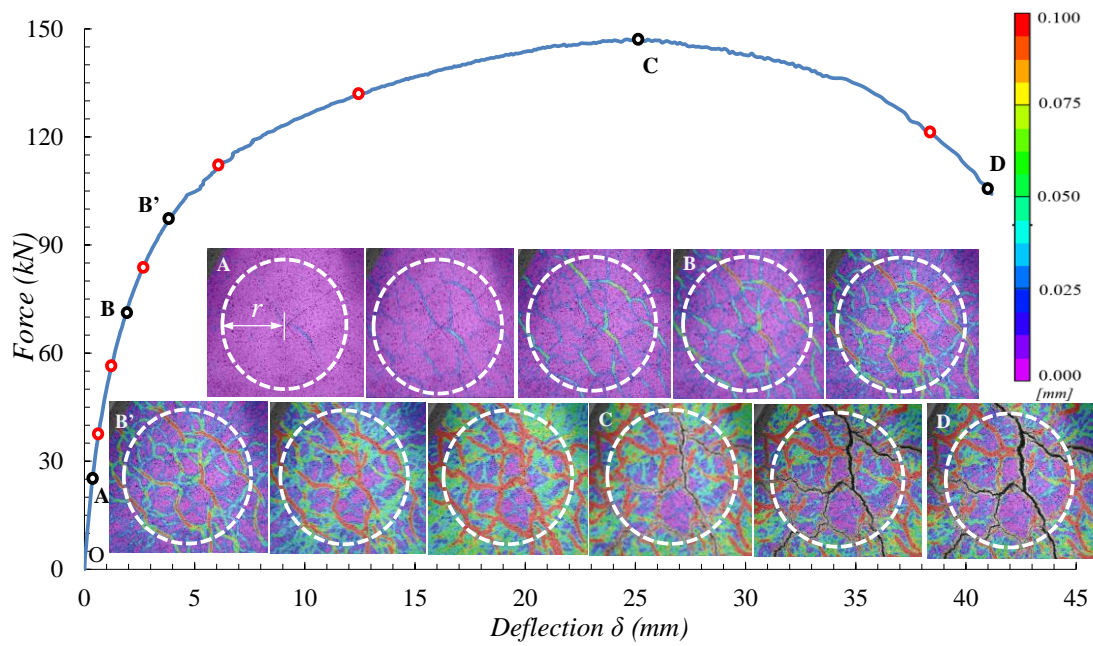
Figure 7 Example of cracking and fracture process on the tensile surface of the UHPFRC slab under quasi-static ring-on-ring testing (S3)

Table 1 Equi-biaxial flexural parameters from ring-on-ring tests

No.	h (mm)	F_e [kN]	δ_e [mm]	w_e [mm]	F_{qe} [kN]	δ_{qe} [mm]	w_{qe} [mm]	F_p [kN]	δ_p [mm]	w_p [mm]
S1	50.30	25.74 $(0.18F_p)$	0.40	0.014	76.06 $(0.54F_p)$	2.20	0.089	140.34	31.75	3.60
S2	51.81	31.02 $(0.20F_p)$	0.53	0.011	89.87 $(0.59F_p)$	2.65	0.087	153.16	19.06	1.70
S3	50.48	28.77 $(0.20F_p)$	0.45	0.011	75.56 $(0.51F_p)$	2.14	0.087	147.14	25.01	2.85
S4	46.43	25.35 $(0.22F_p)$	0.66	0.009	71.04 $(0.56F_p)$	2.74	0.067	126.51	29.46	4.63
Average	49.75	27.72 $(0.20F_p)$	0.51	0.010	78.13 $(0.55F_p)$	2.43	0.083	141.74	26.32	3.20

3.2.2 Inverse analysis results from ring-on-ring test

Figure 8 illustrates the determination of elastic limit (point A') from specimen S3 as example. According to the description in section 2.2, the evolution of moving average secant modulus E_{mi} as a function of central deflection δ_i is calculated using equation (6). Thus, following the 1% irreversible decrease criterion, the elastic limit is determined at a deflection of 0.46 mm and force of 28.77 kN, corresponding to equi-biaxial elastic limit stress of 9.17 MPa and elastic modulus of 57'500 MPa.

Figure 9 shows the determination of damage localization point B' from specimen S3. Considering that the experimentally determined quasi-elastic limit is at a force level of 0.55 F_p, a total of 20 interpolated points are selected between 0.50 F_p to 0.80F_p, as indicated by the red circles Figure 9 (a). The corresponding values of stress and strain based on equation (17) and (18) are given in Figure 9 (b). The equi-biaxial strain at the end of hardening ε_{Utu} corresponding to the calculated equi-biaxial tensile strength (f_{Utu} = 14.24 MPa) is determined to be 1.62‰.
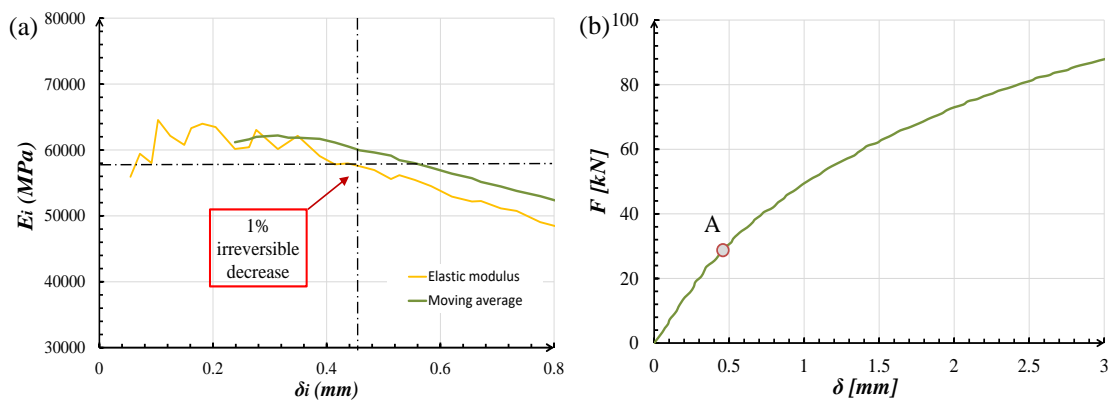
Figure 8 Example of determination of elastic limit:
(a) elastic modulus as a function of deflection; (b) position of elastic limit
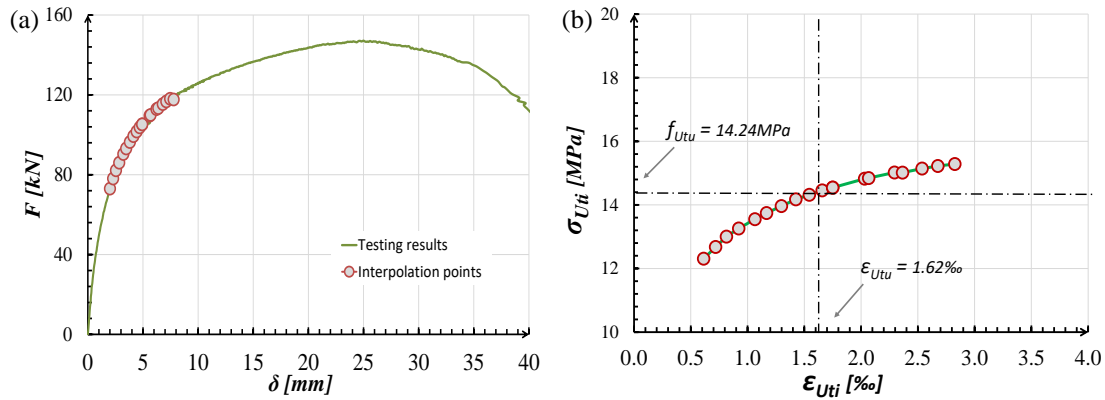
Figure 9 Example of determination of damage localization point:
(a) test results with interpolated points; (b) corresponding tensile properties

Finally, all results from inverse analyses of the ring-on-ring tests are summarized in Table 2, where $F_{A'}$ and $F_{B'}$ refer to the force at elastic limit and at damage localization point as determined using the proposed inverse analysis method. In general, the equi-biaxial tensile properties are consistent within the four slab specimens, although a relatively low value of ε_{Utu} is observed for S4. The equi-biaxial elastic modulus is 59'000 MPa in average. It is noted that the determined elastic limit (point A') agrees well with the experimental result (point A), where the first matrix discontinuity is observed from DIC analysis. Value $F_{B'}$, corresponding to 0.63 F_p in average, is around 16% higher than the quasi-elastic limit (point B, F_{qe}) as determined experimentally. For direct comparison, the position of point B' is marked in Figure 7 for S3. The corresponding DIC strain contours at points B and B' are given in Figure 10 for each UHPFRC slab specimen. It is observed that at point B, a network of matrix discontinuities is formed in the central tensile area of the slab. Afterward, this network resists cooperatively the increasing load, although slight strain concentration (red lines in the DIC strain contours) is observed. Beyond point B', the strain concentrates largely and locally to form several fictitious cracks. Therefore, point B' as determined from inverse analysis matches well with the damage localization point as obtained from experiments.

Table 2 Equi-biaxial tensile properties from inverse analysis of ring-on-ring test

No.	E_U	$F_{A'}$	f_{Ute}	$F_{B'}$	ε_{Utu}	f_{Utu}
	[MPa]	[kN]	[MPa]	[kN]	[‰]	[MPa]
S1	57'700	25.90 $(0.18F_p)$	8.31	89.52 $(0.64F_p)$	1.23	13.67
S2	56'000	31.27 $(0.20F_p)$	9.46	98.03 $(0.64F_p)$	1.28	14.07
S3	57'500	28.77 $(0.20F_p)$	9.17	96.75 $(0.66F_p)$	1.62	14.24
S4	64'500	30.55 $(0.26F_p)$	9.62	76.05 $(0.61F_p)$	0.94	14.35
Average	59'000	29.12 $(0.21F_p)$	9.14	90.09 $(0.63F_p)$	1.27	14.08
Std. dev.	3793	-	0.58	-	0.28	0.30
CV	0.06	-	0.06	-	0.22	0.02
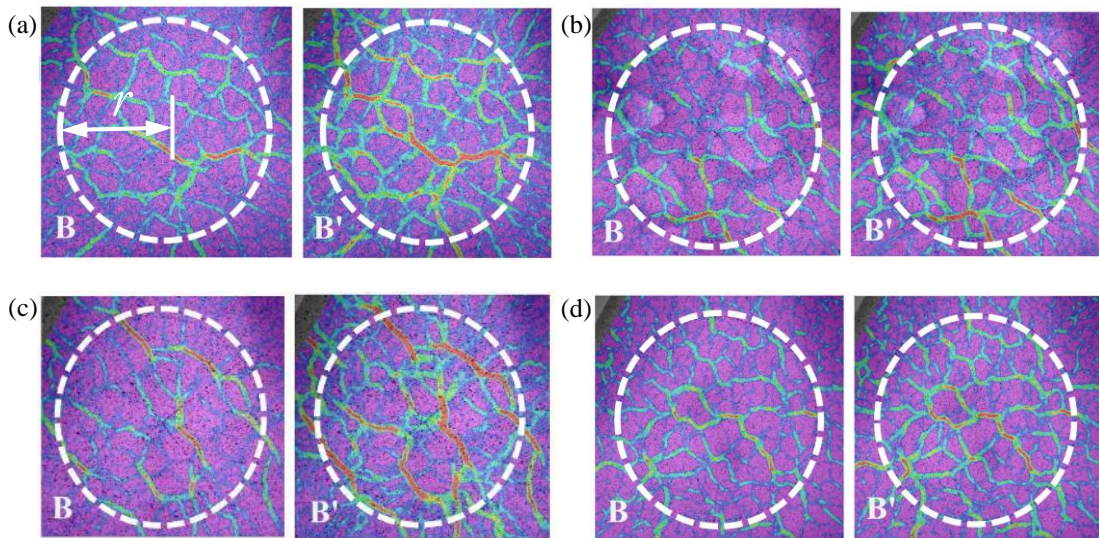
Figure 10 Comparison between quasi-elastic limit (B) and fictitious crack localization point (B') of slabs: (a) S1; (b) S2; (C) S3; (D) S4

3.3 Inverse analysis results from 4PBT

3.3.1 Experimental results

The force-deflection curves from different UHPFRC plates under 4PBT are shown in Figure 11, where a four-domain response can be identified. Based on DIC analysis, Figure 12 shows the fracture process observed from plate B1 as representative example, in which the damage propagation on the bottom surface of the constant moment zone (between loading points) are presented.

The determination of corresponding uniaxial flexural parameters is based on the same methodology as for the ring-on-ring tests. In general, the flexural responses from different plates agree well until reaching the quasi-elastic limit, and afterward, varying largely in terms of force-deflection curve and cracking pattern with increase of deflection.

Table 3 Uniaxial flexural parameters and uniaxial tensile properties from 4PBT

No.	h	F_e	F_{qe}	w_{qe}	F_p	w_p	E_U	$F_{A'}$	f_{Ute}	$F_{B'}$	ε_{Utu}	f_{Utu}
	(mm)	*[kN]*	*[kN]*	*[mm]*	*[kN]*	*[mm]*	*[MPa]*	*[kN]*	*[MPa]*	*[kN]*	*[‰]*	*[MPa]*
B1	51.80	6.12 (0.30 F_p)	14.82 (0.73 F_p)	0.031	20.42	0.07	48'750	6.61 (0.30F_p)	10.35	19.27 (0.87F_p)	3.10	13.16
B2	52.53	6.40 (0.28 F_p)	16.41 (0.73 F_p)	0.029	22.47	0.06	46'000	7.19 (0.29F_p)	10.94	23.23 (0.94F_p)	6.20	14.49
B3	53.30	6.15 (0.31 F_p)	14.36 (0.71 F_p)	0.039	20.15	0.12	47'380	6.67 (0.29F_p)	9.86	21.16 (0.92F_p)	4.90	12.97
B4	53.77	6.19 (0.35 F_p)	12.72 (0.72 F_p)	0.035	17.70	0.18	46'100	7.81 (0.38F_p)	11.35	16.08 (0.78F_p)	1.50	11.43
B6	53.83	7.10 (0.36 F_p)	12.98 (0.66 F_p)	0.025	19.52	0.20	47'000	7.02 (0.31F_p)	10.18	20.07 (0.89F_p)	3.40	12.56
B7	53.61	6.71 (0.29 F_p)	16.34 (0.71 F_p)	0.040	23.16	- [a]	47'760	7.63 (0.29F_p)	11.15	24.28 (0.92F_p)	5.00	14.94
B8	53.07	6.70 (0.31 F_p)	14.94 (0.69 F_p)	0.041	21.57	0.12	46'180	7.31 (0.30F_p)	10.90	22.29 (0.91F_p)	4.70	13.91
B9	52.47	7.79 (0.30 F_p)	17.00 (0.66 F_p)	0.036	25.70	0.20	47'540	8.02 (0.28F_p)	12.23	26.70 (0.93F_p)	7.30	16.56
B10	51.90	7.61 (0.31 F_p)	16.38 (0.66 F_p)	0.025	24.69	0.13	51'000	8.67 (0.33F_p)	13.52	24.10 (0.92F_p)	4.40	15.90
Average	52.92	6.75 (0.31 F_p)	15.11 (0.70 F_p)	0.033	21.71	0.13	47'523	7.44 (0.31F_p)	11.16	21.90 (0.90F_p)	4.50	13.99

[a] Crack localizes out of the DIC measurement zone;

[b] B5 with strain-softening behavior is not considered in this study.
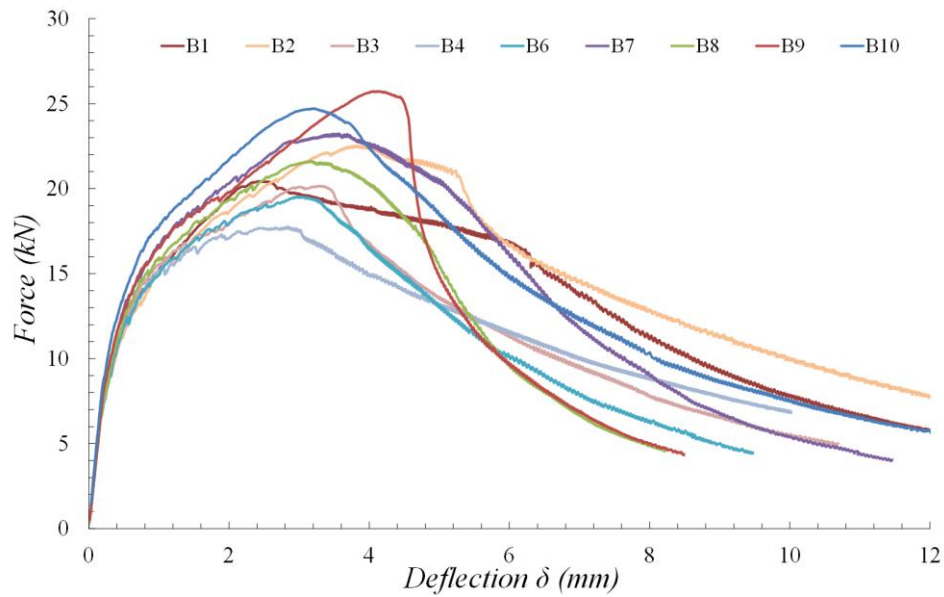
Figure 11 Force-deflection responses from 4PBT
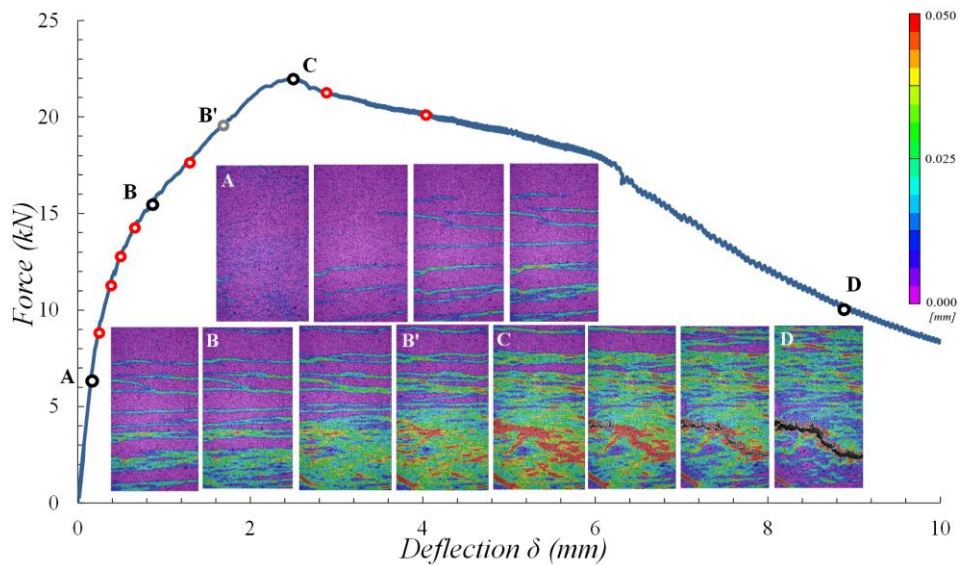
Figure 12 Example of fracture process of UHPFRC plate under 4PBT (B1)

3.3.2 Uniaxial tensile properties from 4PBT

The inverse analysis is conducted individually based on the force-deflection response of each specimen under 4PBT condition, following the method proposed by Denarié et al. [11]. The inverse analysis results of 4PBT are summarized in Table 3. A considerable variation of uniaxial tensile properties, especially the uniaxial strain at the end of hardening, is observed. This is

attributed to the large variation of fiber distribution in the slab where 4PBT specimens were extracted, as also reported in [1,12,13,39].

Similar with the findings from the inverse analysis of the ring-on-ring test results (section 3.2), point A' corresponds well to the elastic limit, where the first matrix discontinuity exists. Point B' represents the initiation of large damage concentration on single fictitious crack, as illustrated in Figure 12 as an example.

4. Discussion

Based on the inverse analysis results obtained from the ring-on-ring test and 4PBT, the equi-biaxial and uniaxial tensile properties (in average) of strain-hardening UHPFRC are compared. It is found that under equi-biaxial stresses, the average elastic modulus is 59'000 MPa, approximately 24% higher than the one obtained under uniaxial stress, while the equi-biaxial elastic limit stress (9.14 MPa) is 18% smaller than the uniaxial elastic limit stress (11.16 MPa) in average. This may be attributed to the fact that a large zone of the UHPFRC slab specimen in ring-on-ring test configuration is under pure bending in all directions, while a relatively small zone of the rectangular plate in 4PBT is under pure bending in only one direction. Thus, it is plausible that the formation of first matrix discontinuity occurs at lower stress in the ring-on-ring test, given the stochastic nature and inherent variability of fiber distribution in the UHPFRC material. On the other hand, the relatively high value of equi-biaxial elastic limit may be explained by the confinement effect due to multiple axial tension under ring-on-ring testing. The same effect was reported by Swanepoe [14] for SHCC under biaxial DTT.

As for the damage localization point B' where the fictitious cracks start to propagate significantly, the corresponding force $F_{B'}$ represents 90% of the flexural resistance (0.90 F_p) under 4PBT condition. This is slightly lower than values ($F_{B'} \geq 0.95 F_p$) reported in the literature [21,25], in which different strain-hardening UHPFRC mixes and specimen sizes were used. However, in the study of López et al. [21], point B' was proposed empirically without experimental validation. In the study of Baby et al. [25], a pair of staggered LVDTs were installed on the tensile surface of the specimen, and the point B' was identified at the bifurcation of deformation measurements from the two LVDTs. However, the result depends largely on the measuring length and position of LVDTs, given that the matrix discontinuities before point B' are not distributed uniformly but are concentrated in specific zones in the constant moment length, as illustrated in Figure 12. This implies that the apparent bifurcation is not determined accurately, leading to an overestimation of strain at the end of hardening [11]. The full-field strain measurements using the DIC technique in the present study allow to determine point B' with high accuracy.

On the other hand, point B' from the ring-on-ring test corresponds to 0.63 F_p, which is much lower than the corresponding values obtained from the 4PBT. This is explained by the significant stress distribution since complex cracking pattern with large crack surfaces are observed (Figure 7) beyond point B' under the ring-on-ring test configuration, resulting in a considerable increase of the flexural resistance. Besides, the analytical equi-biaxial strain at the end of hardening is 1.27‰,

while the uniaxial strain is as high as 4.50‰. This large difference can also be observed visually at point B' from Figure 7 and Figure 10 for the ring-on-ring test and Figure 12 for 4PBT, where more compact distribution and higher amount of matrix discontinues per unit surface are detected on the tensile surface for the 4PBT. This may be explained by inhomogeneous fiber distribution in one specific direction of the UHPFRC slab, where damage localizes early and the restrains further development of matrix discontinuities over the remaining part of the slab. Similar experimental results were reported in [20] using biaxial DTT, in which the biaxial strain at the end of hardening was determined to be 0.17‰, while the uniaxial strain was 0.25‰ for the same type of UHPFRC. Conversely, the equi-biaxial tensile strength (14.08 MPa) is almost equivalent to the uniaxial tensile strength (13.99 MPa).

5. Conclusion

An original analytical inverse analysis method for determining the equi-biaxial tensile properties of strain-hardening UHPFRC from the ring-on-ring test is proposed based on elastic slab bending and yield line theories. The inverse analysis results are validated against experimental evidence obtained from DIC analysis. Moreover, the uniaxial tensile properties of the same UHPFRC are obtained from the inverse analysis of 4PBT, following the method proposed in [11]. Uniaxial and equi-biaxial tensile properties of strain-hardening UHPFRC are then compared.

The main conclusions are:

(1) The proposed inverse analysis offers a simple method to determine the equi-biaxial tensile properties of strain-hardening UHPFRC based on the experimental force-deflection curves from the ring-on-ring test. The method does not require extensive iterative procedures and can be implemented in a ready-to-use spreadsheet.

(2) The determination of elastic limit based on the criterion of 1% irreversible reduction of the moving average of the secant elastic modulus is proven to be objective, as validated experimentally based on DIC analysis. The corresponding equi-biaxial elastic limit stress (9.14 MPa) is 18% smaller than the uniaxial elastic limit stress (11.16 MPa); while the equi-biaxial elastic modulus (59' 000MPa) is 24% higher than that under uniaxial stress

(3) The damage localization point corresponds to 63% of flexural maximum resistance under the ring-on-ring testing condition, while 90% under 4PBT condition. The corresponding equi-biaxial strain at the end of hardening is 1.27‰, which is only 28% of the uniaxial strain. This difference can also be observed visually on the DIC strain contours at point B', where more compact distribution and higher amount of matrix discontinues per unit surface are detected on the tensile surface for 4PBT, compared with the corresponding findings from the ring-on-ring test.

(4) The equi-biaxial tensile strength (14.08 MPa) is almost equivalent to the uniaxial tensile strength of cut-out of larger plates 4PBT strips (13.99 MPa) as determined by invers analysis.

6. References

[1]   C. Oesterlee, Structural response of reinforced UHPFRC and RC composite members (doctoral thesis, 4848), École polytechnique fédérale de Lausanne (EPFL), 2010.

[2]   T. Makita, E. Brühwiler, Tensile fatigue behaviour of ultra-high performance fibre reinforced concrete (UHPFRC), Mater Struct. 47 (2014) 475–491.

[3]   M. Bastien-Masse, E. Brühwiler, Experimental investigation on punching resistance of R-UHPFRC–RC composite slabs, Materials and Structures. 49 (2016) 1573–1590.

[4]   E. Brühwiler, "Structural UHPFRC" to enhance bridges, in: Keynote Lecture, 2nd International Conference on UHPC Materials and Structures (UHPC 2018 - China), Fuzhou, China, 2018: pp. 140–158.

[5]   E. Denarié, E. Brühwiler, Cast-on site UHPFRC for improvement of existing structures–achievements over the last 10 years in practice and research, in: 7th Workshop on High Performance Fiber Reinforced Cement Composites, 1-3, June 2015, Stuttgart, Germany, 2015.

[6]   T. Guenet, F. Baby, P. Marchand, L. Sorelli, S. Bernardi, F. Toutlemonde, Flexural failure modes and ductility assessment of ribbed triangular UHPFRC plates, in: HiPerMat 2016-4th International Symposium on Ultra-High Performance Concrete and High Performance Construction Materials, 2016: p. 9p.

[7]   A. Spasojevic, Structural implications of ultra-high performance fibre-reinforced concrete in bridge design, École polytechnique fédérale de Lausanne (EPFL), 2008.

[8]   X. Shao, L. Deng, J. Cao, Innovative steel-UHPC composite bridge girders for long-span bridges, Front. Struct. Civ. Eng. 13 (2019) 981–989.

[9]   Voo Yen Lei, Foster Stephen J., Voo Chen Cheong, Ultrahigh-Performance Concrete Segmental Bridge Technology: Toward Sustainable Bridge Construction, Journal of Bridge Engineering. 20 (2015) B5014001.

[10] J. Kim, D.J. Kim, S.H. Park, G. Zi, Investigating the flexural resistance of fiber reinforced cementitious composites under biaxial condition, Composite Structures. 122 (2015) 198–208.

[11] E. Denarié, L. Sofia, E. Brühwiler, Characterization of the tensile response of strain hardening UHPFRC - Chillon Viaducts, AFGC-ACI-Fib-RILEM Int. Symposium on Ultra-High Performance Fibre-Reinforced Concrete, UHPFRC 2017. (2017).

[12] M. Bastien-Masse, E. Denarié, E. Brühwiler, Effect of fiber orientation on the in-plane tensile response of UHPFRC reinforcement layers, Cement and Concrete Composites. 67 (2016) 111–125.

[13] X. Shen, E. Brühwiler, Influence of local fiber distribution on tensile behavior of strain hardening UHPFRC using NDT and DIC, Cement and Concrete Research. 132 (2020) 106042.

[14] W. Swanepoel, The behaviour of fibre reinforced concrete (SHCC) under biaxial compression and tension, Stellenbosch: Stellenbosch University, 2011.

[15] D.-Y. Yoo, G. Zi, S.-T. Kang, Y.-S. Yoon, Biaxial flexural behavior of ultra-high-performance fiber-reinforced concrete with different fiber lengths and placement methods, Cement and Concrete Composites. 63 (2015) 51–66.

[16] B.A. Graybeal, F. Baby, Development of Direct Tension Test Method for Ultra-High-Performance Fiber-Reinforced Concrete., ACI Materials Journal. 110 (2013) 177–186.

[17] X. Shen, E. Brühwiler, Characterization of Tensile Beahvior in UHPFRC Thin Slab Using NDT Method and DIC System, in: Proceedings PRO 129, Fuzhou, China, 2018.

[18] T. Kanakubo, Tensile Characteristics Evaluation Method for Ductile Fiber-Reinforced Cementitious Composites, ACT. 4 (2006) 3–17.

[19] K. Wille, S. El-Tawil, A.E. Naaman, Properties of strain hardening ultra high performance fiber reinforced concrete (UHP-FRC) under direct tensile loading, Cement and Concrete Composites. 48 (2014) 53–66.

[20] O. Ple, E. Astudillo de al Vega, G. Bernier, O. Bayard, Biaxial tensile behavior of the reactive powder concrete, in: Cancun, Mexico, 2002: pp. 369–387. https://trid.trb.org/view.aspx?id=704544.

[21] J.Á. López, P. Serna, J. Navarro-Gregori, H. Coll, A simplified five-point inverse analysis method to determine the tensile properties of UHPFRC from unnotched four-point bending tests, Composites Part B: Engineering. 91 (2016) 189–204.

[22] J.Á. López, P. Serna, J. Navarro-Gregori, E. Camacho, An inverse analysis method based on deflection to curvature transformation to determine the tensile properties of UHPFRC, Mater Struct. 48 (2015) 3703–3718.

[23] SAMARIS D26, Modelling of UHPFRC in composite structures, European project 5th FWP / SAMARIS – Sustainable and Advanced MAterials for Road Infrastructures – WP 14: HPFRCC, http://samaris.zag.si/, 2006.

[24] F. Baby, B. Graybeal, P. Marchand, F. Toutlemonde, UHPFRC tensile behavior characterization: inverse analysis of four-point bending test results, Mater Struct. 46 (2013) 1337–1354.

[25] F. Baby, B. Graybeal, P. Marchand, F. Toutlemonde, Proposed flexural test method and associated inverse analysis for ultra-high-performance fiber-reinforced concrete, ACI Materials Journal. 109 (2012) 545.

[26] Technical Leaflet SIA 2052 UHPFRC – Materials, design and construction, SIA (Swiss Society of Engineers and Archtitects) Zurich Switzerland, 2016.

[27] N. AFNOR, P18-710: National addition to Eurocode 2–Design of concrete structures: Specific rules for ultra-high performance fiber-reinforced concrete (UHPFRC), Association Française de Normalisation, 2016.

[28] P. Marti, T. Pfyl, V. Sigrist, T. Ulaga, Harmonized Test Procedures for Steel Fiber-Reinforced Concrete, MJ. 96 (1999) 676–685.

[29] Recommendation SIA 162/6 Steel fibre reinforced concrete, SIA (Swiss Society of Engineers and Archtitects) Zurich Switzerland, 1999.

[30] E. Cadoni, T. Teruzzi, A. Muttoni, R. Suter, E. Brühwiler, FRC in Switzerland: research, applications and perspectives, in: International Workshop on Advanced Fiber Reinforced Concrete, International Workshop on Advanced Fiber Reinforced Concrete, 2004.

[31] C. ASTM, 1499-05. Standard test method for monotonic equibiaxial flexural strength of advanced ceramics at ambient temperature, ASTM International, West Conshohocken, Pennsylvania. (2009).

[32] X. Shen, E. Brühwiler, Flexural quasi-static behavior of UHPFRC circular slab specimens, AFGC-ACI-Fib-RILEM Int. Symposium on Ultra-High Performance Fibre-Reinforced Concrete, UHPFRC 2017. (2017).

[33] S. Timoshenko, S. Woinowsky-Krieger, Theory of plates and shells, (1959).

[34] D.-Y. Yoo, N. Banthia, G. Zi, Y.-S. Yoon, Comparative Biaxial Flexural Behavior of Ultra-High-Performance Fiber-Reinforced Concrete Panels Using Two Different Test and Placement Methods, Journal of Testing and Evaluation. 45 (2017) 624–641.

[35] M.A. Baril, L. Sorelli, J. Réthoré, F. Baby, F. Toutlemonde, L. Ferrara, S. Bernardi, M. Fafard, Effect of casting flow defects on the crack propagation in UHPFRC thin slabs by means of stereovision Digital Image Correlation, Construction and Building Materials. 129 (2016) 182–192.

[36] L. Moreillon, J. Nseir, R. Suter, Shear and flexural strength of thin UHPC slabs, in: Proceedings of Hipermat, 2012: pp. 748–756.

[37] K.W. Johansen, Yield-line theory, Cement and Concrete Association, 1962.

[38] R. Park, W.L. Gamble, Reinforced concrete slabs, John Wiley & Sons, 1999.

[39] L.F.M. Duque, B. Graybeal, Fiber orientation distribution and tensile mechanical response in UHPFRC, Mater Struct. 50 (2017) 1–17.

Paper IV

Biaxial Flexural Fatigue Behavior of Strain-Hardening UHPFRC Thin Slab Elements

ABSTRACT

The biaxial flexural fatigue behavior of circular slab elements made of strain-hardening Ultra High Performance Fiber Reinforced Cementitious Composite (UHPFRC) is investigated experimentally by means of the ring-on-ring test method. Fourteen flexural fatigue tests under constant amplitude fatigue cycles up to the Very High Cycle Fatigue domain (20 million cycles) are conducted with varying maximum fatigue stress level S ranging from 0.50 to 0.68. Digital Image Correlation (DIC) technology is applied to capture the 3D full-field strain contours on the tensile surface through the entire fatigue test. Test results presented in the S-N diagram reveal a fatigue endurance limit under biaxial flexural fatigue at S=0.54. Fatigue tests exhibiting failure show four distinct phases of damage evolution, while only the first two phases are observed in the case of run-out tests. DIC analysis reveal formation and propagation of multiple fine fictitious cracks that dominate the stable fatigue propagation phase with slow rate, representing the longest part of fatigue life of the UHPFRC specimen. Finally, the secant modulus of deflection and fictitious crack opening with respect to fatigue cycles is found to characterize quantitatively fatigue damage evolution.

1. Introduction

Tensile strain-hardening Ultra-High Performance Fiber Reinforced Cementitious Composites (UHPFRC) possess extremely low permeability, relatively high strength (compressive strength ≥ 180MPa, tensile strength ≥ 10MPa). A notable feature of UHPFRC subjected to uniaxial tension is the significant deformation capacity including hardening strain up to 5‰, where only matrix discontinuities in the bulk matrix are observed before reaching the tensile strength. Afterward, the pronounced softening behavior is characterized by the formation of one fictitious crack with major fracture energy dissipation, as illustrated in Figure 1 for uniaxial tensile response. Regarding the fatigue behavior of UHPFRC, a fatigue endurance limit up to multimillion cycles exists under uniaxial tensile or flexural fatigue [1–5]. These characteristics make UHPFRC fundamentally different from high performance concrete or fiber reinforced concrete, and suitable for the application on fatigue sensitive structural components [6,7].
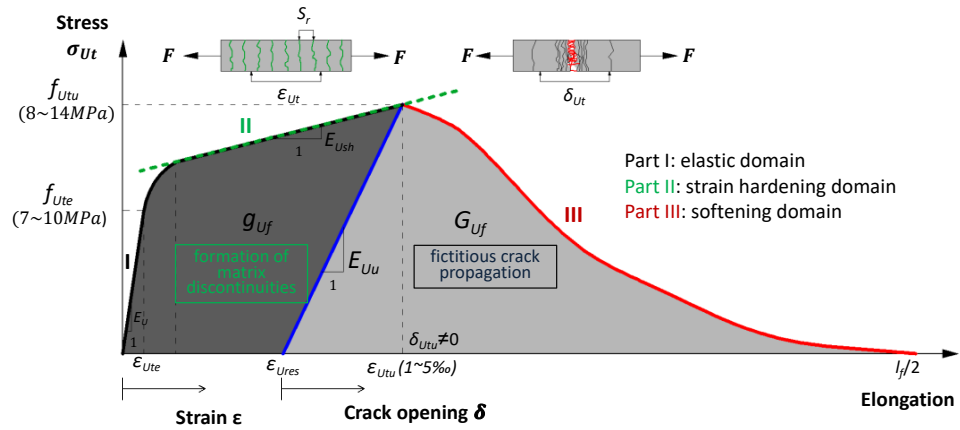
Figure 1 Schematic representation of tensile response of strain-hardening UHPFRC (not in scale)

Application of UHPFRC to specific zones of structural members subjected to severe mechanical and environmental actions, such as bridge deck slabs, has been proven to be an effective method to improve (strengthen) structural members with respect to resistance and durability. The original concept is placing a relatively thin UHPFRC layer (with typical thickness of 50mm) on the top surface of the reinforced concrete (RC) after preparation of the substrate surface by water jetting [6,8].

In the case of bridges, deck slabs are the most fatigue loaded structural elements. The actual stress state caused by wheel loading is nearly equi-biaxial and far from being uniaxial [9]. And during the service duration (of more than 100 years), bridge decks are expected to be subjected to a high number of repetitive loading, which may exceed several hundred million [10]. In this context, comprehensive understanding of the fatigue behavior of bridge deck slabs under biaxial conditions and Very High Cycle Fatigue (VHCF) is essential in the fatigue design of UHPFRC strengthening of existing RC bridge deck slabs and of deck slabs of new UHPFRC bridges.

As summarized in Table 1, only few experimental studies have been conducted on the fatigue behavior of strain-hardening UHPFRC by means of either uniaxial direct tensile test (DTT)

or bending tests, in which UHPFRC shows fatigue endurance limit at a certain number of loading cycles [1–5]. An empirical determination of the fatigue endurance limit is introduced in UHPFRC design codes like SIA 2052 [11] and NF P18-710 [12].

Makita et al. [1] carried out three series of fatigue tests using specimens subjected to different initial loading conditions, including specimens with preloading into the elastic domain, the strain hardening domain and the softening domain of UHPFRC, respectively. Different fatigue endurance limits were obtained for all three domains in direct tension after 10 million cycles. Significant redistribution of local deformation and stress due to strain-hardening behavior in the UHPFRC bulk material was observed in all test series. This redistribution capacity enhanced the fatigue behavior. Smooth fatigue crack surface, analogous to the one known from steel, was observed for UHPFRC specimens showing fatigue failure.

Furthermore, the fatigue endurance limit of UHPFRC strengthened with steel reinforcement bars (hereafter called R-UHPFRC) was determined to be at 54% of the resistance of direct tension test (DTT) specimens, suggesting that the UHPFRC fatigue behavior was in the strain-hardening domain [2]. This phenomena can be attributed to the significant strain hardening capacity of UHPFRC and pronounced stress redistribution from UHPFRC to the steel reinforcement bars, when compared with plain UHPFRC tested by DTT [7].

In the case of bending tests, Parant et al. [3] determined a fatigue endurance limit at 65% of the equivalent flexural tensile strength (corresponding to maximum tensile strains of 1.27‰) after 2 million fatigue cycles for a specific UHPFRC subjected to 4-Point-Bending-Testing (4PBT). It should be noted that at this fatigue stress, only part of the specimen cross section under bending is in the strain hardening domain. Similar findings were reported in the study by Farhat et al. [5], in which the fatigue endurance limit was determined to be at 85% of the flexural strength of small beam specimens subjected to 3-Point-Bending-Testing (3PBT) up to 1 million cycles.

Similar to fatigue damage process known for other materials, Rossi et al. [13] characterized the fatigue damage evolution of UHPFRC under 4PBT into three stages in terms of deflection and openings, namely (1) the micro-cracking stage with rapid increase of deflection and strain, (2) the stable stage with slow and linear increase of deflection, and (3) unstable stage to failure.

Given that actual UHPFRC structural elements often are subjected to flexural tension instead of pure tension, the fatigue bending test may better characterize the tensile fatigue behavior of UHPFRC in structures. In addition, considering that the strain-hardening behavior is more pronounced in the tensile zone of bending specimens than in pure tension specimens [14], the stress and deformation redistribution capacity of strain-hardening UHPFRC may be underestimated. Consequently, the fatigue resistance of UHPFRC may be underestimated when characterized using the DTT.

Large variation of values describing the fatigue endurance limit of UHPFRC is reported in the literature, and the applied number of loading cycles was often limited to only 2 million (Table 1). Thus, there is a need to validate the fatigue endurance limit for Very High Fatigue Cycles (VHFC) domain (N $\geq$ 10×10^6). Additionally, to the best of the authors' knowledge, no extensive research was conducted to investigate the development of strain hardening response of UHPFRC under fatigue loading, although it is of utmost importance to understand the

fatigue behavior of this material. Additionally, the biaxial flexural fatigue behavior of UHPFRC has not yet been studied.

The fatigue strength is generally represented in the *S-N* diagram with the maximum relative stress level *S* as a function of the number *N* of fatigue cycles until failure, presented using a logarithmic scale. In the case of fatigue in bending, *S* denotes the ratio between the maximum fatigue stress and the flexural strength as obtained from the quasi-static testing. The dimensionless term *S* can effectively eliminate differences in loading configuration, material properties and testing conditions, as reported by various experimental campaigns [15].

To the best of the authors' knowledge, UHPFRC standards do not provide *S-N* curves because of limited available fatigue test data. Besides, a critical issue in evaluating fatigue test results based on *S-N* curves is the relatively large scatter of data, as reported in [1,5,16]. This is mainly attributed to the scatter of the UHPFRC's tensile strength resulting from rather large fiber distribution [17–19]. Consequently, the maximum stress level *S* in each test cannot be exactly determined when the average tensile strength from previous quasi-static testing is used as a reference. Therefore, consistent and rigorous specimen preparation and testing procedure should be carefully conducted in fatigue testing of UHPFRC.

Recently, the ring-on-ring test similar to the one used to characterize ceramics and glass according to ASTM C. 1499-05 [20], has been applied successfully to investigate the biaxial flexural behavior of UHPFRC [21,22]. A circular slab specimen is simply supported on a ring support and the external loading is uniformly distributed on a central loading ring from the top. Thus, the central part of the specimen is in pure bending condition, produced by a uniformly distributed moment according to elastic slab bending theory [23]. Consistent test results reported in [21,22] validate the ring-on-ring test as being suitable for fatigue testing.

This paper investigates experimentally the biaxial flexural fatigue behavior of circular slab elements made of strain-hardening UHPFRC, using the ring-on-ring test method. Fourteen biaxial flexural fatigue tests under constant amplitude fatigue cycles up to 20 million cycles are conducted with varying *S* (stress level being the ratio between the maximum fatigue load and the quasi-static flexural resistance of the slab specimen) ranging from 0.50 to 0.68 in order to determine the fatigue behavior of UHPFRC at VHFC in terms of *S-N* curve and fatigue damage evolution due to biaxial flexural fatigue. The fatigue fracture process, particularly the formation and development of matrix discontinuities and fictitious cracks, are analyzed based on digital image correlation (DIC) analysis.

Table 1 Review of fatigue flexural/tensile testing results of strain hardening UHPFRC

Ref.	UHPFRC Type	V_f [%]	f_{Ute} MPa	f_{Utu} MPa	ε_{Utu} ‰	Specimen state before test	Method	$\sigma_{fat,max}$ ($\varepsilon_{fat,max}$)	$\sigma_{fat,min}$	Cycles up to	Endurance limit
Makita et al. [1]	HIFCOM 13	3.0	8.2	9.40	1.64	Without preload	DTT	0.20‰, 0.25‰, 0.30‰	0.1f_{ute}	10 million	0.70f_{ute} (0.61f_{utu})
						Preload into strain-hardening domain		0.10‰, 0.15‰, 0.20‰	0.1$\sigma_{fat,max}$		0.60f_{ute} (0.52f_{utu})
						Preload into softening domain		0.20‰	0.1$\sigma_{fat,max}$		0.45f_{ute} (0.39f_{utu})
Parrant et al. [3]	CEMTEC$_{multiscale}$®	11.0	-	23.48	-	Without preload	4PBT	0.58~0.80 f_{ubu}	0.1$\sigma_{fat,max}$	2 million	0.65f_{ubu}
Chanvillard et al. [4]	Ductal®	2.0	-	-	-	Preload to 0.3mm crack opening	3PBT	0.9f_{ube}	0.1f_{ube}	1 million	0.54f_{utu}
Farhat et al. [5]	CARDIFRC	6.0	9.2	12.89	0.60	Without preload	3PBT	0.80~0.90 f_{ubu}	0.1f_{ubu}	1 million	0.85f_{ubu}
Makita et al. [2]	HIFCOM 13	3.0	8.2	9.40	1.64	Reinforced with steel rebars Without preload	DTT	1.0‰, 1.5‰	0.1$\sigma_{fat,max}$	10 million	0.54f_{utu}

$\sigma_{fat,max}$ and $\sigma_{fat,min}$: imposed maximum and minimum fatigue load

$\varepsilon_{fat,max}$: imposed maximum strain at the initial quasi-static loading to determine $\sigma_{fat,max}$

f_{Ute}: tensile elastic limit based on DTT

f_{Utu}: tensile strength based on DTT

f_{Ube}: flexural elastic limit based on bending test

f_{Ubu}: flexural strength based on bending test

2. Experimental investigation

2.1 Material and specimen preparation

The tested strain-hardening UHPFRC is an industrial premix containing 3.8% by volume of straight steel fibers with length of 13mm and diameter of 0.175mm, and its water to cement ratio is 0.15 (Table 2). At 28 days, the UHPFRC has an average elastic modulus of 49GPa and compressive strength of 185MPa, measured on cylinders of 70mm diameter.

Table 2 Composition of UHPFRC

Components		Quantity
Premix (cement. Additions, quartz sand)		1970
Water	kg/m^3	175
Specific superplasticizer		29
Steel fibers ($l_f/d_f = 13/0.175, V_f = 3.8\%$)		298.3

The circular slab element, with a radius $R_0=600mm$ and a thickness $h=50mm$, is used as test specimen in the present experimental campaign. During casting, the fresh self-compacting UHPFRC (with a slump flow of 700mm) was poured on the center area of the formwork from where it had flown (without any pulling or vibration) to fill entirely the formwork. Afterward, a plastic sheet was pulled over the elements to allow for curing. The formworks were removed 24 hours later. The slab elements were then kept under moist curing conditions at 20℃ and 100% humidity during the following seven days, and subsequently were stored inside the laboratory until testing. The age at testing was more than 90 days when over 90% of the UHPFRC final material properties were attained [24,25].

2.2 Test method

The ring-on-ring test is performed to investigate the biaxial flexural fatigue behavior of UHPFRC slabs. Figure 2 shows the full test set-up and instrumentation applied in this experimental campaign. The slab is simply supported on a steel support ring with $R=500mm$ and width of 50mm, and the force from a hydraulic jack acts on the center of slab through a steel force transmitting ring with $r=150mm$ and width of $30mm$. Thus, uniform tensile stress is introduced on the bottom surface of the slab within the force transmitting ring area, where biaxial stress condition may be assumed.

Before testing, the actual thickness of each UHPFRC slab is measured using Faro Arm (3D measuring arm device) [26]. The slabs are tested with the casting surface facing upwards, allowing the observation of tensile damage propagation on the smooth sheathed surface. Before testing, the casting surface is polished and a mortar layer is placed between support ring and bottom surface to level out both surfaces. Two rubber pads (thickness of $10mm$, $E=500MPa$) are positioned between the slab surfaces and the two rings to distribute the force evenly.

As illustrated in Figure 2, Digital Image Correlation (DIC) technique [27] is applied to observe the full-field fatigue damage propagation during the whole fatigue test. Two digital cameras are placed underneath the slab at a distance of 0.5 m and an angle of 23 degrees to the vertical. The tensile surface of the slab is painted with matte white paint, followed by spraying a black speckle pattern with size less than 1 mm. The targeted area, which is visible to the DIC, is of 500mm in diameter on the slab center. In this case, the DIC measurement accuracy reached about *5με*. In addition, two series of LVDT systems are installed on the top surface to measure the central deflection of slab and deformation of rubber pad, respectively. All deflection measurements are performed with respect to the strong floor. Further details about the ring-on-ring test used in this study can be found in [22].
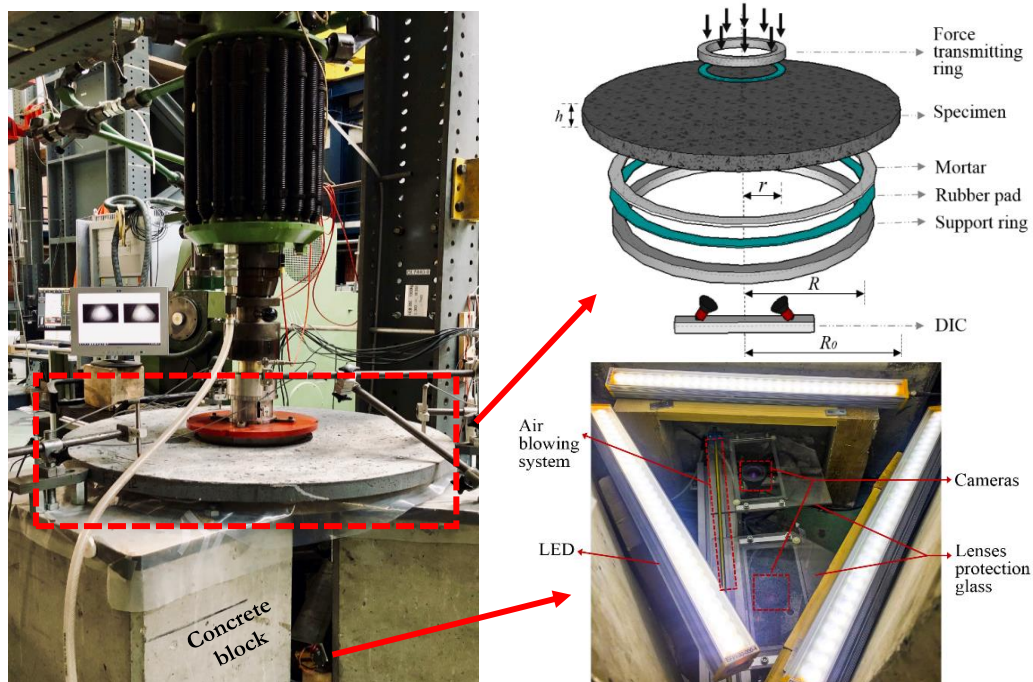
Figure 2 Schematic description of test setup

2.3 Testing program

A total of eighteen UHPFRC circular slab elements are prepared: four quasi-static tests are carried out first to characterize the biaxial flexural behavior, and fourteen fatigue tests with S ranging from 0.50 to 0.70 are performed to investigate the biaxial flexural fatigue behavior of the UHPFRC slab elements.

For the quasi-static test, monotonic loading with a displacement rate of *1.0 mm/min* was applied up to the peak force, followed by a rate of *4.0 mm/min* until the actuator displacement reached 80 mm. The recordings of the two cameras of the DIC system were synchronized via wired computer control with a frequency of 0.2 Hz, while the recording by the LVDTs was 5 Hz.

The fatigue testing procedure is described in Figure 3. First, all the specimens are subjected to three loading-unloading cycles up to 15kN with an actuator displacement rate of 1.0mm/min for loading preparation. Afterward, monotonic loading with the same displacement rate is applied up to the targeted maximum fatigue load $F_{fat,max}$ and unloaded to the corresponding minimum fatigue load $F_{fat,min}$. This quasi-static loading-unloading part aims to precisely predict the flexural resistance of each slab. Then the sinusoidal cyclic loading with constant amplitude is imposed with a frequency of 5Hz. The transition period from quasi-static to constant amplitude fatigue loading regime needs roughly 1min.

A smart DIC measurement program is developed and applied during the fatigue tests as also illustrated in Figure 3. At the early age of fatigue loading, the DIC measurement is activated at every selected number of cycles with frequency of 50Hz. Thus, enough data can be recorded to characterize the rapid first fatigue phase. Then the DIC measurement is activated at each 5'000th cycle during the second stable fatigue phase and at each 100th cycle during the final unstable fatigue phase. Additionally, continuous measurements with a frequency of *100Hz* of the actuator displacement and LVDTs are performed during the fatigue test.
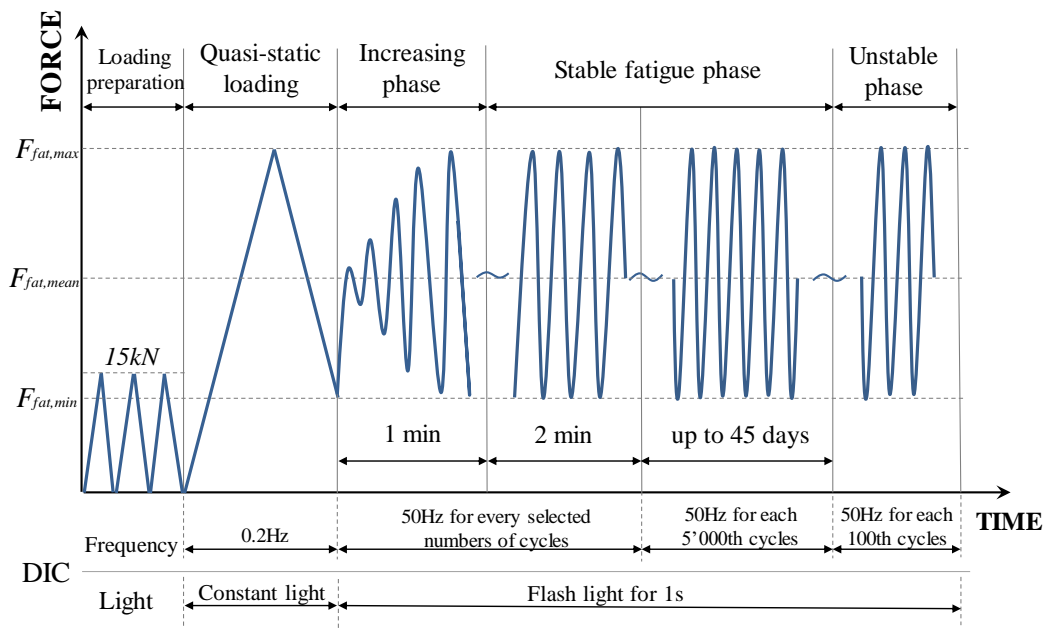
Figure 3 Qualitative fatigue loading history and DIC measurement program

In this study, the values of $F_{fat,max}$ vary between 50% and 70% of the flexural resistance of the UHPFRC slab. Considering that the self-weight causes small stress in structural slabs, the specific ratio $R=F_{fat,min}/F_{fat,max}$ is chosen as 0.1, similar to [2,3,28]. The fatigue endurance limit is defined as the stress level below which no fatigue failure occurs up to 20 million cycles. With respect to deck slabs of bridges, 20 million extreme force cycles are considered to be realistic to be reached during the service life for heavily trafficked bridges. Besides, the number of 20 million cycles belongs to

the range of the VHCF domain [2,29]. Fatigue failure is defined as the event when the imposed maximum load $F_{fat,max}$ can no longer be resisted by the specimen.

3. Experimental results

3.1 Quasi-static biaxial flexural behavior of the UHPFRC circular slab

The force versus central deflection (F-δ) curves of four UHPFRC circular slabs from the ring-on-ring test are presented in Figure 4, in which the thick curve refers to the average response. Here, the central deflection values are determined by DIC analysis on the bottom surface, excluding the deformation of rubber pad measured from three LVDTs on top surface. The recorded force values are modified considering the real thickness of each slab by using the term $(h/h_i)^2$, where h is the nominal thickness (50 mm) and h_i is the measured thickness of each slab.

As observed from the F-δ curves accompanied with DIC analysis [22], the ring-on-ring test yields consistent biaxial flexural response of the UHPFRC slabs. Four distinct domains can be distinguished, namely, the elastic domain (OA), quasi-elastic domain (AB), hardening domain (BC) and softening domain (CD), as marked with letters A-D in Figure 4. Accordingly, Table 4 summarizes the main parameters, including force, deflection and maximum opening, at the end of each domains (point A, B and C) and for all slabs. Based on the DIC strain contours, the elastic limit (corresponds to F_e and δ_e at point A) is determined when the first matrix discontinuity is detected, while the quasi-elastic limit (corresponds to F_{qe}, δ_{qe} and w_{qe} at point B) refers to the start of strain concentration on one or several matrix discontinuities, implying the initiation of fictitious cracks.

In the following, the biaxial flexural response of the UHPFRC circular slab element is described according to the four different domains shown in Figure 4:

(1) Elastic domain (Phase I, OA): A linear F-$\boldsymbol{\delta}$ response is observed, and the elastic limit is obtained when the force reaches about 20% of ultimate resistance ($0.20F_p$).

(2) Quasi-elastic domain (Phase II, AB): The UHPFRC in the most deformed tension zone shows tensile strain hardening behavior. The biaxial flexural response is thus dominated by random development of matrix discontinuities on the bottom surface mainly within the force transmitting area. At the end of this phase, a uniform network of matrix discontinuities is formed with maximum openings less than 0.1mm. The force F_{qe} at the quasi-elastic limit corresponds to 0.55 F_p in average. It should be noted that a considerable portion of the bending resistance develops with little loss of flexural stiffness, and the force-deflection curve remains almost linear in this phase.

(3) Hardening domain (Phase III, BC): UHPFRC deformation gradually increases, entering also into the tensile softening regime. Multiple fictitious cracks develop from some of the

previous matrix discontinuities and propagate. There is a very significant increase in deflection while the flexural resistance increases by about 45%.

(4) Softening domain (Phase IV, CD): At maximum force (point C), several fictitious cracks become dominant, and keep propagating radially from the center to the edge. No more new matrix discontinuities or fictitious cracks appear. The real cracks ($w≥6.5mm$) appear only at the very end of testing with large deflection of more than 40mm, exhibiting pronounced post-peak behavior of the UHPFRC slab element.
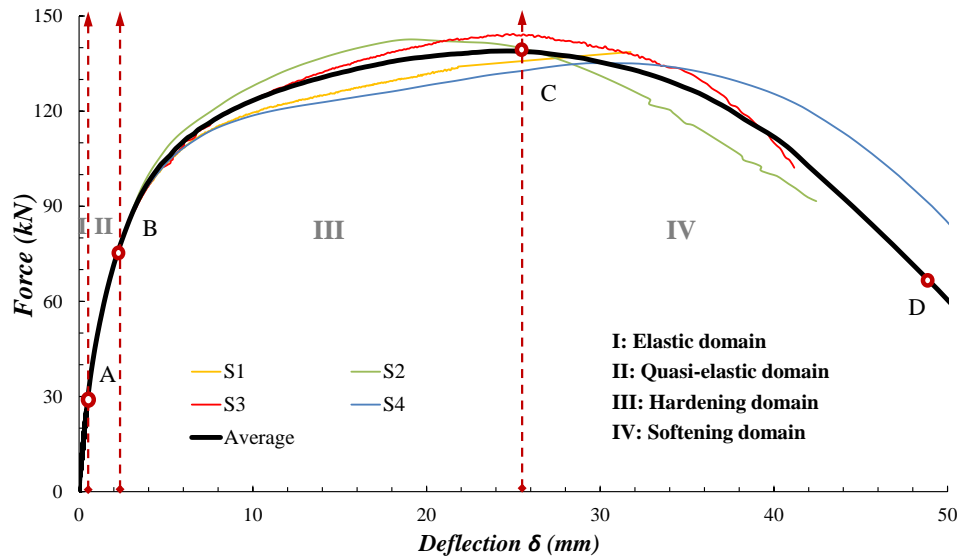
Figure 4 Force- central deflection (F-δ) curves from four quasi-static ring-on-ring tests

Table 3 Biaxial flexural parameters from the quasi-static ring-on-ring tests

No.	F_e (kN)	δ_e (mm)	F_{qe} (kN)	δ_{qe} (mm)	w_{qe} (mm)	F_P (kN)	f_{Utu} (MPa)	δ_P (mm)	w_P (mm)
S1	25.43 ($0.18F_p$)	0.40	75.15 ($0.54F_p$)	2.20	0.089	138.66	14.21	31.75	3.60
S2	28.89 ($0.20F_p$)	0.53	83.70 ($0.59F_p$)	2.65	0.087	142.64	14.62	19.06	1.70
S3	28.23 ($0.20F_p$)	0.45	74.14 ($0.51F_p$)	2.14	0.087	144.38	14.80	25.01	2.85
S4	29.40 ($0.22F_p$)	0.66	82.40 ($0.56F_p$)	2.08	0.067	146.74	13.35	29.46	4.63
Average	27.99 ($0.20F_p$)	0.51	78.85 ($0.55F_p$)	2.27	0.083	143.11	14.08	26.32	3.20
Std. dev.	1.77	0.11	4.90	0.26	0.01	3.14	0.30	5.59	1.24
CV	0.06	0.22	0.06	0.11	0.13	0.02	0.02	0.21	0.39

3.2 Biaxial flexural fatigue behavior of the UHPFRC circular slab

3.2.1 Fatigue life and S-N curves

The results of biaxial flexural fatigue tests on UHPFRC circular slab elements are summarized in Table 4 and on the S-N diagram shown in Figure 5. For F-S12, F-S13 and F-S14, the first fatigue loading was stopped before 20 million cycles because no more increase in central deflection was observed. The second fatigue loading at higher S level was applied until failure occurred. It should be noted that the ultimate flexural resistance $F_{p,cal}$ of each slab is again determined by scaling the average value from quasi-static tests using the term $(h_i/h)^2$.

From the overall test results including all run-out tests, the fatigue endurance limit of UHPFRC slabs under biaxial flexural loading is estimated to be at the S-level of 0.55, as indicated by the dashed line in Figure 5. It is noted that there is a clear gap of fatigue life (N_f) between the tests showing fatigue failure and run-out tests. The slab specimens either failed before 3.53 million cycles or sustained fatigue loading up to 20 million cycles. Moreover, based on the previous quasi-static test results (section 3.1), the force level at S=0.54 almost corresponds to the quasi-elastic limit of biaxial flexural response, where a network of matrix discontinuities is fully developed on tensile surface of the slab.

Figure 5 also shows the best fit for the linear relation between S and log(N_f) for results showing fatigue failure:

$$S = -0.0372\log(N_f) + 0.8012 \tag{1}$$

The accuracy of this relation is represented by a correlation coefficient of R^2=0.81, which is considerably higher than the ones reported in [2,3,28]. This can be attributed to the fact that in most of fatigue studies, the average value of ultimate strength (resistance) as determined from the preceding quasi-static campaign is used for calculating the fatigue stress level S. For a given specimen, the quasi-static resistance is not known, and the value of S is either higher or lower than the corresponding precise S-value of the given fatigue test specimen which cannot be known precisely. This resulted in a relatively poor correlation coefficients. In the present study, the flexural resistance of each slab is determined with the consideration of real thickness, leading to a rather reliable S value for each fatigue testing. Similar finding is reported in [30].

Table 4 Results of biaxial flexural fatigue tests on circular slab specimens

No.	h	$F_{p,cal}$	$F_{f,max}$	$F_{f,min}$	R	S	N_f	W_A	W_B	W_C	RMK
	(mm)	(kN)	(kN)	(kN)			(million)	(mm)	(mm)	(mm)	
F-S1	49.50	140.26	96.00	10.00	0.10	0.68	0.01	-	-		-
F-S2	50.50	145.99	89.00	10.00	0.11	0.61	0.26	0.12	0.51	1.29	-
F-S3	49.80	141.97	82.00	7.30	0.09	0.58	1.58	-	-	-	-
F-S4	54.00	166.92	98.00	8.00	0.08	0.59	0.25	0.13	0.55	1.75	-
F-S5	51.50	151.83	76.00	10.00	0.13	0.50	21.90	0.20	0.47	-	run-out
F-S6	55.00	173.16	112.00	10.00	0.09	0.65	0.01	-	0.83	1.45	-
F-S7	53.20	162.01	98.00	10.00	0.10	0.60	0.11	0.14	0.90	-	-
F-S8	49.50	140.26	79.00	7.00	0.09	0.56	0.43	0.19	0.67	1.30	-
F-S9	51.00	148.89	85.00	9.00	0.11	0.57	0.53	0.20	-	1.49	-
F-S10	49.00	137.44	70.74	6.00	0.08	0.51	17.57	0.18	0.49	-	run-out
			76.00	7.00	0.09	0.55	2.63	-	0.85	1.59	-
F-S11	51.00	148.89	87.50	7.00	0.08	0.59	0.88	0.15	0.63	1.46	-
F-S12	51.00	148.89	80.00	7.00	0.09	0.54	15.08	0.22	0.43	-	run-out
			85.00	7.60	0.09	0.57	3.53	-	0.79	1.23	-
F-S13	49.50	140.26	75.00	7.20	0.10	0.53	20.58	0.13	0.22	-	run-out
			85.00	7.70	0.09	0.61	0.81	-	0.67	1.10	-
F-S14	49.50	140.26	79.00	6.90	0.09	0.56	3.13	-	-	-	-

$$S = -0.0372\log(N_f) + 0.8012$$
$$R^2 = 0.81$$

20 millions

endurance limit
S=0.54

□ Run-out Test

S $(F_{fat,max}/F_p)$

Log(N_f)
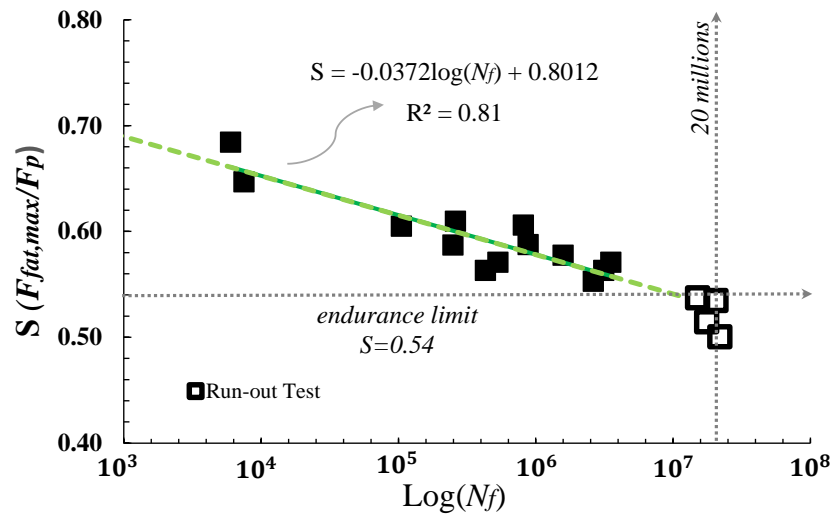
Figure 5 S-N diagram showing fatigue test results from UHPFRC circular slab elements.

3.2.2 Cracking pattern after fatigue failure

Figure 6 shows typical cracking patterns (visible by the naked eye) on the bottom surface of UHPFRC specimens after fatigue failure occurred, for various S-levels ranging from 0.57 to 1.0 (quasi-static testing). The black thick lines refer to the dominant fictitious cracks, and the thin fine lines indicate fine fictitious cracks. It is observed that all slabs failed in flexural fracture mode, characterized by multiple fine fictitious cracks and several dominant fictitious cracks with large opening. The number of dominant fictitious cracks is similar for all specimens, while the number of fine fictitious cracks reduces with decreasing fatigue stress level. Similar observation is reported for other fiber reinforced cementitious materials under uniaxial fatigue tension and flexure in [31,32].

(a) S=1.0 (quasi-static test)   **(b) S=0.68 (N_f=6000)**   **(c) S=0.61 (N_f=0.26×10^6)**

(d) S=0.58 (N_f=1.58×10^6)   **(e) S=0.56 (N_f=3.13×10^6)**

Figure 6 Typical cracking patterns of specimens after testing at various S levels.

4. Fatigue damage evolution based on DIC analysis
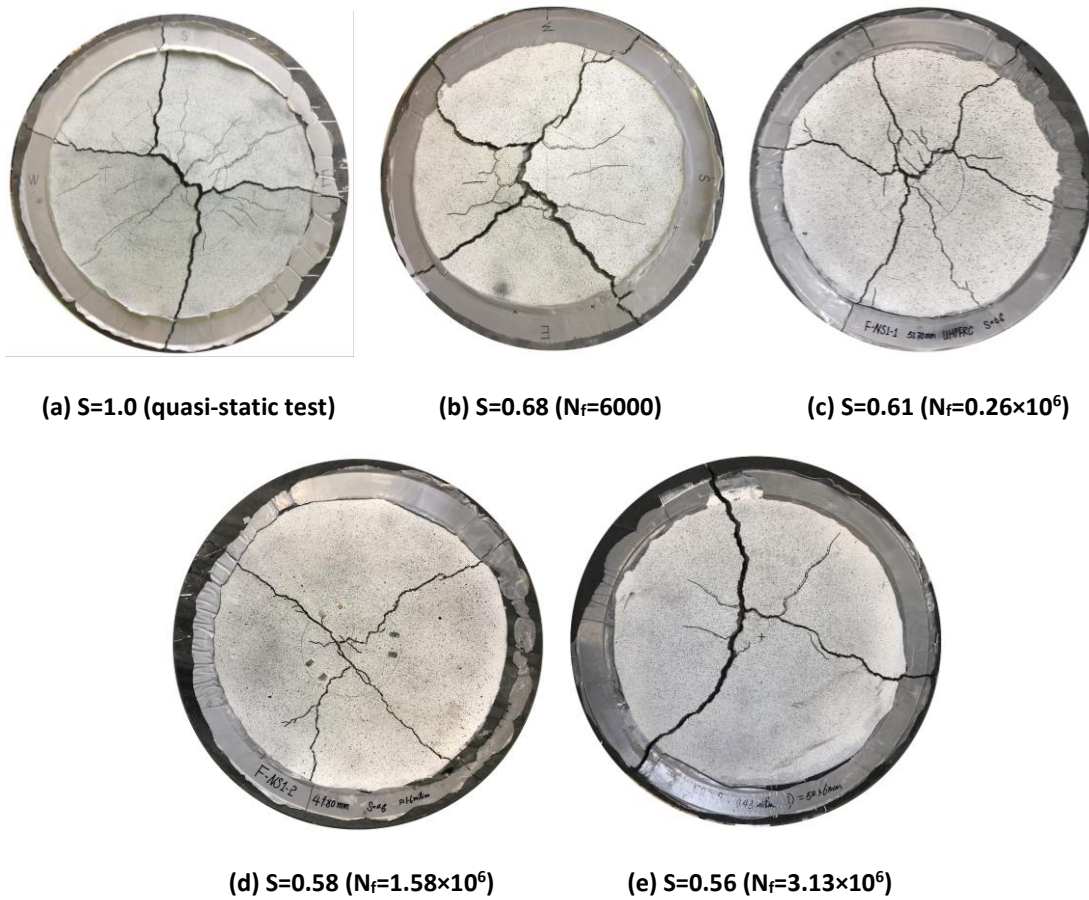
4.1 Overview

Using results from DIC analysis, the fatigue damage evolution of UHPFRC specimens under biaxial flexure is discussed in terms of central deflection as well as fracture process as described by matrix discontinuities and fictitious cracks. The fatigue damage evolution from both specimens showing fatigue failure and run-out tests is analyzed. The influence of creep on fatigue damage evolution is assumed to be negligible considering that time dependent deformation of UHPFRC largely stabilizes [33] after 90 days when the UHPFRC specimens were tested.

4.2 UHPFRC slab with fatigue failure

Figure 7 shows the typical fatigue damage evolution of specimen F-S11 considered as representative for UHPFRC specimens showing fatigue failure. The curves in Figure 7(a) stand for the maximum and minimum central deflection ($\delta_{max,i}$ and $\delta_{min,i}$) in each loading cycle, respectively. Several DIC strain contours are selected to illustrate the fracture characteristics observed on the tensile surface of UHPFRC slab under fatigue testing, as illustrated in Figure 7(a). The white dashed circle marks the position of the force transmitting ring, and the lines with different colors mark the matrix discontinuities and fictitious cracks.

Moreover, using the virtual extensometers of the DIC analysis tool, the opening response of every single matrix discontinuity and fictitious crack is recorded over the entire duration of testing. The virtual extensometers, with a measurement length of roughly 30mm, are set separately to be perpendicular to the propagation path and located at the critical part of each target. In order to obtain actual opening values, the contribution from the elastic deformation within the measurement length is deduced. Correspondingly, the maximum and minimum openings are given in Figure 7(b).

In general, an inverted S-shaped response with four phases is observed for all the damage evolution curves. The different phases are determined based on the apparent change of the evolution rate of central deflection and opening, as marked with the letters A-D in Figure 7. Moreover, based on the strain contours from DIC analysis, point A corresponds to the initiation of opening concentration on one or several fictitious cracks, represented by the orange lines on the DIC strain contours in this study. And point B refers to the grouping of several fictitious cracks within the central zone of the specimen and initiation, while other fictitious cracks are partly unloaded. Beyond point C, this group of fictitious cracks becomes dominant ($w \geq 1.3mm$ generally, hereafter called dominant fictitious crack) and develops rapidly, leading to final failure. Accordingly, the values of opening at point A, B and C (w_A, w_B and w_C) are given in Table 4 based on DIC analysis.

The characteristic response of each phase is described as follows:

(1) Phase I (OA): rapid initial evolution to stabilization: A network of matrix discontinuities and one or several fine fictitious cracks are produced on the tensile surface of the UHPFRC slab after the initial quasi-static loading, given that the specimen enters into the

hardening domain at the loading level $F_{f,max}>0.55\ F_p$. In the following fatigue cycles (less than 5% of N_f), deflection and fictitious crack opening increase rapidly. This may be attributed to multiple fine fictitious cracks that developed from matrix discontinuities due to interface degradation between fibers and matrix, as also reported in [13]. Afterward, the number of fine fictitious cracks stabilizes, and interface degradation is dominating progressively the damage propagation with increasing number of fatigue cycles. This leads to decreasing evolution rate. The maximum fictitious crack opening at point A (w_A) is in the range of 0.12mm to 0.22mm.

(2) Phase II (AB): stable evolution with slow rate: Phase II is characterized by moderate, constant and linear increase of central deflection and fictitious crack opening with increasing number of fatigue cycles up to roughly 65% of N_f. Fictitious cracks evolve gradually in terms of opening, accompanied by minor creation of new matrix discontinuities and fictitious cracks. Several fictitious cracks individually propagate as indicated by red lines on the DIC strain contours (Figure 7-a). At the end of Phase II (point B), several fictitious cracks group together within the central zone of the specimen. The maximum fictitious crack opening at point B (w_B) is in the range of 0.51mm to 0.90mm.

(3) Phase III (BC): stable evolution with high rate: Fatigue damaging process concentrates on the group of fictitious cracks which propagate radially from the center to the edge of the slab, while matrix discontinuities and fine fictitious cracks are gradually unloading. This phase still exhibits stable and nearly linear evolution up to almost 90% of N_f, although a higher evolution rate compared with that in Phase II (more than 2 times higher in terms of deflection evolution rate and 4 times higher in terms of opening evolution rate) is observed. The maximum opening of fictitious cracks at the end of Phase III (w_C) ranges from 1.29mm to 1.75mm.

(4) Phase IV (CD): rapid deterioration to failure: The dominant fictitious cracks ($w{\ge}1.3mm$ generally) in the group increases rapidly, leading to failure after a relatively short number of fatigue cycles corresponding to approximately 10% of N_f.

Figure 7 Fatigue damage evolution of specimen F-S11 (S=0.60, N_f=0.88×10^6):
(a) central deflection evolution and fracture process; (b) evolution of fictitious crack opening.

4.3 UHPFRC specimens without fatigue failure (run-out tests)

Run-out specimens show only two phases related to fatigue damage evolution. Typical evolution curves are illustrated in Figure 8 in terms of central deflection and opening of fictitious cracks:

Phase I is the rapid initial evolution of deflection and fictitious crack opening. The number of fine fictitious cracks is significantly smaller than in the case of specimens with fatigue failure.

Phase II exhibits stable increase of deflection and fictitious crack opening with much lower rate, particularly for opening evolution rate, compared with that from fatigue failure testing. For example, the average deflection evolution rate of specimen F-S13 is 6.80×10^{-8} mm/cycle, comparable to the values ($2.09 \times 10^{-8} \sim 4.52 \times 10^{-8}$ mm/cycle) reported in [3] under uniaxial flexural fatigue. However, the evolution rate in Phase II decreases gradually with increasing number of fatigue cycles. It is noted that almost no damage increase is determined during the last several million fatigue cycles ($N_f > 17 \times 10^6$), suggesting that no fatigue failure is expected.

At the end of the run-out test, the maximum fictitious crack openings are in the range of 0.25mm to 0.49mm, which are smaller than the ones at point B (w_B) of the fatigue failure tests. These values are significantly larger than 0.1mm as determined from four-point bending fatigue testing [28] and 0.24mm from direct tensile fatigue tests [13].
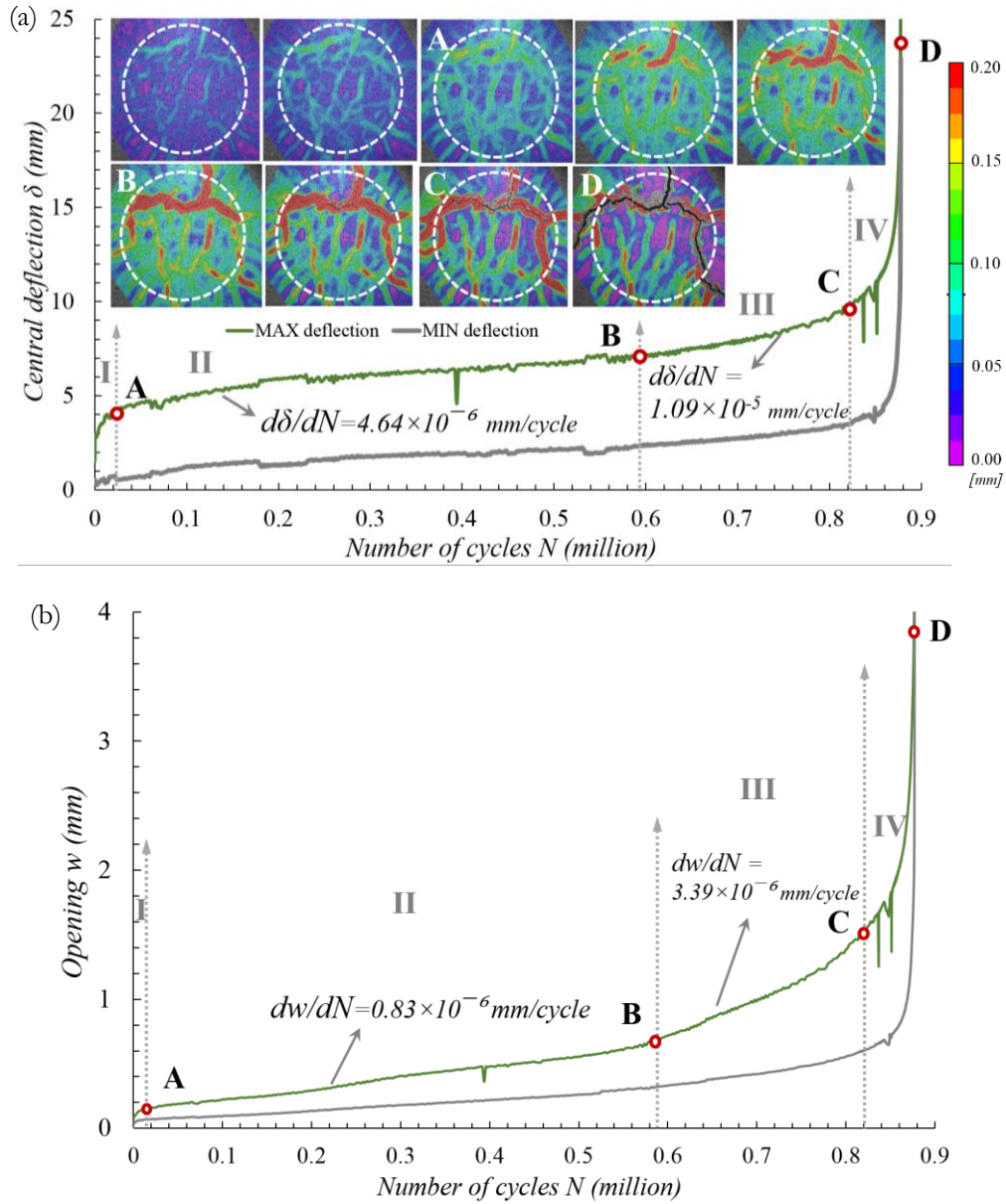
Figure 8 Fatigue damage evolution of specimen F-S13 (S=0.55, N_f=20.58×10^6):
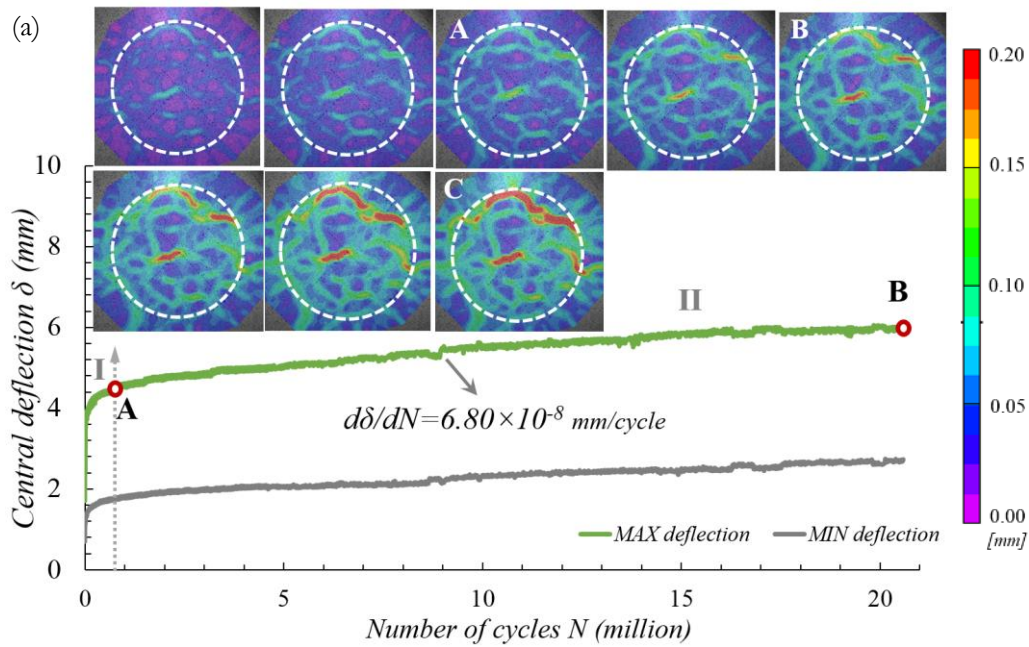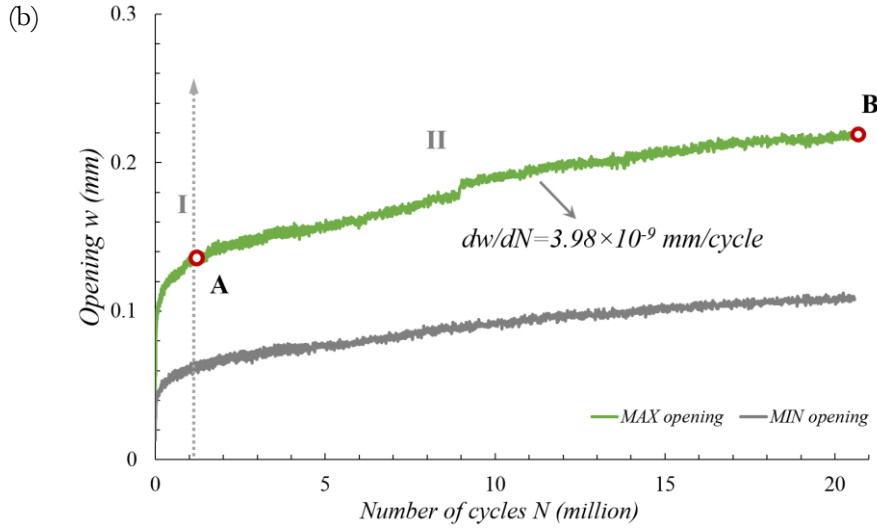**(a) central deflection evolution and fracture process; (b) evolution of fictitious crack opening**

5. Fatigue damage analysis

Fatigue is a process of damage accumulation and mechanical property degradation in materials under cyclic loading. Fatigue finally leads to failure by fracture if a certain threshold of damage is reached [34,35]. A representative damage variable is of outmost importance to characterize quantitatively fatigue damage and fatigue life.

In the following, the secant modulus obtained from the force – deflection curve of each loading cycle is introduced as damage variable describing fatigue of the tested UHPFRC slab specimens under biaxial bending. Similar concept was applied in [36,37], where the modulus of deformation under direct tension was used. In the present investigation, the secant modulus $E_{U,fat,i}$ at i-th cycle is determined as:

$$E_{U,fat,i} = \frac{F_{f,max,i} - F_{f,min,i}}{\delta_{f,max,i} - \delta_{f,min,i}} \tag{1}$$

And the fatigue damage variable D_n derived from secant modulus is expressed as:

$$D_n = 1 - \frac{E_{U,fat,i}}{E_{U,fat,0}} \tag{2}$$

where $F_{f,max,i}$ and $F_{f,min,i}$ are the measured maximum and minimum forces at the i-th cycle; $\delta_{f,max,i}$ and $\delta_{f,min,i}$ are the measured maximum and minimum deflections at the i-th cycle; $E_{U,fat,0}$ is the initial secant modulus of the UHPFRC slab specimen.

Figure 9 shows the damage evolution curves as obtained from all fourteen UHPFRC slab specimens subjected to biaxial flexural fatigue. The normalized number of fatigue cycles N_n referring to the number of cycles at fatigue failure N_f of each test is used for direct comparison between the specimens with various fatigue loading levels as well as fracture and run-out events at the end of the test. Figure 9 also includes the run-out specimens that were subsequently subjected to higher fatigue loading until failure.

The fatigue damage level of $D_n = 0.50$ subdivides into two distinct domains. Below this level, there is no fatigue failure, and no significant additional damage occurs after the initial phase. Above this level, fatigue damage is continuously accumulated until fatigue failure occurs. The damage level of $D_n = 0.50$ corresponds to the fatigue loading of $S = 0.55$ determined in Section 3.2.1 to be the fatigue endurance limit. Consequently, the test results analyzed in terms of the fatigue damage variable D_n confirm the existence of a fatigue endurance limit of the UHPFRC slab specimens under biaxial fatigue.

Figure 9 also reveals a linear relation between the fatigue damage variable D_n and the normalized number of fatigue cycles to failure, for the range between N_n=0.07 and 0.9 for all fatigue failure tests irrespective of damage degree. In this range, the average rate dD_n/dN_n is determined to be 0.26 for specimens showing fatigue fracture. For the run-out tests, the damage level D_n is less than 0.40 in the initial domain of $N_n \leq 0.07$ prior to the linear damage accumulation domain, while for the tests with fatigue failure, the value D_n is in the range of 0.45 to 0.56, suggesting a significant damage accumulation already at the early stage of fatigue.

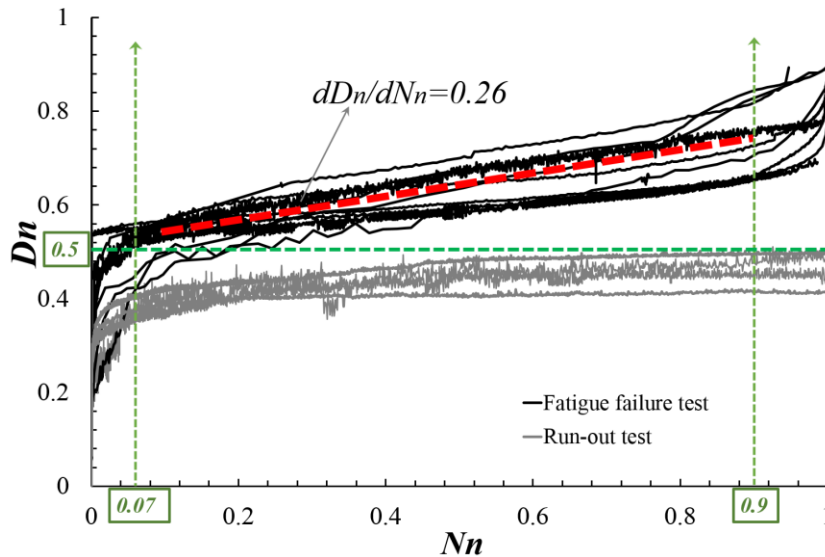**Figure 9 Damage evolution of UHPFRC slab specimens subjected to biaxial flexural fatigue**

Similar results have been reported for UHPFRC specimens subjected to direct tensile fatigue in [36], where the fatigue damage variable was characterized by the deformation modulus of the specimen. However, the value of dD_n/dN_n determined in [36] was 0.33, or about 27% higher than the value found in the present study.

This may be explained by the network of fine fictitious cracks in the case of biaxial stress state allowing for redistribution of deformation and thus damage in the UHPFRC specimen during stable fatigue damage evolution. On the contrary, only a limited number of fine fictitious cracks mainly develop in the orthogonal direction to the principle tensile stress direction in the case of the direct tension specimen [3,28] leading to higher fatigue damage accumulation.

Consequently, biaxial fatigue stress condition allows to redistribute deformation from weaker localized zones to stronger ones, thereby retarding the fatigue damage evolution in UHPFRC. This also confirms the significant stress and deformation redistribution capacity of the UHPFRC material.

6. Conclusions

The biaxial flexural fatigue behavior of strain-hardening UHPFRC thin slab elements with various levels of fatigue loading including the VHFC domain is investigated experimentally using the ring-on-ring test method. The main conclusions are:

(1) The fatigue endurance limit at 20 million cycles of the UHPFRC slab specimens tested under biaxial flexural fatigue is equal to the fatigue loading level S=0.54. This loading level almost corresponds to the quasi-elastic limit of the same UHPFRC specimen as determined by quasi-static testing.

(2) For the UHPFRC specimens showing fatigue fracture, four fatigue damage phases are determined. In Phase I, a network of fine fictitious cracks is formed on the tensile surface of slab during a small part of the fatigue life. Phase II is characterized by slow propagation of fine fictitious cracks. In Phase III, fatigue damage process concentrates on several dominant fictitious cracks with partial unloading of the remaining ones. Phases II and III show stable fatigue damage evolution comprising more than 80% of the fatigue life. Finally, rapid fatigue damage until fracture occurs in Phase IV.

(3) For run-out UHPFRC specimens, only the first two phases are observed. Multiple fine fictitious cracks are little pronounced in Phase I, and there is no more additional fatigue damage at the end of Phase II.

(4) The secant modulus is a representative fatigue damage variable to describe biaxial flexural fatigue of UHPFRC slab specimens. Derived from the secant modulus, the fatigue damage level of $D_n = 0.50$ defines the fatigue endurance limit in terms of fatigue damage in UHPFRC.

(5) Linear fatigue damage accumulation occurs in UHPFRC slab specimens showing fatigue fracture, irrespective of the fatigue loading level. The constant fatigue damage rate $\mathrm{d}D_n/\mathrm{d}N_n$ is determined to be 0.26, 27% slower than the corresponding value obtained

from direct tensile fatigue tests which may be due to the higher redistribution capacity in UHPFRC when subjected to biaxial fatigue stresses.

7. References

[1]   T. Makita, E. Brühwiler, Tensile fatigue behaviour of ultra-high performance fibre reinforced concrete (UHPFRC), Mater Struct. 47 (2014) 475–491.

[2]   T. Makita, E. Brühwiler, Tensile fatigue behaviour of Ultra-High Performance Fibre Reinforced Concrete combined with steel rebars (R-UHPFRC), International Journal of Fatigue. 59 (2014) 145–152.

[3]   E. Parant, P. Rossi, C. Boulay, Fatigue behavior of a multi-scale cement composite, Cement and Concrete Research. 37 (2007) 264–269.

[4]   G. Chanvillard, P. Pimienta, A. Pineaud, P. Rivillon, Fatigue flexural behavior of pre-cracked specimens of special UHPFRC, Special Publication. 228 (2005) 1253–1268.

[5]   F.A. Farhat, D. Nicolaides, A. Kanellopoulos, B.L. Karihaloo, High performance fibre-reinforced cementitious composite (CARDIFRC)–Performance and application to retrofitting, Engineering Fracture Mechanics. 74 (2007) 151–167.

[6]   E. Brühwiler, "Structural UHPFRC" to enhance bridges, in: Keynote Lecture, 2nd International Conference on UHPC Materials and Structures (UHPC 2018 - China), Fuzhou, China, 2018: pp. 140–158.

[7]   C. Oesterlee, Structural response of reinforced UHPFRC and RC composite members (doctoral thesis, 4848), École polytechnique fédérale de Lausanne (EPFL), 2010.

[8]   E. Denarié, E. Brühwiler, Cast-on site UHPFRC for improvement of existing structures–achievements over the last 10 years in practice and research, in: 7th Workshop on High Performance Fiber Reinforced Cement Composites, 1-3, June 2015, Stuttgart, Germany, 2015.

[9]   J. Kim, D.J. Kim, S.H. Park, G. Zi, Investigating the flexural resistance of fiber reinforced cementitious composites under biaxial condition, Composite Structures. 122 (2015) 198–208.

[10]   M. Rocha, E. Brühwiler, Prediction of fatigue life of reinforced concrete bridges using Fracture Mechanics, in: Proceedings Bridge Maintenance, Safety, Management, Resilience and Sustainability, CRC Press/Balkema, 2012: pp. 3755–3761.

[11]   SIA 2052, Technical Leaflet SIA 2052 UHPFRC – Materials, design and construction, 2016.

[12]   N. AFNOR, P18-710: National addition to Eurocode 2–Design of concrete structures: Specific rules for ultra-high performance fiber-reinforced concrete (UHPFRC), Association Française de Normalisation, 2016.

[13]   P. Rossi, E. Parant, Damage mechanisms analysis of a multi-scale fibre reinforced cement-based composite subjected to impact and fatigue loading conditions, Cement and Concrete Research. 38 (2008) 413–421.

[14]   K. Wille, S. El-Tawil, A.E. Naaman, Properties of strain hardening ultra high performance fiber reinforced concrete (UHP-FRC) under direct tensile loading, Cement and Concrete Composites. 48 (2014) 53–66.

[15]   M.K. Lee, B.I.G. Barr, An overview of the fatigue behaviour of plain and fibre reinforced concrete, Cement and Concrete Composites. 26 (2004) 299–305.

[16] E.S. Lappa, High strength fibre reinforced concrete: static and fatigue behaviour in bending, TU Delft, Delft University of Technology, 2007.

[17] M. Bastien-Masse, E. Denarié, E. Brühwiler, Effect of fiber orientation on the in-plane tensile response of UHPFRC reinforcement layers, Cement and Concrete Composites. 67 (2016) 111–125.

[18] L.F.M. Duque, B. Graybeal, Fiber orientation distribution and tensile mechanical response in UHPFRC, Mater Struct. 50 (2017) 1–17.

[19] X. Shen, E. Brühwiler, Characterization of Tensile Beahvior in UHPFRC Thin Slab Using NDT Method and DIC System, in: Proceedings PRO 129, Fuzhou, China, 2018.

[20] C. ASTM, 1499-05. Standard test method for monotonic equibiaxial flexural strength of advanced ceramics at ambient temperature, ASTM International, West Conshohocken, Pennsylvania. (2009).

[21] D.-Y. Yoo, G. Zi, S.-T. Kang, Y.-S. Yoon, Biaxial flexural behavior of ultra-high-performance fiber-reinforced concrete with different fiber lengths and placement methods, Cement and Concrete Composites. 63 (2015) 51–66.

[22] X. Shen, E. Brühwiler, Flexural quasi-static behavior of UHPFRC circular slab specimens, AFGC-ACI-Fib-RILEM Int. Symposium on Ultra-High Performance Fibre-Reinforced Concrete, UHPFRC 2017. (2017).

[23] S. Timoshenko, S. Woinowsky-Krieger, Theory of plates and shells, (1959).

[24] K. Habel, Structural behaviour of elements combining ultra-high performance fibre reinforced concretes (UHPFRC) and reinforced concrete, Doctoral Thesis (EPFL). (2004).

[25] K. Habel, M. Viviani, E. Denarié, E. Brühwiler, Development of the mechanical properties of an Ultra-High Performance Fiber Reinforced Concrete (UHPFRC), Cement and Concrete Research. 36 (2006) 1362–1370.

[26] FaroArm® - Portable 3D Measurement Arm for any application. https://www.faro.com/products/3d-manufacturing/faroarm/

[27] M.A. Michael A., J.-J. Orteu, H.W. Schreier, Digital Image Correlation (DIC), in: H. Schreier, J.-J. Orteu, M.A. Sutton (Eds.), Image Correlation for Shape, Motion and Deformation Measurements: Basic Concepts,Theory and Applications, Springer US, Boston, MA, 2009: pp. 1–37.

[28] T. Makita, E. Brühwiler, Tensile fatigue behaviour of ultra-high performance fibre reinforced concrete (UHPFRC), Materials and Structures. 47 (2014) 475–491.

[28] K. Sadananda, A.K. Vasudevan, N. Phan, Analysis of endurance limits under very high cycle fatigue using a unified damage approach, International Journal of Fatigue. 29 (2007) 2060–2071.

[30] C.T. Loraux, Long-term monitoring of existing wind turbine towers and fatigue performance of UHPFRC under compressive stresses (doctoral thesis, 8404), École polytechnique fédérale de Lausanne (EPFL), 2018.

[31] B.-T. Huang, Q.-H. Li, S.-L. Xu, B.-M. Zhou, Tensile fatigue behavior of fiber-reinforced cementitious material with high ductility: Experimental study and novel P-S-N model, Construction and Building Materials. 178 (2018) 349–359.

[32] P. Suthiwarapirak, T. Matsumoto, T. Kanda, Multiple cracking and fiber bridging characteristics of engineered cementitious composites under fatigue flexure, Journal of Materials in Civil Engineering. 16 (2004) 433–443.

[33] D. Casucci, C. Thiele, J. Schnell, Experimental Investigation on Bending Creep in Cracked UHPFRC, in: H. Herrmann, J. Schnell (Eds.), Short Fibre Reinforced Cementitious Composites and Ceramics, Springer International Publishing, Cham, 2019: pp. 19–31.

[34] J. Degrieck, W. Van Paepegem, Fatigue damage modeling of fibre-reinforced composite materials: Review, Applied Mechanics Reviews. 54 (2001) 279–300.

[35] Z. Lv, H.-Z. Huang, S.-P. Zhu, H. Gao, F. Zuo, A modified nonlinear fatigue damage accumulation model, International Journal of Damage Mechanics. 24 (2015) 168–181.

[36] T. Makita, E. Brühwiler, Damage models for UHPFRC and R-UHPFRC tensile fatigue behaviour, Engineering Structures. 90 (2015) 61–70.

[37] X. Zhao, X. Wang, Z. Wu, Z. Zhu, Fatigue behavior and failure mechanism of basalt FRP composites under long-term cyclic loads, International Journal of Fatigue. 88 (2016) 58–67.

Conclusions

1. Overview

This thesis contributes to a better understanding of the static and fatigue biaxial flexural responses of strain-hardening UHPFRC thin slab elements at both material and structural levels, with specific aim for application in bridge rehabilitation and design. In total, four experimental campaigns are carried out and provide the basis for the development of analytical models. The present chapter serves as a summary of main contributions of this thesis, and provides the potential topics pertaining to UHFPRC material and structure for extending this research.

2. Contributions and conclusions

2.1 Representative tensile behavior of strain-hardening UHPFRC thin slab element

The uniformity factor μ_2 is introduced to determine quantitatively the influence of local fiber distribution on the tensile behavior of strain-hardening UHPFRC, with the objective to characterize the representative tensile behavior of thin slab elements. Firstly, the Non-Destructive Test (NDT) method using a magnetic probe is applied for investigating the local fiber distribution within a 50mm thick slab element. Afterward, the representative tensile response is characterized using the direct tensile test (DTT) method and the Digital Image Correlation (DIC) system. The main conclusions are:

(1) Based on NDT analysis, important variation of local fiber distribution, including fiber volume fraction V_f, orientation μ_0 and efficiency μ_1, is observed within a UHPFRC slab element. Among the relevant parameters, the fiber orientation factor μ_0 shows the largest variation ($11.9\% \leq \hat{c}_v \leq 22.5\%$). Subsequently, the uniformity factor μ_2 as determined by the spacing of matrix discontinuities, is proposed to characterize quantitatively local fiber distribution within the UHPFRC element.

(2) Compared with the μ_0 and μ_1 factors, the uniformity factor μ_2 exhibits a wider range (0.13 to 0.64) within the tested UHPFC slab and has a stronger influence on the strain-hardening response of UHPFRC. Based on the testing results from the present experimental campaign and the literature, hardening strain ε_{Utu} and matrix discontinuities energy g_{Uf} vary linearly with $\mu_0\mu_1\mu_2$ for a given UHPFRC mix.

(3) For a given UHPFRC mix, there are no intrinsic tensile properties. The representative behavior is strongly dominated by the fiber distribution in the structural element. Thus, the average values of μ_2, μ_0 and μ_1 factors should be used to determine the representative tensile response of UHPFRC for the intended structural application. This can be achieved using the proposed meso-mechanical model.

(4) In a given UHPFRC layer, the uniformity factor μ_2 is thickness dependent: for UHPFRC layers with thickness of 25mm, 40mm and 50mm, the determined μ_2-factors are 0.58, 0.52 and 0.39, respectively.

(5) The NDT method using the magnetic probe allows fine and reliable contour mapping of the actual fiber distribution in UHPFRC elements. It is shown to be an efficient method to determine local fiber distribution in a UHPFRC element, thus eventually replacing fracture testing in the future.

2.2 Biaxial flexural and tensile responses of strain-hardening UHPFRC thin slab element

The biaxial flexural and tensile responses of strain-hardening UHPFRC thin slab elements are investigated experimentally and analytically. A total of four ring-on-ring tests and ten 4PBT (4-Point-Bending-Tests) are carried out using circular slab elements and small rectangular plates, respectively. Moreover, an analytical inverse analysis method for analyzing the ring-on-ring test is proposed originally to determine the biaxial tensile properties of strain-hardening UHPFRC. Ring-on-ring test and 4PBT results are then compared with special emphasis on strength, ductility and characteristics of matrix discontinuity and fictitious crack development, according to experimental evidence and inverse analysis results. The following conclusions are drawn:

(1) A four-phase structural response characterizes for biaxial flexural response of UHFPRC slab elements under ring-on-ring testing condition. In particular, the quasi-elastic limit, representing the initiation of strain concentration based on DIC analysis, is introduced. It corresponds to roughly 55% of flexural resistance, while it is 70% under 4PBT. However, the corresponding flexural strength at the quasi-elastic limit as obtained from both tests, are nearly identical. Moreover, at the quasi-elastic limit, a larger number of matrix discontinuities with maximum opening of 0.08mm is observed on the UHPFRC slab element under ring-on-ring testing, while less matrix discontinuities with maximum opening of 0.03mm are found for the 4PBT. This implies that the opening of matrix discontinuity of UHPFRC is further developed under biaxial stress condition compared with uniaxial stress condition.

(2) The ultimate flexural strength from ring-on-ring testing is roughly 28% higher than the one obtained from 4PBT. The corresponding energy absorption capacity under ring-on-ring testing is more than 3 times higher than the one from 4PBT, suggesting significant strain redistribution capacity of UHPFRC under biaxial stress condition.

(3) The biaxial flexural response from the ring-on-ring test shows random distribution and uniform network of matrix discontinuities in the quasi-elastic domain, as well as multiple fictitious cracks in the hardening domain. This represents realistically the large volume involved and fracture mechanism of real UHPFRC structural elements. In addition, the ring-on-ring test yields stable results towards a consistent characterization of the biaxial flexural response of UHPFRC slab.

CONCLUSIONS

(4) Based on the yield line and slab bending theories, an original analytical inverse analysis method from ring-on-ring test has been developed and applied successfully to determine the biaxial tensile properties of strain-hardening UHPFRC. The inverse analysis results are validated against the experimental evidence, particularly based on DIC analysis. It has been proved that the proposed inverse analysis offers a simple method to identify the biaxial tensile properties of UHPFRC based on the experimental force-deflection curve. The method does not require complicated iteration procedure and can be accomplished using a spreadsheet.

(5) The damage localization point corresponds to 63% of flexural resistance under ring-on-ring testing condition, while 90% under 4PBT condition. The corresponding biaxial strain at the end of hardening is 1.27‰, which is only 28% of the uniaxial strain. Such difference can be observed visually on the DIC strain contours at point B', where more compact distribution and higher amount of matrix discontinues in unit surface are detected on the tensile surface for 4PBT, compared with that from ring-on-ring test. The biaxial tensile strength is almost equivalent to the uniaxial tensile strength.

(6) The objective determination of the elastic limit of UHPFRC slab elements from ring-on-ring testing is proposed based on the criteria of 1% irreversible decrease of the moving average elastic modulus. This method is properly justified by the DIC analysis corresponding to the appearance of a first matrix discontinuity. It is observed that the elastic limit of UHPFRC subjected to biaxial tensile stress is around 18% smaller in average than that under uniaxial condition. This can be attributed to the fact that a large zone of the circular slab element is under pure bending in arbitrary directions, while a relatively small zone of the rectangular plate is under pure bending field in only one direction. Thus, it is plausible that the initiation of the first matrix discontinuity occurs earlier in the ring-on-ring test, given the stochastic nature and inherent variability of fiber distribution in the UHPFRC material.

2.3 Biaxial flexural fatigue behavior of strain-hardening UHPFRC thin slab element

The biaxial flexural fatigue behavior of circular slab elements made of strain-hardening UHPFRC is investigated experimentally by means of the ring-on-ring test method. Fourteen flexural fatigue tests under constant amplitude fatigue cycles up to the Very High Cycle Fatigue domain (20 million cycles) are conducted with varying maximum fatigue stress level S ranging from 0.50 to 0.70. The following conclusions are drawn:

(1) The fatigue endurance limit at 20 million cycles of the UHPFRC slab specimens tested under biaxial flexural fatigue is equal to the fatigue loading level S=0.54. This loading level almost corresponds to the quasi-elastic limit of the same UHPFRC specimen. At this loading level, the network of matrix discontinuities is fully developed on the tensile surface of the slab, as determined by quasi-static testing. This implies that the matrix

discontinuities on tensile surface of UHPFRC slab will not lead to detrimental damage under biaxial flexural fatigue.

(2) For the UHPFRC specimens showing fatigue fracture, an inverted S-shaped response with four fatigue damage phases are determined. In Phase I, a network of fine fictitious cracks is formed on the tensile surface of the specimen during a small part of the fatigue life (less than 5% of N_f). Phase II is characterized by moderate, constant and linear increase of central deflection and fictitious crack opening with increasing number of fatigue cycles up to roughly 65% of N_f. In Phase III, fatigue damage process concentrates on several dominant fictitious cracks with partial unloading of the remaining ones. This phase still exhibits stable and nearly linear evolution up to almost 90% of N_f, although a higher evolution rate compared with that in Phase II (more than 2 times higher in terms of deflection evolution rate and 4 times higher in terms of opening evolution rate) is observed. Finally, rapid fatigue damage until fracture occurs after a relatively short number of fatigue cycles corresponding to approximately 10% of N_f in Phase IV.

(3) For run-out UHPFRC specimens, only the first two phases are observed. Multiple fine fictitious cracks are little pronounced in Phase I. Phase II exhibits stable increase of deflection and fictitious crack opening with much lower rate, particularly for opening evolution rate, compared with that from fatigue failure testing. There is almost no more additional fatigue damage at the end of Phase II, suggesting that no fatigue failure is expected.

(4) The secant modulus obtained from the force – deflection curve of each loading cycle is introduced as a representative fatigue damage variable to describe biaxial flexural fatigue of UHPFRC slab specimens. Derived from the secant modulus, the fatigue damage level of $D_n = 0.50$ defines the fatigue endurance limit in terms of fatigue damage in UHPFRC.

(5) Linear fatigue damage accumulation occurs in the range between $N_n = 0.07$ and 0.9 for all UHPFRC slab specimens showing fatigue fracture irrespective of the fatigue loading level. The constant fatigue damage rate dD_n/dN_n is determined to be 0.26, 27% slower than the corresponding value obtained from direct tensile fatigue tests which may be due to the higher redistribution capacity in UHPFRC when subjected to biaxial fatigue stresses.

(6) For the run-out tests, the damage level D_n is less than 0.40 in the initial domain of $N_n \leq$ 0.07 prior to the linear damage accumulation domain, while for the tests with fatigue failure, the value D_n is in the range of 0.45 to 0.56, suggesting a significant damage accumulation already at the early stage of fatigue.

3. Implementation in practice

3.1 UHPFRC properties

3.1.1 Uniaxial strain at the end of hardening ε_{Utu}

In an UHPFRC new structural element or reinforcement layer, the characteristic value of uniaxial strain at the end of hardening ε_{Utu} is given by:

$$\varepsilon_{Utu} = \mu_2 \frac{\bar{w}_i(f_{Utu})}{S_{r,c}} + \frac{f_{Utu}}{E_U} \tag{1}$$

- μ_2: uniformity factor accounting for the variation of local fiber distribution. In general, a series of suitability tests representing the structural element in the real stress states must be conducted, and the average value of uniformity factors should be used to scale the tensile response to the dimensions of the structural elements of the intended application. The values of 0.58, 0.52 and 0.39 are suggested for the UHPFRC thin layers with thickness of 25mm, 40mm and 50mm, respectively.

3.1.2 Inverse analysis to determine the equi-biaxial tensile properties

The principle of the inverse analysis method is to convert pairs of measured force F_i and deflection δ_i at characteristic points under ring-on-ring testing into corresponding pairs of equi-biaxial tensile stress and strain at the surface of the specimen in the constant moment zone under tension.

(1) The equi-biaxial elastic modulus E_U is given by:

$$E_U = \frac{3(1-v^2)}{2\pi h^3} \frac{(F_e - F_0)}{(\delta_e - \delta_0)} \left[\frac{(3+v)(R^2 - r^2)}{2(1+v)} + r^2 \ln \frac{r}{R} \right] \tag{2}$$

- F_e, δ_e: the measured force and deflection at the end of the linear-elastic behavior of the specimen under ring-on-ring testing.

(2) The equi-biaxial elastic limit stress f_{Ute} is given by:

$$f_{Ute} = \frac{3F_e}{2\pi h^2} \left[\frac{(1-v)(R^2 - r^2)}{2R^2} - (1+v) \ln \frac{r}{R} \right] \tag{3}$$

(3) The equi-biaxial tensile strength f_{Utu} is given by:

$$f_{Utu} = 1.15 \frac{F_p}{\pi h^2} \frac{R - r}{R} \tag{4}$$

(4) The equi-biaxial strain at the end of hardening is given by:

$$\varepsilon_{Utu} = \frac{(1-v)f_{Utu}}{E_U} + \alpha_u \chi_u h \tag{5}$$

- α_u: ratio of the height of the yielding zone and the total height of the specimen at damage localization point under ring-on-ring testing;
- χ_u: the curvature at damage localization point under ring-on-ring testing;
- The details about the determination of damage localization point can be found in the section 2.5, Chapter 4.

3.2 Verification of fatigue safety

The fatigue safety verification of UHPFRC new structural element or reinforcement layer under biaxial flexure consists of two-item check: strain level check and secant modulus level check.

(1) At strain level check, the maximum biaxial strain at the most tensioned surface of the UHPFRC element need to be checked according to:

$$\varepsilon_{U,fat,max}(Q_{fat}) \leq \varepsilon_{Utud} \tag{6}$$

- Q_{fat}: characteristic value of fatigue loading;
- ε_{Utud}: design value of biaxial strain at the end of hardening.

(2) At secant modulus level check, the secant modulus of UHPFRC element need to be checked according to:

$$n_{fat} = \frac{E_{U,fat,res}}{0.5 \cdot E_{U,fat,d}} \geq 1.0 \tag{7}$$

- n_{fat}: fatigue safety index;
- $E_{U,fat,res}$: examination value of residual secant modulus of UHPFRC element;
- $E_{U,fat,d}$: design value of original secant modulus of UHPFRC element

4. Perspectives and future works

4.1 UHPFRC properties

(1) Improve and systemize the NDT method

Reliable and systematic NDT methods using magnetic probe should be further developed to determine the tensile response of UHPFRC efficiently and representatively, thus eventually replacing the fracture testing in the future. Firstly, the quantitative relationship

between tensile properties, in particular tensile strength and hardening strain, and inductance values from NDT measurement should be determined for the given family of UHPFRC materials. Secondly, different sizes of magnetic probes should be fabricated to fit various geometries of UHPFRC elements, e.g. large slab cast-on-site and prefabricated elements with complex geometry.

(2) Investigate the influence of local fiber distribution on the tensile behavior of UHPFRC using FEA

The present study introduces the uniformity factor μ_2 for considering the local fiber distribution in UHPFRC specimens. The significant influence of μ_2 on the tensile response, especially the hardening strain, is highlighted. However, the amount of tested specimens and range of μ_2 is limited. Thus, an extensive finite element analysis (FEA) is expected to validate the proposed meso-mechanical model, and establish the direct relationship between local fiber distribution and the uniformity factor μ_2. In this regard, a valid numerical model should be conducted firstly to fit with the experimental evidence in terms of stress-strain response and cracking behavior. Afterward, a wide range of quantitative degrees of variation of local fiber distribution, which can be represented by variation of the tensile strength, can be applied to the numerical model.

4.2 Ring-on-ring test to characterize UHPFRC

(1) Ring-on-ring test using small slab specimen

The ring-on-ring test yields representative and stable results allowing for consistent characterization of the biaxial flexural response of UHPFRC slab elements. However, the circular slab used in the present study has a large size with diameter of 1200mm and thickness of 50mm ($\approx$140kg), which is not easy for handling and placing. Moreover, such geometry of specimen cannot fit in standard servo-controlled testing machines. Therefore, a smaller circular slab specimen is proposed for the ring-on-ring test.

(2) Evaluate the structural redistribution coefficient using a numerical approach

The unfavorable influence of intrinsic heterogeneity of local fiber distribution on the fracture response can be considerably compensated when large cracking surfaces are involved in the fracture process due to stress redistribution. This is particularly so in the case of strain-hardening UHPFRC under biaxial flexural testing, given that a large network of matrix discontinuities and multiple fictitious cracks are observed. Therefore, a coefficient (structural redistribution factor) should be introduced to take into account the reduced variability of mechanical bearing capacity when associated with a large volume involved in the failure process and/ or when the structure is able to redistribute stresses significantly, thus favoring the average rather than the minimum strength. In this context, a numerical procedure taking into account a wide range of heterogeneity of the mechanical

characteristics in the UHPFRC slab can be conducted to evaluate the redistribution factor based on the ring-on-ring testing results.

4.3 Fatigue behavior of UHPFRC

(1) Fatigue behavior of UHPFRC under variable amplitude

In bridge deck slabs, the amplitude of fatigue loading caused by vehicles is generally variable. The present experimental study, however, is limited to the biaxial flexural fatigue behavior of UHPFRC slab under constant amplitude fatigue loading. Hence, the fatigue behavior of UHPFRC under variable amplitudes, as well as fatigue stress reversals, should be investigated.

(2) Fatigue behavior of UHPFRC considering fiber distribution

It has been demonstrated that the local fiber distribution has significant influence on the strain-hardening response of UHPFRC under direct tension. However, its influence on the tensile fatigue behaviour is not yet clear, which still needs to be investigated experimentally. Moreover, great care is required during alignment and installation of the specimen for direct tensile fatigue testing to avoid initial eccentricities before testing. Otherwise, the specimen may be pre-damaged, leading to significant underestimation of the fatigue strength of UHPFRC.

ENAC Faculté de l'Environnement Naturel, Architectural et Construit
IIC Institut d'Ingénierie Civile
MCS Maintenance, Construction et Sécurité des ouvrages

EPFL

CURRICULUM VITAE

PROFILE

Name: **Xiujiang Shen**   Degree: Ph.D.

Gender: Male   Date of Birth: January 1st, 1990

Nationality: China   Email: xiujiang.shen@epfl.ch

shenxiujiang@gmail.com

Address: EPFL ENAC IIC MCS, GC B3 454 (Bâtiment GC), Station 18, CH-1015 Lausanne, Switzerland

EDUCATION

❖ Doctor (2015.10 ~ 2020.04)

École polytechnique fédérale de Lausanne (EPFL), Switzerland

Dissertation: **Static and Fatigue Biaxial Flexural Behavior of Strain-Hardening UHPFRC Thin Slab Elements**

Supervisor: Prof. Eugen Brühwiler

❖ Master of Engineering (2012.9 ~ 2015.6)

Fuzhou University, China

Thesis: **Test Study on Tensile Behavior of UHPFRC** (Best Thesis Award in Fujian Province)

Supervisor: Prof. Baochun Chen

RESEARCH INTEREST

❖ UHPFRC material and its mechanical performance, in particular tensile and fatigue behavior;

❖ Structural response and fatigue safety of UHPFRC elements;

❖ Rehabilitation and strengthening of existing structures using UHPFRC.

SELECTED PUBLICATIONS

❖ **Influence of Local Fiber Distribution on Tensile Behavior of Strain-Hardening UHPFRC using NDT and DIC** (*Cement and Concrete Research 132 (2020): 106042.*)

❖ **Biaxial Flexural Behavior of Strain-Hardening UHPFRC Thin Slab Elements** (*Construction and Building Materials, Volume 255, 20 September 2020, 119344*)

❖ **An Analytical Inverse Analysis to Determine Biaxial Tensile Behavior of Strain-Hardening UHPFRC from Ring-on-Ring Test** (*Submitted to Materials and Structures*)

❖ **Biaxial Flexural Fatigue Behavior of Strain-Hardening UHPFRC Thin Slab Elements** (*Submitted to International Journal of Fatigue*)